Generation of laminar streaks in a Rankine-body boundary layer by free-stream vortical disturbances

Eva Zincone

A Thesis submitted for the degree of Doctor of Philosophy

Department of Mechanical Engineering

University of Sheffield

February 2018

CONTENTS

LIST OF FIGURES

LIST OF TABLES

ACKNOWLEDGEMENTS

Firstly, I am grateful for the funding received by the Air Force Of Scientific Research and the University of Sheffield to undertake my PhD.

I would like to express my sincere gratitude to my supervisor Dr Pierre Ricco for the continuous support of my PhD study, for his patience and motivation.

I thank my colleagues, in particular Claudia and Elena, not only for the helpful discussions, but especially for all the fun we have had together in the last four years. They are now much more than just colleagues!

I also thank my friends, particularly Donatella and Gessica who, despite the distance, have always been there to listen.

A big "Thank you" goes to all the wonderful people I have met in Sheffield. To all my international friends for the unforgettable time spent together and to my climbing friends who taught me that *every mountain top is within reach if you just keep climbing.*

Last but not the least, I would like to thank my family for supporting me in my life in general.

ABSTRACT

It is known that friction due to boundary layer disturbances can affect the performances of many engineering systems and there are many works on the suppression of the transitional boundary layer. Most of the results on the velocity and pressure in the literature are for the flat-plate boundary layer, but it is interesting to see how the velocity and pressure change with the curvature. This work aims to extend the results of the flat-plate boundary layer to a Rankine-body boundary layer.

A small amplitude, unsteady, three-dimensional perturbation of a mean base flow is considered. The flow is assumed incompressible and the Reynolds number high. The analysis is performed in an optimal coordinate system, where the streamwise coordinate is replaced by the velocity potential and the wall normal coordinate by the streamfunction associated to the inviscid mean flow given by a uniform flow which encounters a source flow. The perturbation flow around and far from the body is solved analytically.

In the viscous region near the body, the base flow satisfies the steady mean flow equations in optimal coordinates with no similarity. Boundary region equations in optimal coordinates for the perturbation flow are derived and numerically solved by imposing no-slip conditions at the wall for the three velocity components and appropriate boundary conditions at a large distance from the body. The latter are found by matching with the outer solution. The boundary region equations are parabolic in the streamwise coordinate therefore a marching procedure along this coordinate will be used in the code. Initial conditions to start

the code are derived.

The results suggest that the mean pressure gradient modifies the shape of the streamwise velocity profile compared to the one of the flat-plate boundary layer and the inner perturbation pressure matches the outer one at a large distance from the body. It is observed that the streamwise wavenumber of the perturbation plays a key role in the development of streaks.

1. INTRODUCTION

The interaction of a fluid in motion with a solid surface affects the performance of mechanical, aeronautical, civil and chemical engineering systems. When an object moves through a fluid, a boundary layer is created on its surface. In this region viscous effects are not negligible, while far from the body if the Reynolds number based on the velocity of the flow, the characteristic length and the kinematic viscosity is high enough, viscosity can be neglected. Normally in this kind of problem the domain is divided in two regions, one inviscid region far from the object and the small viscous boundary layer region. The velocity flow within the boundary layer starts from zero (no-slip condition due to adherence to the wall) and then it rapidly increases until it reaches the value of the free stream velocity. The boundary layer can either be laminar or turbulent. In the former case the fluid flows in parallel and ordered layers while in the latter case the flow is chaotic. Generally, the boundary layer goes from laminar to turbulent through a transitional zone. It has been established that turbulent flows exert a much higher wall friction than laminar flows. Since vehicles such as cars and airplanes, for example, consume an enormous amount of energy due to friction, many works have been directed to the suppression of transitional boundary layer disturbances. It is better achieving drag reduction in the still laminar transitional zone than in the already developed turbulent one because suppressing small-amplitude laminar disturbances requires less energy. The reduction of drag has a great technological importance because it implies a significant decrease of the enormous amount of energy consumed by airplanes during flight. Moreover flight

costs and aerodynamic noise could be reduced and number of the passenger per flight could be increased. Such outcomes could restrict the global warming effect. Despite the process which governs the transition has been widely studied, at present is not fully understood.

The flow within the boundary layer is influenced by the external flow. In the literature there are numerous papers in which the effects of free stream turbulence (FST) on the boundary layer are analysed. FST is defined by the turbulence level (Tu) and the turbulence length scales. The experimental work of Matsubara & Alfredsson (2001) confirms that if Tu is low (< 1 %) the transition from laminar to turbulent boundary layer occurs for the growth of Tollmien-Schilichting (TS) waves; otherwise, if Tu is high ($> 1\%$) the mechanism which determines the passage from laminar to turbulent is called *bypass transition*. During *bypass transition* the boundary layer is laminar and the flow is characterised by long streamwise perturbations known as streaks. These streaks are also called *Klebanoff distortions*, because Klebanoff was among the first to observe the streaks. Due to non-parallel flow effects, these low-frequency components of three-dimensional vortical disturbances in the free stream penetrate the boundary layer and they produce significant distortions in the spanwise direction. There are a large number of direct laboratory investigations of the transition process in the presence of Klebanoff fluctuations. Kendall (1990) observed the intermittent appearance of a wave packet in the boundary layer at moderate levels of free-stream turbulence. Even if he did not understand the origin of Klebanoff modes he performed many experiments which revealed some important characteristic of them. They appear only when the turbulence level is higher than a threshold, they grow faster than TS waves and they propagate quickly downstream and slowly in the spanwise direction. Downstream of the streaky region turbulent spots appear and then a turbulent boundary layer fully develops.

In recent years, Klebanoff modes have been widely investigated. Works on a flat plate geometry are presented in section 1.1 and a review of studies performed on bluff bodies is presented in section 1.2. The latter is more relevant for this project, where the effect of the curvature and the flow at the stagnation point are investigated.

1.1 Flat plate

1.1.1 Experimental works

Bypass transition has been mainly studied experimentally and all the results showed that FST induced streamwise streaky structures of alternate high and low velocity in the boundary layer. Dryden (1936) obtained information about the origin of eddies and turbulence effects by performing experiments in a wind tunnel. He showed that the velocity in the boundary layer was affected by the turbulence in the free stream and by the pressure gradient. He observed that the amplitude of fluctuations was higher in the boundary layer than in the free stream, while the frequency was lower, as if the boundary layer worked as a low-pass filter. Taylor (1939) continued to perform experiments in the wind tunnel and his observations were in agreement with those of Dryden (1936). In the literature the first experiments on transitions are attributed to Klebanoff (1971) and the observed streaks in the boundary layer are called Klebanoff modes after him. Johnson & Ercan (1999) developed a new method to predict boundary layer transition by modelling the velocity fluctuations induced by FST. They suggested that the transition process was dominated by low frequencies of perturbations. Their model was used to predict the start and the end of transition and the propagation of the spots. They also showed the relation between the integral length scale and the transition length, which was inversely proportional to the level of turbulence. In effect, at low turbulence there was a high dependence of

the length scale, while at high turbulence the transition process was completely independent of the length scale. Two years later Matsubara & Alfredsson (2001) made experiments using techniques like *flow visualisation* and *hot-wire anemometry* in order to determine the effects of FST (in the range of 1-6 %) in the boundary layer. They performed the experiments using grids of various sizes to generate the free-stream turbulence on a test plate. They determined streamwise and spanwise scales of the streaky structures, namely the wavelengths of the disturbance. They found that the spanwise velocity decreased moving downstream, where it approached the boundary layer thickness. Conversely the streamwise velocity increased and it became proportional to the boundary layer thickness, going downstream. As it can be seen in Figure 1.1, their results showed that a streaky region could be observed in the boundary layer, in which high and low velocity alternated. They also pointed out that the breakdown of the streaky structures was associated with a secondary instability which seemed to lead to turbulence.

Boundary layer transition from laminar to turbulent depends on many parameters, such as Reynolds number, Tu and Mach number. In the paper of Walsh *et al.* (2004) it was pointed out that transition affect both entropy production and heat transfer. They also suggested that the boundary layer transition was only driven by the entropy generation rate and that all the other parameters were functions of it. Fransson *et al.* (2005) , by making measurements on FST induced transitions with $1.4\ \% < Tu < 6.7\ \%$, affirmed that the disturbance energy is proportional to Tu^2 and Re (Reynolds number). Like Matsubara & Alfredsson (2001) they used different grids to generate turbulence. They made a model of the the transition zone, with the aim to determine the intermittency of the velocity signal in it. In effect they found the universal shape of the intermittency function. This allowed them to determine flow properties in the transitional zone. Moreover

the model of transition zone demonstrated that for $Tu > 2.5$ % the transition zone length increased with increasing of Tu. They also found a formula for the spot production rate. Mans *et al.* (2005) analysed in detail oscillations during bypass transition, using an experimental set-up formed by a water channel and they found that two secondary instability modes were present: the antisymmetric one, also called sinuous and the symmetric one, called varicose. The amplitudes of these spanwise oscillations increased both spatially, specifically in the upstream direction, and temporarily. When a critical amplitude of each mode was reached, turbulent spots appeared. A few years later they focused on the antisymmetric mode to understand how the sinuous secondary instability mode could initiate the natural breakdown to turbulence. The study showed that this instability resulted in a streak configuration in which low-speed streaks were near to each other in the spanwise direction and that pieces of low speed fluid were present in the high-speed streaks. This interaction led to vortices that then developed in 3D structures (Mans *et al.* , 2007). Liepmann & Nosenchuck (1982) used active feedback control to reduce the TS wave amplitude and then to delay transition to turbulence. Their work is different from the previous experimental works since they used phase control instead of the modification of the mean-velocity profiles.

1.1.2 DNS works

Direct numerical simulation (DNS) is a method to numerically solve the Navier-Stokes equations. Many authors performed simulations on bypass transition induced by free-stream turbulence (sometimes in complement with laboratory experiments). Kleiser & Zang (1991) reviewed some work about direct numerical simulation on transition. In particular they discussed the interaction between different theories and numerical results. They pointed out that the principal objective of numerical simulations was to obtain a complete model of the transition

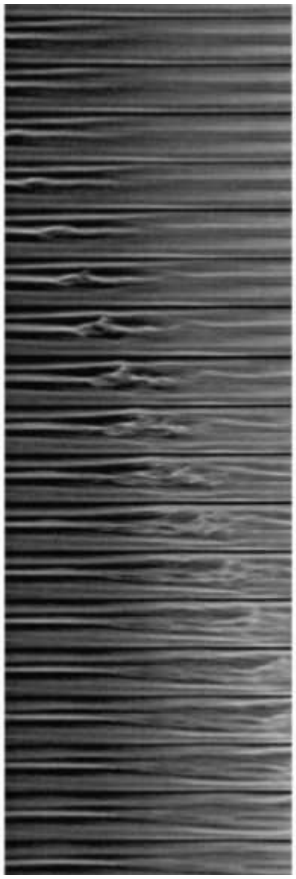

Fig. 1.1: Development of a streak instability. The time between frames is 20 m s, the free-stream velocity is 2 m s^{-1} and the speed of the structure is about 0.5 U_∞. (Matsubara & Alfredsson, 2001).

process. Landahl (1980) showed that inviscid parallel flows exhibited kinetic energy growth associated with the streamwise velocity component. He confirmed the presence of long streaks in the boundary layer which depended on the amplitude of the free stream velocity. The linearized theory used in his work was limited by nonlinear effects and secondary instabilities, namely his results were valid only in the hypothesis that the characteristic length is much larger than the initial velocity perturbation (multiplied by time). In other words, his results were only valid in a small time interval. Rist & Fasel (1995) developed a method based on the spatial-mode to reproduce the laboratory experiments. By analysing the numerical results they identified the shear layers and vortical structures. They understood that different visualisation techniques could give different observations in some mechanisms, while their numerical results were in perfect agreement with the experiments of Klebanoff.

Jacobs & Durbin (2001) depicted eddies and interactions between the modes of the perturbation flow during transition induced by free-stream turbulence. Their simulations showed that when low-frequency modes penetrated the boundary layer, they produced lower frequency modes, which were amplified by the shear and they developed into streaks in the streamwise velocity. These streaks had the same shape and behavior of those observed in the experimental measurements. The results showed that streaks were stable if they remained near the wall, mechanism known as transient growth, because there is an initial growth followed by exponential decay; instead if they lifted up, the disturbance rapidly grew and turbulent spots appeared. Then the spots led to turbulent boundary layer. Brandt & Henningson (2002) studied the transitions originated by sinuous instability in an incompressible flat-plate-boundary-layer flow. They found that during the transition process elongated streamwise vortices were present. At the late stages, far from the wall the periodic motion continued while close to the

wall they observed turbulent spots.

Zaki & Durbin (2005) explored the penetration of external vortical disturbances in the boundary layer, by studying Orr-Sommerfeld modes interaction. The evolution of modes was analysed by DNS and the domain included boundary region zone inside the boundary layer. The transition process was simulated with two modes: one strongly coupled and one weakly coupled high-frequency mode. Results showed that if one mode penetrated the boundary layer and the other one did not, there was transition. In this paper it was confirmed that low frequencies penetrated the boundary layer and they led to Klebanoff modes. Zaki & Durbin (2006) continued their studies by investigating the role of the pressure gradient on the flat-plate transitional boundary layer by changing the angle of attack β. Their results showed that under adverse pressure gradients the Klebanoff distortions were stronger and the transition occurred earlier. Moreover, they observed that for high turbulence levels the transition was independent by the pressure gradient. They also underlined that the effect of the pressure gradient on the amplitude of the streaks was enhanced by scaling the velocity by the local mean velocity, namely considering the spatial variation of the mean flow.

Ovchinnikov *et al.* (2008) made DNS of bypass transition due to high-amplitude FST to study the effects of the FST length scale and disturbance behavior near the leading edge. They performed different DNS of boundary layer transition in order to study how the transition behavior changed with the variation of the FST length scale. Results showed the importance of the FST length scale to start the transition and also to determine the physical mechanism. They concluded by suggesting that different FST length scales would produce different disturbance growth rates in the boundary layer and this would explain the differences in the measured transition origins in the experiments.

1.1.3 Theoretical works

For a long time bypass transition has only been experimentally observed, but it could not be theoretically explained. During the 1980's and the 1990's a new mechanism was discovered. It was called *algebraic growth*. In more recent years the role of algebraic growth was theoretically explained by *transient growth theory* which is a candidate mechanism for bypass transition because it is essentially algebraic growth followed by exponential decay. One of the first works based on transient growth theory is Libby & Fox (1964). They used perturbations of the Blasius solution to describe the velocity fields associated with different flows and they described the linearization procedure to improve each perturbation solution in order to obtain high-order effects. They considered that the initial velocity profiles deviated from the Blasius solution. A more recent work is of Butler & Farrell (1992), who attempted to explain the transition to turbulence for stable modes in channel flow. They found the 3D optimal perturbations responsible of the streaks of streamwise velocity. They had a profound effect on the flow, in effect they were the cause of streaks which could lead to secondary instabilities. Butler & Farrell (1992)'s work demonstrated that using 3D disturbances, instead of 2D disturbances, was a better approach to describe the development of small disturbances. In the same period Luchini (1996) found an unstable 3D perturbation which developed at any Reynolds number, in contrast to previously known flow instabilities. The flow did not depended on Reynolds number because Prandtl's boundary layer equation were used (Reynolds number scaled out). Before his work, the known effects which caused instabilities were the TS waves and Gortler vortices. In Libby & Fox (1964) a 2D perturbation was assumed, but the response of a 2D flow to a 3D perturbation could be different. Luchini (1996) considered a non-parallel base flow and this choice had the consequence that the algebraic growth was not followed by viscous decay, even in presence of

viscosity. The mathematical model of Luchini (1996) could describe the initial linear amplification of bypass transition. In the following sections three different theoretical approaches are described.

- *Optimal growth theory* which is a method used to calculate the optimal perturbations, namely the initial velocity perturbation profile which produces the biggest amplification of the disturb.

- *Orr-Sommerfeld theory*, based on the Orr-Sommerfeld equation, which determines the conditions for the stability. It is very important because the solution of the Navier-Stokes equations can become unstable under some conditions of the flow.

- *Goldstein theory* is explained in details because this project is based on it.

Optimal growth theory

Luchini (2000) continued his work by determining optimal perturbations with a new method based on the upstream integration of adjoint equations. He realised that transient amplification explained the linear growth of initially small disturbances. Then a secondary instability excited nonlinear interactions and caused transition. He found the maximum amplification factor approachable through the mechanism of algebraic growth and he also determined the spanwise wavenumber corresponding to the maximum amplification factor. Since the amplification range was centred at zero frequency, the steady case was very easy and interesting to study. He could clarify the strange concordance between the experimental observations and the theoretical results that the perturbation profiles of transitional flow had a single maximum. He explained this fact by declaring that the shape of the streak always tended to the shape of the perturbation, even if it was not the optimal one. Andersson *et al.* (1999) calculated the maximum spatial

transient growth in the Blasius boundary layer and concluded that the energy growth is due to vortices aligned in the streamwise direction.

One of the most recent works on optimal growth theory is of Higuera & Vega (2009), who constructed a numerical scheme in order to describe streaky perturbations as a streamwise evolving solution of the problem formulated by Luchini (1996). They showed that the growth of internal streaky perturbations was algebraic instead of exponential and they supported the idea that the optimisation procedure to define optimal streaks was not necessary because the streamwise evolution exhibited a growth decay (transient growth).

Orr-Sommerfeld theory

The aim of the Orr-Sommerfeld theory is to study under which conditions the solution of the Navier-Stokes equations is unstable, namely when the solution keeps increasing as $y \to \infty$,where y is the coordinate normal to the surface. The flow is divided in a mean *parallel* flow (a mean flow with just the streamwise component) and a perturbation flow in the three directions. Once obtained the equations for the perturbation flow (collecting terms of order ϵ , with ϵ the amplitude of the perturbation velocity) a periodic solution in x, z and t is substituted in the equations to obtain the Orr-Sommerfeld equations and the wavenumber which makes the solution stable can be found.

The solution of the Orr-Sommerfeld equation has both discrete and continuous modes. Jacobs & Durbin (1998) argued that a general free-stream disturbance in a viscous flow could be seen as a superposition of continuous modes. In their paper a method to compute the continuous modes and to show their inability to penetrate the boundary layer was developed. This latter phenomenon was called *shear sheltering*. Results showed that the penetration depth of the disturbance in the boundary layer depends on frequency and Reynolds number.

In the recent paper of Dong & Wu (2013) it was argued that continuous modes of the Orr-Sommerfeld equations could not be used to represent free-stream vortical disturbances. The main reason was that they were derived from the non-parallel-flow approximation.

Goldstein theory and recent works

In recent years many works have been carried out on turbulent flow on a flat plate. They aimed to find a solution for the flow in the boundary layer. Leib *et al.* (1999) analysed the effects of free-stream turbulence on the pretransitional boundary layer on a flat plate. The flow is decomposed into the mean flow (a *uniform flow* in the streamwise direction) and a purely convected *perturbation flow* (in the three directions). The domain is divided in four asymptotic regions as shown in figure 1.2. Region I is the inviscid upstream outer region, where the flow is modified by the presence of the body without considering the displacement effect; region II is the two dimensional boundary layer region, where the spanwise viscous effects are negligible respect to the normal viscous effects; region III is the three dimensional boundary layer region where the spanwise viscous effects are to take in account; finally, region IV is the downstream outer region, where there is the displacement effect. They found analytic solutions for equations in region I, II and IV and they derived the boundary and initial conditions to numerically solve the equations in region III.

They assumed that the turbulence velocity satisfied the solenoidal condition. In region I the flow is determined by Laplace's equation which can be solved with the method of variation of parameters. Therefore they found an analytic solution of the inviscid perturbation velocity. In region II and III the mean flow solution is determined by Blasius equation, but the perturbation flow in these two regions has to satisfy different equations.In fact, in region II the boundary

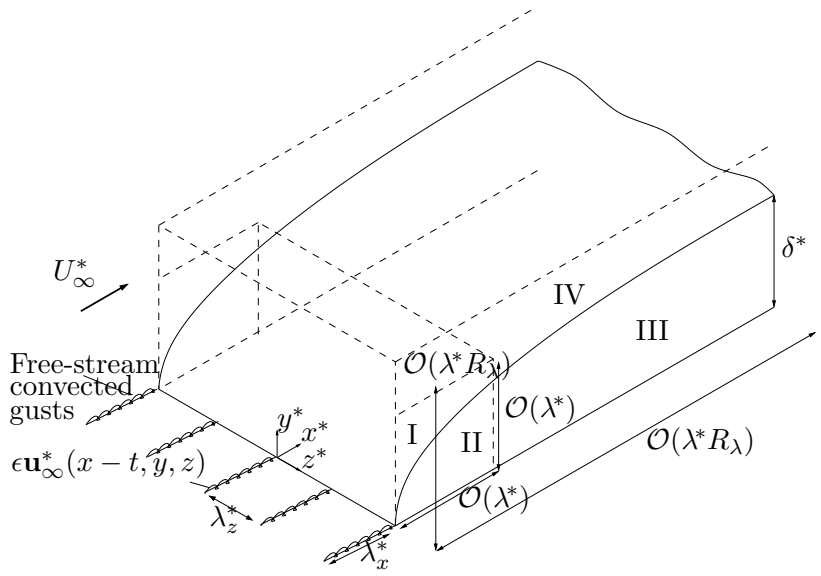

Fig. 1.2: Flow configuration.

layer thickness is small compared with the disturbance wavelength and thus in the boundary layer equations the second derivative with respect to the spanwise direction can be neglected; moreover there is no pressure gradient. The solution of the boundary layer equations has to satisfy the appropriate upstream boundary conditions and a solution in this region is found to show that the streamwise velocity grows linearly with the streamwise coordinate.

In region III, where the boundary layer thickness is of the same order of the disturbance wavelength, the flow is governed by the linearized unsteady boundary-region equations, in which the second derivative with respect to the spanwise direction is not negligible anymore and there is a pressure gradient. They are solved numerically after having derived the upstream and far-field boundary conditions by matching the solutions in the near regions. The flow in region IV is used to derive far-field boundary conditions. Here the mean velocity components are expressed as the derivatives of the complex streamfunction, where the displacement effect is considered. There are no pressure fluctuations

in this region and the perturbation velocity is determined by introducing the streamfunction variable in place of the normal one. The analytic solution in region IV is found and then it is used as a boundary condition for the large-η form of boundary region equations , where η is the rescaled normal coordinate.

Since the equations are linearized they could divide the solution in individual Fourier components and they showed that the low-frequency transverse velocity fluctuations in the free-stream are the cause of Klebanoff modes. In section 3.2 some of the numerical results of Leib *et al.* (1999) are shown.

A few years later Wundrow & Goldstein (2001) considered the general case of the effects on a laminar boundary layer of small-amplitude, steady, streamwise vorticity in the upstream flow, by taking a finite Reynolds number. They showed that the upstream linear perturbation led to a downstream small nonlinear perturbation. Ricco *et al.* (2011) generalised the results of Wundrow & Goldstein (2001) to an unsteady case, then considering $k_1/\epsilon = \mathcal{O}(1)$, where k_1 is the streamwise dimensionless wavenumber. They studied the instability of unsteady nonlinear streaks due to free-stream disturbances on an incompressible laminar boundary layer. Their attention was focused on long disturbance wavelengths because it is known that they are responsible for the streak generation. Their results showed that the nonlinearity can inhibit the amplification of streaks, thus it has a stabilising effect and nonlinear interactions have an effect of distortion on the mean flow. These numerical results are in agreement with the experimental results of Matsubara & Alfredsson (2001).

1.2 Bluff body

1.2.1 Experimental works

Among all the works on bluff bodies, many studies have focused on understanding perturbed stagnation point flows and one of the first experimental observations

was that free-stream turbulence induce large heat transfer enhancement at the stagnation point. Later it was recognised that the turbulence length scale was a key parameter in determining the effects of the free-stream turbulence, in particular it was found that the heat transfer enhancement increases with increasing Reynolds number and turbulence intensity and decreases with decreasing turbulence length scale.

Experimental observations are discussed in Bearman (1972), Bearman & Morel (1983), Maciejewski & Moffat (1992) and Ueda *et al.* (1997). Bearman (1972) measured the distortion of turbulence approaching a two-dimensional bluff body. His experimental results were in agreement with the basic theory of Hunt (1973).A few years later Bearman & Morel (1983) performed experiments in a wind tunnel on a bluff body which encountered a fluid with a high level of free stream turbulence at high Reynolds numbers. The main topic of the work was the effect of the interaction between the mean flow and free stream turbulence on the drag of bluff bodies. They described the main mechanisms whereby this interaction occurred to predict the effects of free stream turbulence at different locations. Three basic mechanisms were found: accelerated transition to turbulence, enhanced mixing and entrainment and the distortion of free stream turbulence itself by the mean flow. These mechanisms could act all together, even if at different points of the flow. It was proved that the effect of free-stream turbulence on drug reduction was to increase it. They also observed how the effects of turbulence changed by modifying the scale from a small value to a value comparable with the characteristic length of the bluff body. They did not arrive at any relevant conclusion because the effects of turbulence were completely random by acting on the scale of turbulence, namely they could be amplified, reduced or not modified at all. They concluded that high level free stream turbulence had significant effects on the flow over bluff bodies but they were not easily

predictable.

Maciejewski & Moffat (1992) investigated boundary layer heat transfer with very high free stream turbulence. The experiment was performed by placing a surface which had constant temperature at different locations in a turbulent free jet. They measured the heat transfer rate on the surface and and the level of turbulence in the free stream. They found that at high level of turbulence the heat transfer was increased more than it was predicted in previous experiments in which the level of turbulence was lower, considering the same Reynolds number. Their research was among the first to explain what happened at high intensity anisotropic turbulence. Ueda *et al.* (1997) experimentally studied velocity statistics along the stagnation line of an axi-symmetric stagnating turbulent flow. They took measurements of the instantaneous streamwise and normal velocity by using a laser-Doppler velocimetry. During the experiments they changed the turbulence level in the air flow by using a turbulence generator. In the previous experimental works the measurements were performed by hot-wire anemometry technique and this was a problem because flow was disturbed by the presence of the probe and the heat was lost from the hot wire to the wall. With the laser-Doppler velocimetry it was possible to take more accurate data close to the wall. Their results showed that with the installation of the turbulence generator, near the stagnation wall turbulence structures appeared. At high level of turbulence the streamwise mean velocity component was found to increase with increasing the distance from the wall until it started to increase linearly as in the case of low turbulence. The streamwise perturbation velocity component had the same behaviour of the mean velocity, while the normal perturbation velocity component increased by approaching the wall where it reached a maximum value.

1.2.2 DNS works

DNS and large eddy simulation (LES) have been widely used to study the flow around a bluff body. LES solves the low-pass filtered Navier-Stokes equations, as a result, LES resolves the large scale flow structures, but represents the effect of the small scale ones using subgrid-scale models.

Two examples of LES are presented in Xiong & Lele (2001) and Huai *et al.* (1999).

Xiong & Lele (2001) performed a large eddy simulation of leading-edge heat transfer under free-stream turbulence. The aim was to understand the mechanism of heat transfer augmentation and also to evaluate if LES could predict heat transfer processes in the gas turbine environment. This was of essential importance for the gas turbine design since combustors normally generate significant free-stream turbulence. They solved the three-dimensional compressible Navier-Stokes equations using a high-order finite difference method and an implicit time marching scheme. Numerical results showed that for small disturbance amplitudes the heat transfer increased significantly and also that when the disturbance length scale was increased, the enhancement decreased. They found an optimal length scale for which the heat transfer had its highest value. The free-stream turbulence was the cause of three main processes on the leading edge. The first one was the turbulence decay, the second one the inviscid distortion and finally the viscous interaction. The structures responsible for the heat transfer enhancement were found to be strong streamwise vortices on the wall. They used the local boundary layer thickness to characterise the scale of these structures at different Reynolds numbers. Their numerical results were in good agreement with experimental measurements only at relatively low Reynolds numbers, while for higher ones they used a hybrid simulation, namely LES method outside the boundary layer and a finer DNS-like grid within it because in the region close to

the wall smaller effects were present. Huai *et al.* (1999) computed the evolution of the disturbances leading to transition on a swept wedge by large-eddy simulation. The velocity and pressure were decomposed into a large-scale component and a subrigid-scale component and a filtering operation was applied to the continuity and Navier-Stokes equations in order to obtain the governing equations which were solved by using the fractional-time-step method. Their results showed that for stationary-crossflow-dominated transition the simulations were in agreement with the wind tunnel experiments and direct numerical simulations. They found the same shape of the structure and could predict the same transition location.

Thanks to DNS, some progress in understanding the effects of FST has been done, because DNS allows the visualization of typical flow structures. Most of the works focus on the downstream region of the body, without considering the interaction with the flow upstream, also known as *receptivity*. However, receptivity is very important to determine the correct amplitude of the perturbation flow inside the boundary layer and to understand how outer disturbances penetrate ad interact with the boundary layer.

Attention has been given to receptivity by Tempelmann *et al.* (2012), who investigated the linear receptivity of a swept-wing boundary layer by direct numerical simulation by solving the linearised Navier-Stokes equations. They assumed the disturbance to be periodic in time and spanwise direction and used Dirichlet boundary conditions. They focused on finding the optimal disturbance which gave the largest receptivity. They showed that the optimal surface roughness had the form of a wavy wall with maximum amplitude near the stagnation line and that under these conditions the boundary-layer receptivity was higher than to free-stream disturbances.

Some other relevant works on DNS is here reported to outline the state of the art.

Bae *et al.* (2003) performed a direct numerical simulation for stagnation point flow with free-stream turbulence given as a precomputed field of isotropic turbulence. Their objectives were to obtain realistic stagnation flow turbulence and to apply the results with the organised inflow disturbances in case of free-stream turbulence. They used an optimised finite difference scheme to reduce the computational cost of DNS. They considered a high Reynolds number based on a reference length scale and they set different values of intensity of the free-stream turbulence. They also changed the turbulence length scale, which was a multiple of the laminar boundary layer thickness. Their results showed that the streamwise vortices were stretched in the streamwise direction and because of this, the temperature field was also stretched in the same direction. The evolution of the streamwise vorticity outside the boundary layer made the turbulent diffusion of the normal mean momentum much larger than that of the streamwise one. They also investigated the evolution of flow structures in the stagnation region and demonstrated that outside the boundary layer the stretched structures were preserved, while in the stagnation region the near-wall flow structure was affected by the mechanism which also occurred in shear-layer flows. They concluded their paper by suggesting that the effect of large-scale edges played a fundamental role in the enhancement of the turbulent stagnation region heat transfer. Venema *et al.* (2014) simulated by direct numerical simulation the flow and the heat transfer in a tandem cylinder setup. Previous investigations had shown that free-stream turbulence caused an increase in the heat transfer near the stagnation region. The important parameters describing the models were the Reynolds number, the turbulence intensity and the turbulence length scale. They studied the mechanism for which the heat transfer increased and they also analysed the flow development and the turbulent structures. In particular they focused on the sensitivity of the heat transfer to the wake generator distance

because they were particularly interested in the location of the maximum heat transfer increase. Since in their DNS study they could not increase the Reynolds number to obtain the changing of wake, they increased the distance between the two cylinders. In this way the characteristic turbulence intensity was reduced. The results with larger distance between the cylinders were in good agreement with the experimental observations. They observed instantaneously the flow field and they found out that elongated flow structures which penetrated the boundary layer were the cause for the increase of the heat transfer. They finally pointed out that downstream of the stagnation point there probably was a larger heat transfer increase. In recent years many authors focused on receptivity in stagnation point boundary layer.

Obrist *et al.* (2012) investigated by DNS the transition mechanism into a swept Hiemenz boundary layer. The free stream flow was given by a mean flow with two superimposed stationary rotating vortex-like disturbances. The streaks created in the boundary layer could either decay or exhibit a secondary instability which then led to turbulence downstream, depending on the amplitude and frequency of the free-stream turbulence. The inflow boundary conditions for the perturbed flow were of Dirichlet type, while the outflow boundary conditions were of convective type. As initial condition to start the simulation they chose to use an unperturbed flow field. Their results showed that by keeping the same free-stream perturbation amplitude and changing the frequency, the breakdown to turbulence occurred at different streamwise positions. In particular, the breakdown was first reached in the medium frequency configuration, it was reached later in the slow frequency configuration and the streaks remained laminar in the fast frequency configuration. John *et al.* (2014) showed that the transition mechanism in the swept Hiemenz boundary layer could be stabilised by uniform wall suction. They performed a Fourier-Hermite spectral decomposition to estimate

the growth rate of the secondary instability. Their results showed that suction could reduce the growth rate of the secondary instability because it inhibited the growth of the streaks. In other words even if the growth rate was positive (but small) there may not be transition to turbulence due to the fact that the primary streaks decay quicker. They also studied the effect of changing the Reynolds number and demonstrated that by increasing it, the growth rate of the secondary instability became larger.

Guegan *et al.* (2007) used direct numerical simulation and a optimization algorithm to determine the optimal perturbation in swept Hiemenz flow. They superimposed to the analytical solution of swept Hiemenz flow an infinitesimal perturbation which was periodic in the spanwise direction. The optimal perturbation was the initial perturbation with the most amplified energy over a finite time and they found it to consist of spanwise vortices. Pérez *et al.* (2012) investigated the linear global instability of non-orthogonal incompressible swept attachment-line boundary-layer flow. They considered a basic flow given by the combination of a two-dimensional non-orthogonal flow and a swept flow and solved the governing equations numerically with a shooting method. They employed both the BiGlobal instability problem and DNS to analyse the linear instability and compared the two methodologies. Their interest was then focused on the model of the global instability and the effect of the α parameter on their numerical solutions, where α was the angle of attack. In particular they wanted to understand if the agreement between the two numerical methodologies employed was maintained by changing α. They showed that if α was decreased the flow is destabilised.

Mack *et al.* (2008) focused their attention to the connection between attachment-line and crossflow modes by using an iterative method together with direct numerical simulations. They considered a compressible flow around a parabolic body and they first studied the stability of a two-dimensional perturbation flow

superimposed to a two-dimensional base flow in order to use this base flow for the global stability analysis. They concluded that the global spectrum of a swept body contained both attachment-line modes and crossflow modes and their numerical results were in agreement with the previous experimental observations.

1.2.3 Theoretical works

In his most important work, Hiemenz in 1911 established that stagnation point flow admitted exact solutions of the Navier-Stokes equations. Sutera *et al.* (1963) performed a mathematical model of the sensitivity of heat transfer in the stagnation point boundary layer to free-stream vorticity. They were inspired by the experimental evidences that such vorticity, of small intensity in the free stream flow, amplified near the boundary layer. They considered a viscous, incompressible, steady flow with a small amount of vorticity added and transported by the mean stream. They focused on the region near the stagnation point, basically they chose a case very similar to Hiemenz flow but with vorticity. The solution of the perturbation flow differed from the classical Hiemenz solution because it described a three-dimensional flow field. They obtained a system of nonlinear partial differential equations whose unknown functions were the three perturbation velocity components. Because of the nonlinearity the components were coupled to each other, resulting in an exchange of energy among eddies of different size. They found out that the vorticity which entered the boundary layer being transported by the mean flow, was parallel to the wall and thus it had the orientation to be stretched in the stagnation point. This was the cause of the generation of three-dimensional effects within the boundary layer. From their model they also stated that only those components with wavelength equal to or larger than a cut-off wavelength could enter the boundary layer. However the process of nonlinearity generated vorticity of smaller scale within the boundary

layer.

Sadeh *et al.* (1970) analysed the vorticity amplification in a flow approaching a two dimensional stagnation point. Their work was based on the theory of Sutera *et al.* (1963) which stated that the main mechanism through which small turbulence in the free stream amplified at the wall was the vorticity amplification near the stagnation point. This theory was called *The vorticity amplification theory* and it was valid for a steady, two-dimensional stagnation flow of a viscous, incompressible fluid with constant properties. The considered case was very similar to the Hiemenz flow with the difference of added vorticity to the flow. According to this theory, the streamwise velocity component was the only one which was amplified in the stagnation point flow. Moreover the amplification depended on the wavelength of the vorticity, in particular only from a specific neutral wavelength there was amplification. The principal objective of Sadeh *et al.* (1970) was to extend the vorticity amplification model but considering the flow outside and far from the boundary layer. They considered a steady, viscous, incompressible flow past a circular cylinder with a superimposed sinusoidal perturbation. The considered Reynolds number was high ($\mathcal{O}(10^5)$). They started from the Hiemenz flow solution, namely from the linear variation of the velocity components near the stagnation point. Then they took an approximate form of this solution near the stagnation point for the mean flow and subsequently they tried a similar form solution for the perturbation velocity. By substituting it in the equations of the perturbation flow previously found, they numerically computed the perturbation velocity in the outer region. Their results showed the amplification of vorticity, by stretching mechanism namely the vorticity of scale larger than the neutral scale was amplified and it gave the input vorticity in the boundary layer.

A great deal of attention has been given to the stability of stagnation-point flows and bluff-body flows. Kestin & Wood (1970) investigated the stability of

two-dimensional stagnation flow showing that it was unstable if a three-dimensional disturbance was superimposed to the base flow. They considered an incompressible flow over a two-dimensional blunt body and pointed out that the mean velocity did not grow with y far away from the body, but it reached a constant mean value upstream which was used as outer boundary condition for the mean flow. A small disturbance periodic in the spanwise direction z direction was superimposed to the base flow and it was required that the perturbation amplitude vanished in the free stream. They derived the linearised equations for the perturbation flow by using the vorticity in order to eliminate the pressure and obtained the asymptotic solution of the vorticity as $\eta \to \infty$. They used the vorticity equation to analyse the spectrum and found that the flow was unstable and it consisted of counter-rotating vortices with a unique wavelength in the spanwise direction. Theofilis (1994) used a spectral method to obtain the solution of the Orr-Sommerfeld equation. He considered a three-dimensional Hiemenz base flow with a non-zero spanwise velocity component with a superimposed perurbation flow periodic in the spanwise direction. He derived the equations for the perturbation flow by using the velocity-vorticity form of the unsteady Navier-Stokes equations. As far field boundary conditions, the perturbation velocity and vorticity components were assumed to vanish. He simplified the linearised perturbation equations by assuming that the base flow had a predominant spanwise direction and he then found the Orr-Sommerfeld equation related with the disturbance. His results showed that the solution of the Orr-Sommerfeld equation could be used to predict the eigenspectrum for unstable and stable modes and in particular a couple of modes seemed to have similar frequencies and their interaction can lead to destabilisation of the boundary layer. Mack & Schmid (2011) investigated the global stability of a three-dimensional compressible supersonic flow around a parabolic body. The previous models consisted in breaking the

domain in two regions: the stagnation point and the downstream region where the boundary layer was three-dimensional. Their model gave a more complete vision of the perturbation dynamics. They decomposed the flow into a mean flow and a perturbation flow periodic in time and spanwise direction and substituted it into the Navier-Stokes equations obtaining a system of linear partial differential equations. They used iterative techniques such as the Arnoldi method in order to have stability information and employed the Cayley transformation to accelerate the convergence of the method. Their results showed that there were different modal structures. The boundary-layer modes which described the perturbation dynamics were vortices which became unstable for specific parameters. The acoustic modes were divided in two categories: wave structures and acoustic standing waves. The wavepacket modes were the equivalent of the continuous spectrum.

Theofilis (1993) performed a numerical study on the stability of the swept attachment line boundary layer. He used a shooting method to solve the equations for the three-dimensional base flow where a parameter was introduced in order to control the blowing/suction in the boundary layer. The perturbation equations were derived in the velocity-vorticity formulation and then discretized using a second-order finite difference scheme in the normal direction and a pseudospectral method in the spanwise direction. He assumed that only the chordwise velocity components of both the mean flow and perturbation flow depended on the chordwise coordinate. He then employied the Fourier transform to obtain a set of equations in spectral space for the perturbation flow. The no-slip condition at the wall for the streamwise and spanwise velocity components was set and the disturbance was assumed to vanish at large distances from the plate. He considered several cases for the normal velocity component at the wall which was the forcing term. He was among the first to use an initial value problem approach,

and his work is useful to study the stability a the attachment line. Brattkus & Davis (1991) studied the stability of stagnation-point flow for several disturbances. They set no-slip boundary conditions at the wall and vanishing boundary conditions at a large distance from the wall assuming the exponential decay of the disturbances and assuring a discrete spectrum model which means considering that the disturbance originates within the boundary layer. They considered long wave disturbances which slowly varied along the streamwise direction, self-similar disturbances which were of the same form of the base flow so that only the streamwise component depended on the streamwise coordinate, generalised Görtler disturbances which were an extension as a power series of the previous ones. Their results showed that the self-similar disturbances were the least stable.

The most relevant research efforts on receptivity are reported in the following works. They are certainly important to put the work herein presented in a broader context.

Goldstein & Atassi (1976) developed a complete second-order theory for the unsteady flow about an airfoil due to a periodic gust. This theory had been developed before but in the linearized approximation giving the same results of a flat plate with no thickness and angle of attack. They included two small parameters to formulate the problem correctly: the amplitude of the incident disturbance and the angle of attack. They supposed that the amplitude of the gust was much smaller than the amplitude of the mean velocity and that it was of the same order of the angle of attack. The effect of including these parameters was the distortion of the initial gust by the mean potential flow over the body, which induced variations of the wavelength, amplitude and phase of the incident vorticity. They formulated the problem considering a two-dimensional airfoil immersed in an incompressible flow with a small amplitude perturbation in the free stream flow. The solution of the linearized governing equations describing the problem

were evaluated by taking an asymptotic expansion of the inner region, namely the boundary region. The boundary conditions were obtained by matching the outer expansion solution. They obtained an explicit solution for the simplest case of zero-thickness airfoil. They could not superimpose all the parameters because the problem would have became nonlinear. Thomas *et al.* (2015) were interested in the receptivity process in the swept Hiemenz boundary layer which was characterized by the initial flow properties. They considered an incompressible viscous flow and used the vorticity form of the Navier-Stokes equations to find the governing disturbance equations. The perturbation was considered periodic in the spanwise direction and it was represented by a Fourier series. They forced the flow using suction or blowing at the plate surface distributed as periodic holes. Once the perturbation flow was generated inside the boundary layer they could calculate the receptivity amplitude of the disturbance and this was found to be independent by the wall forcing. The linear analysis showed that the receptivity amplitude was linearly proportional to the absolute maximum value of the perturbation velocity.

Obrist & Schmid (2011) extended the flow solution of swept Hiemenz flow to a swept bluff body flow which consisted of a three-dimensional boundary layer, an inviscid stagnation-point flow and an outer parallel flow. They showed that in the Hiemenz model the outer boundary conditions for the perturbation flow were valid under the assumption that the Hiemenz solution was valid everywhere, but it was only valid at the stagnation point. In their model they used a different base flow and inserted it into the stability equations in order to find diverging modes. By using the wave packet pseudomodes theory they derived the appropriate outer boundary conditions. Their results showed how the modes are connected with the outer flow and they could be used to study the receptivity of leading-edge boundary layer. Criminale *et al.* (1994) investigated the evolution of disturbances in

stagnation-point flow by considering a small perturbation of a three-dimensional base flow. The linearised equations for the disturbance were written in terms of the vorticity and the boundary conditions were the no slip condition at the wall and the disturbance vanished at large distance from the plate. The initial condition was derived considering that the disturbance at initial time was bounded in all directions. The coordinates were changed from Cartesian to moving coordinates with the advantage that in this new coordinate system the coefficients of the equations only depended on time. They then employed Fourier transforms in the new directions and found the analytical solution of the disturbance equations. They showed that while the planar stagnation-point flow was stable, the fully three-dimensional flow could be stable or unstable depending on the position along the transverse direction.

Lorna & Peake (2016) presented an analytic model which predicted the inviscid response to upstream turbulence with the leading-edge stagnation point of a thin aerofoil. They initially considered one Fourier mode upstream and used Goldstein (1978) solution for the vortical velocity components. They found an analytical solution at leading order by considering both high and low frequencies. In order to do that, they needed to do some approximations such as the Mach number and body thickness had to be small. Moreover they had to consider a new asymptotic region to avoid the singularity at the leading edge. They used this solution to consider the effect of homogeneous weak turbulence upstream. Their results were in a good agreement with the experimental results only for high frequencies and their model did not include viscous and nonlinear effects.

van Driest & Blumer (1963) used the boundary layer solution of Pohlhausen and Falkner-Skan to calculate the effect of pressure gradient on transition. They introduced the disturbance in the flow, they used the Taylor method which consists in assuming that the pressure disturbances distort the boundary layer. Their

results showed that for the stagnation point flow the Polhausen and Falkner-Skan solutions were in good agreement. Xiong & Lele (2004) studied the distortion of upstream disturbances in a Hiemenz boundary layer, considering an unsteady incompressible viscous flow. The flow was given by the combination of a steady two-dimensional mean flow modelled by the Hiemenz boundary-layer flow and an unsteady three-dimensional perturbation flow. They assumed that the length scale of the disturbance was much larger than the boundary-layer thickness. The perturbation was considered periodic in time and spanwise direction so that it could be expanded in a double Fourier series and only the streamwise velocity component depended on the streamwise coordinate. They studied the effect of the perturbation wavelength and amplitude on the numerical solution found using the over-relaxation method. They also found a composite asymptotic solution for the vortical disturbances which was valid both inside and outside the Hiemenz boundary layer. The asymptotic solution was obtained as an explicit dependence on the disturbance length scale and frequency and they concluded that the parameter responsible for the amplification of the incoming vorticity was the ratio between the disturbance length scale and the boundary-layer thickness.

Obrist & Schmid (2010) investigated the continuous spectrum and effect of free-stream turbulence on a swept Hiemenz flow, focusing on algebraically decaying modes. They performed the analysis using wave packet pseudo-modes which was an approximation of the governing equations similar to WKBJ method. Their results confirmed that the swept Hiemenz flow had a continuous spectrum in the complex plane bounded by the imaginary part of eigenvalues. The modes of the continuous spectrum represented decaying wave solutions which had the physical meaning of the communication between the free-stream and the boundary layer and they were then relevant for receptivity studies. Gorla (1978) investigated the response of an axisymmetric stagnation flow to transient free stream velocities.

The equations were derived and solved numerically by a fourth order Runge-Kutta method. The results were obtained for two different cases: the first one was the case where the inviscid flow changed with constant acceleration and the second case was where the free stream velocity changed exponentially with time. In both cases the shear stress first increased and then decreased with time and its maximum value depended on Reynolds number.

In his thesis, Turner (2005) analyzed the evolution of T-S waves over objects of different geometries, among which was a Rankine body. He observed that the mean pressure gradient on a Rankine body was adverse for the majority of the body surface; he performed studies on the effect of the pressure gradient on the position of the stability point and his results showed that for favourable pressure gradients the stability point moved downstream while for adverse pressure gradient it moved upstream. The amplitude of the T-S waves was influenced by the position of the stability point, in particular the amplitude was increased for adverse pressure gradients.

Rapid distortion theory

Rapid distortion theory is a method for calculating rapidly changing turbulent flows under the action of different kinds of distortion, such as large-scale velocity gradients. Inspired by Taylor (1935), who calculated the effects of stream distortion on a turbulent flow where the disturbance was sinusoidal, Batchelor & Proudman (1954) obtained the effect of rapid distortion on homogeneous turbulence. They considered the Fourier transform of the turbulent motion and they integrated Taylor (1935)'s results. They focused on changes occurring in a homogeneous turbulent motion when a uniform distortion is added. They were interested in the changes on properties of a turbulent motion caused by imposing distortions, because it was empirically known that they could drastically change.

Distortions occur in wind tunnels when there is a reduction in the work sectional area. A distortion could also be seen as large-scale variation of turbulent motion, as it produced small-scale velocity variations which could see the large-scale strain as a superimposed distortion. Even if their results were very interesting, they could not be validated with experiments because it was really difficult to obtain distortion so rapid.

Hunt (1973) generalised the rapid distortion theory developed by Batchelor & Proudman (1954) by calculating the turbulent velocity around a bluff body outside of the boundary layer and upstream. The solution to the equations which he obtained could be found only if the scale of the disturbance was not of the same order of the characteristic length of the body, because in this case the computing time was very high. He just showed a qualitative behavior of the velocity when the two scales were comparable. The theory developed by Hunt (1973) explained different mechanisms, such as the governing physical processes of distortion of the turbulence by the mean flow, the arrest of turbulence by the body and the concentration of vortex lines at the body's surface. His research was really interesting for many different reasons. First of all it was the first work which differed from the other studied cases (Batchelor & Proudman, 1954). Secondly it gave an overview of the effects of turbulence on boundary layer transitions for bluff bodies and finally it could be applied to many real situations where a turbulent flow streamed around obstacles of generic shapes. He based his work on rapid distortion theory, thus he assumed that each eddy did not exchange energy with other Fourier components but it was just affected by the mean flow. Under this hypothesis the problem was linear and then it could be solved by mathematical methods. Differently from Batchelor & Proudman (1954) , Hunt (1973) considered non-homogeneous distortion, namely the scale of the turbulence did not allow the neglect of the mean flow velocity gradient. Moreover he imposed the

boundary condition on the turbulence that the velocity normal to the surface of the body was zero. The body chosen for the analysis was a circular cylinder but the results could be extended to any body. Even if some of the assumptions made were not realistic and the analysed turbulent flow was not physically realisable everywhere around the body, the results could be used to predict some experimental results. In the paper he briefly discussed the comparison between his theory and the experiments of Bearman (1972). Theory and experiments both showed that when the scale of the disturbance was low, high-frequency components of the streamwise velocity were amplified while low-frequency components were reduced near the stagnation streamline.

Goldstein (1978) also worked on rapid distortion theory, to extend the work of Hunt (1973). He considered compressible flows, with no restrictions on the Mach number value with high Reynolds numbers and he started from the linear inhomogeneous wave equation of a potential function associated with the perturbation velocity. As usual, he assumed that the upstream disturbance was a small perturbation of the constant velocity mean flow. He showed that the perturbation velocity consisted of two parts: one was a known function of the imposed upstream distortion and the mean flow, it was also called gust and it was purely convected, it had zero-divergence and it was decoupled from the fluctuations in pressure; the other one was an irrotational disturbance, given by the gradient of the potential function which was the solution of the wave e equation and it was related to pressure fluctuations. The source term of the inhomogeneous wave equation was found to be zero upstream because it was given by the divergence of the density multiplied by the perturbation velocity. Since the density was considered constant upstream and one of the assumption was that the imposed perturbation satisfied the continuity equation, namely its divergence was equal to zero, the source term was zero upstream and then the solution of the homoge-

neous wave equation was zero in this region. However, approaching the body, the perturbation was distorted by the mean flow and thus its divergence was different from zero, resulting in a source term in the wave equation and then a non-zero solution for it, at finite distances from the obstacle. The potential velocity field produced by the distortion gave pressure fluctuations. Remembering that the perturbation velocity was given by two parts and noticing that the first one was not zero in general at the wall, then the second part given by the potential flow had to balance it to satisfy the boundary condition. Thus, even if the effect of the distortion of the mean flow was not considered, pressure fluctuations would still have been produced. From a mathematical point of view, pressure fluctuations could then be seen as a necessary term to balance the fluctuations in momentum which arised from the distortion of the gust by the mean flow around the object.

Goldstein (1984) focused on the solution of the external flow around a body of generic shape where a small-amplitude, unsteady, viscous motion was imposed on steady potential flow. He derived the equations for the perturbation velocity and then divided the solution for it in two parts: the first one is the homogeneous solution which satisfies the momentum equation without the forcing term (namely without the pressure gradient); the second one is the potential solution, from which the outer pressure is derived. The total perturbation velocity is given by the summation of these two solutions. He first found the homogeneous solution by WKBJ theory, a method to find the solution of partial differential equations and then from the continuity equation he calculated the potential solution. By using this theory he looked for the phase and the amplitude of the perturbation velocity. The equation for the phase in a new coordinate system is found to be the Eikonal equation. He found a complete analytic solution of the perturbation velocity by changing coordinates. This change of coordinates will be better explained in the next chapter and it is very important because it will be used in this project.

Goldstein (1984) supposed that the steady potential flow is not influenced by viscous effects and to study the problem he included viscous effects in rapid distortion theory. He used his results to calculate the flow over a circular cylinder and he showed the numerical results for large Reynolds numbers. In particular he focused on the behavior of the streamwise perturbation component velocity along the mean flow stagnation streamline. Its absolute value vanishes when the dimensionless wavenumbers along the perpendicular directions go either to zero or infinity. Moreover, plots of the same function versus the streamwise coordinate show that it decreases as the coordinate goes to zero. Finally, it is very important to remark that these results are valid just for high Reynolds numbers.

1.3 Objectives

In the literature, several theories have been presented to understand the transition from laminar to turbulence. However, to the author's best knowledge, very few publications can be found in the literature that address the issue of understanding the evolution of Klebanoff modes on bluff bodies. The interaction between the outer flow and the flow inside the boundary layer has been scarcely investigated from the theoretical point of view.

The major lack in the literature is that most of the previous studies do not take into account the outer flow dynamics which is fundamental to determine the correct amplitude of the streaks. Even though the dynamics of the streaks has been widely investigated in recent years, most results have been obtained without considering the outer flow dynamics and the perturbation at the leading edge or stagnation point. Nonetheless, it is possible to further explain the evolution of the streaks by using the proper mathematical formulation. With this goal, this work seeks to analyse the dynamics of the Klebanoff modes on a bluff body in order to make a contribution to understanding the transition to turbulence. In particular

a Rankine body, obtained by the combination of a uniform flow with a source, is considered because it is representative of many engineering systems. Two main issues arise when dealing with the analysis of combined pressure gradient and curvature on the pre-transitional boundary layer.

- It is important to identify the streaks with accelerating mean flow.
- It is crucial to compute the outer flow dynamics

Based on the approach presented in Leib *et al.* (1999), we present a rigorous mathematical approach which consists of analysing the outer perturbation flow and deriving the boundary region equations. Furthermore the correct initial conditions are used to initiate the numerical simulations.

The results could eventually lead to a better understanding of the dynamics of several physical mechanisms.

2. MATHEMATICAL FORMULATION

We consider a uniform flow of velocity U_∞^* encountering a large scale bluff body. We chose a Rankine body since several engineering systems such as submarines, turbine blades, airplane wings can be well represented by it. The stagnation point is the first region encountered by the flow and the velocity here is zero. The curvature is responsible for a mean pressure gradient. When the flow encounters the body a laminar viscous boundary layer is created on its surface.

A small amplitude, unsteady, three-dimensional kinematic perturbation flow is superimposed to the base flow. The free-stream disturbance is assumed of the convected gust type at sufficiently large distance from the body, an excellent model for oncoming turbulent flows of small amplitude, as if it was generated by a grid. When the flow encounters the body both the mean and the perturbation flow are distorted and they become parallel downstream. Figure 2.1 shows the Rankine body and the flow generated by the grid. The origin of the Cartesian and polar coordinate system is at the point source. The flow moves in the streamwise direction. A rotated Cartesian coordinate system is used at the stagnation point with origin located at the stagnation point.

A Rankine body is represented mathematically by a uniform flow which encounters a source flow (Anderson (2007)). The domain is divided in two asymptotic regions, corresponding to region III and IV of Leib *et al.* (1999): the outer region around the body where the mean flow is inviscid and the inner thin viscous boundary layer region. We only consider two asympotic regions because the boundary layer of a Rankine body has a thickness at the stagnation point,

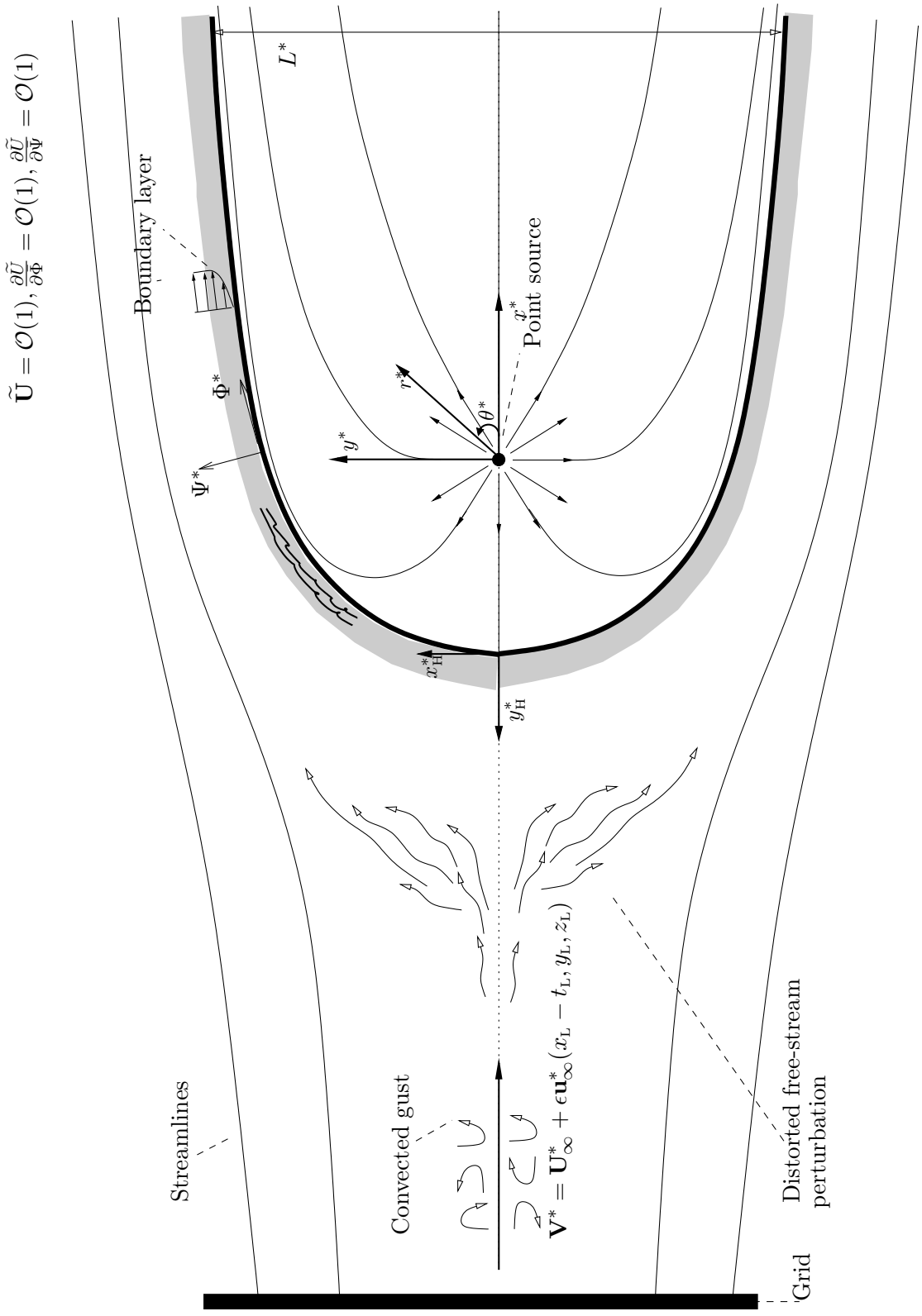

Fig. 2.1: Perturbed flow around the body. The origin of Cartesian and polar coordinate system is at the point source. At the stagnation point a rotated coordinate system is used.

therefore the perturbation flow inside the boundary layer is three dimensional alongside the whole body's surface as in region III of Leib *et al.* (1999). The outer flow of a Rankine body is displaced at the stagnation point and around the body as in region IV of Leib *et al.* (1999). In both regions the flow is decomposed into a mean flow and a perturbation flow. The outer mean flow is inviscid, two-dimensional, given by a uniform flow encountering the flow produced by a point source and it is displaced by the presence of the body. The displacement effect is due to the actual viscous flow in the boundary layer. The streamline external to the boundary layer is deflected upward a distance which is exactly the boundary layer thickness. The displacement effect gives rise to the concept of an effective body, namely the free stream sees the contour of the boundary layer as if it was the body. The mean pressure is computed by the Bernoulli equation. It is assumed that the outer perturbation flow has a periodic modulation along the spanwise direction and time and that its spatial scales are much smaller that the mean-flow scale. Helmholtz decomposition is used to decompose the velocity into a homogeneous part and a potential contribution related to the pressure. It will be shown that the outer perturbation pressure is of the same order of the inner perturbation pressure, which means that the perturbation pressure inside the boundary layer does not decay far from the body, unlike what happens on a flat plate. As for the free-stream, the boundary layer flow is divided in a mean flow and in a perturbation flow, both viscous. The mean boundary layer flow is two-dimensional and for this reason a streamfunction can be defined, in analogy with Blasius flow. This streamfunction depends on an unknown function F which has a relationship with both of the components of the mean flow velocity. By substituting these relationships in the equations of the mean flow, a nonlinear third order equation for F is obtained. This equation is the steady nonlinear equation for the mean flow with no similarity, because there is a dependence

on the streamwise variable. The solution of the inner mean flow is known at the stagnation point, it is called the Hiemenz solution. The inner perturbation flow is viscous and three-dimensional and it is governed by the boundary region equations. Once the velocity and pressure disturbance are obtained everywhere outside of the thin boundary layer, they are used to formulate the outer boundary conditions of the boundary region equations. Although the asymptotic matching is employed to find the composite mean flow, the same approach cannot be used for the perturbation flow. The reason is that the solution of the outer perturbation flow is obtained in a region where the outer mean velocity and its derivatives are of order 1, because at the stagnation point the velocity is zero thus there is a singularity. Since the integral is evaluated from upstream, the outer solution is unknown for small streamlines alongside the body. Therefore the outer boundary conditions for the boundary region equations are imposed at sufficiently large distance from the body, without using the asymptotic matching. Initial conditions are necessary to start the numerical computation and they are obtained by making assumptions on the flow near the stagnation point. Table 2.1 gives an overview of the asymptotic regions around the Rankine body.

2.1 Scaling

In this section the appropriate scaling is described. All the dimensional quantities are marked by the symbol $*$. Lengths which are scaled by L^* are indicated by the subscript L. L^* is the characteristic thickness of the Rankine body at infinite downstream distance as shown in figure 2.1. Lengths which are scaled by λ_z^*, which is the spanwise disturbance wavelength, do not have any subscript. The velocity components are made dimensionless by U_∞^*, pressure by $\rho^* U_\infty^{*2}$ where ρ^* is the density and time by L^*/U_∞^*.

The upstream turbulence is represented by a convected perturbation of the

uniform mean flow U^*_∞, namely the flow upstream is

$$\mathbf{V} = \hat{i} + \epsilon \mathbf{u}_\infty(x - t, y, z), \tag{2.1}$$

where $\mathbf{V} = (u, v, w)$ is the dimensionless velocity vector and

$$\mathbf{u}_\infty = \hat{\mathbf{u}}^\infty e^{i(k_\Phi x + k_\Psi y + k_z z - k_\Phi t)} + c.c., \tag{2.2}$$

with , $k_\Phi = 2\pi\lambda^*_z/\lambda^*_\Phi$, $k_\Psi = 2\pi\lambda^*_z/\lambda^*_\Psi$, $k_z = 2\pi$; λ^*_Φ,λ^*_Ψ,λ^*_z are the wavelengths in the streamwise, normal and spanwise directions and k_Φ, k_Ψ, k_z are the dimensionless wavenumbers. We are going to consider only one mode of the spectrum of the oncoming turbulence.

The mean flow with components ($\widetilde{U}$,$\widetilde{V}$) is uniform upstream but it becomes non-uniform moving downstream. There is a region around the body where derivatives of the mean flow are of order 1.

2.2 Optimal coordinates

Since the body is not a flat plate, it is convenient to work in a special coordinate system. In this section the change of coordinates is explained.

The continuity and Navier-Stokes equations have to be satisfied by both the mean and the perturbation flow

$$\nabla \cdot \mathbf{V} = 0, \tag{2.3}$$

$$\frac{\partial \mathbf{V}}{\partial t_{\mathrm{L}}} + \mathbf{V} \cdot \nabla \mathbf{V} = -\nabla p + \frac{1}{R_{\mathrm{L}}} \nabla \cdot (\nabla \mathbf{V}), \tag{2.4}$$

where $R_{\mathrm{L}} = U^*_\infty L^*/\nu^* \gg 1$ is the Reynolds number.

The new set of coordinates Φ_{L}, Ψ_{L}, z is employed, where Φ_{L} is the potential and Ψ_{L} is the streamfunction of the inviscid mean flow in planes perpendicular to the spanwise direction z, which can be used because the mean flow is independent

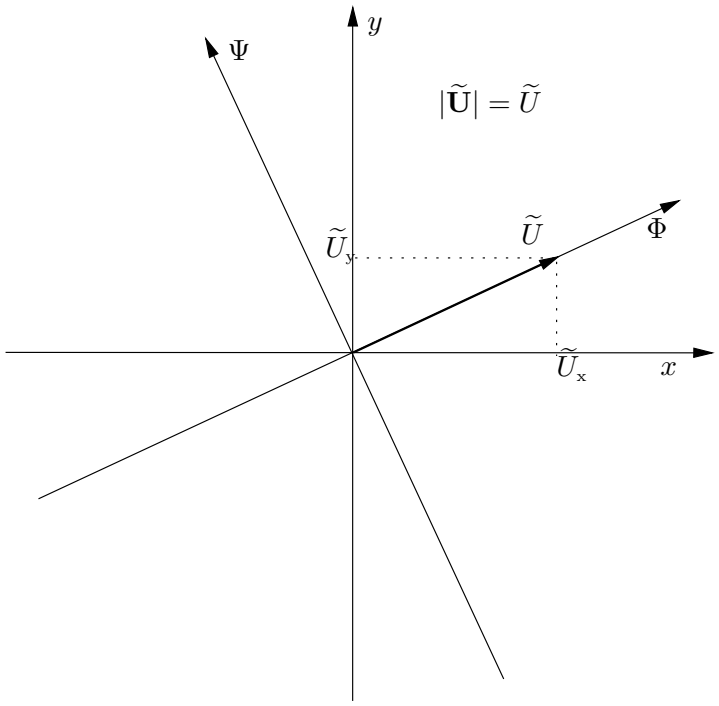

Fig. 2.2: Outer potential velocity in x-y plane and Φ-Ψ plane.

from z. The streamwise coordinate x_{L} is replaced by the outer mean-flow velocity potential Φ_{L} and the wall normal coordinate y_{L} is replaced by the outer mean-flow streamfunction Ψ_{L}. Upstream, where the flow is parallel, $\Phi_{\mathrm{L}} = x_{\mathrm{L}}$ and $\Psi_{\mathrm{L}} = y_{\mathrm{L}}$. These coordinates are called optimal coordinates or Kaplun coordinates because he was the first one to introduce them in his thesis (Kaplun, 1954).

The velocity $\widetilde{\mathbf{U}}$ is a vector in the Φ direction, because by definition a potential flow is along constant streamlines. Thus it has two components in the x-y plane, but just one component in the Φ-Ψ plane along Φ. This means that the absolute value of the velocity is the same value as the Φ-component, namely

$$|\widetilde{\mathbf{U}}| = \widetilde{U}.$$

Figure 2.2 shows the just explained relationship, which will be used when the coordinates of the equations are changed.

The reason why it is convenient to change coordinates and in particular to choose the potential and streamfunction as new coordinates is that in this new system the body can be treated as a flat plate, because the stream lines follow the shape of the body as shown in Figure 2.3. In Appendix A continuity and Navier-Stokes equations in optimal coordinates are derived and they are

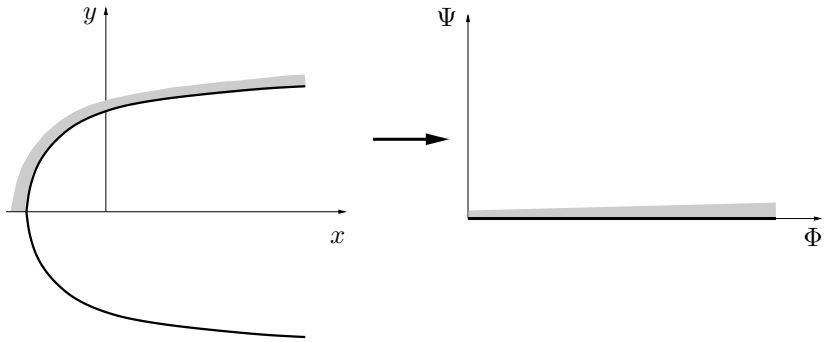

Fig. 2.3: Change of coordinates.

$$\widetilde{U}\frac{\partial w_\Phi}{\partial \Phi_\mathrm{L}} + \widetilde{U}\frac{\partial w_\Psi}{\partial \Psi_\mathrm{L}} + \frac{\partial w_z}{\partial z_\mathrm{L}} = 0, \tag{2.5}$$

$$\begin{aligned}\frac{1}{\widetilde{U}^2}\frac{\partial w_\Phi}{\partial t_\mathrm{L}} + w_\Phi\frac{\partial w_\Phi}{\partial \Phi_\mathrm{L}} + w_\Psi\frac{\partial w_\Phi}{\partial \Psi_\mathrm{L}} + \frac{1}{\widetilde{U}}w_z\frac{\partial w_\Phi}{\partial z_\mathrm{L}} + \frac{\partial \ln\widetilde{U}}{\partial \Phi_\mathrm{L}}\left(w_\Phi^2 + w_\Psi^2\right) = -\frac{1}{\widetilde{U}^2}\frac{\partial p}{\partial \Phi_\mathrm{L}} + \\ \frac{1}{R_\mathrm{L}}\left[\frac{\partial^2 w_\Phi}{\partial \Phi_\mathrm{L}^2} + \frac{\partial^2 w_\Phi}{\partial \Psi_\mathrm{L}^2} + \frac{1}{\widetilde{U}^2}\frac{\partial^2 w_\Phi}{\partial z_\mathrm{L}^2} - 2\frac{\partial \ln\widetilde{U}}{\partial \Psi_\mathrm{L}}\left(\frac{\partial w_\Psi}{\partial \Phi_\mathrm{L}} - \frac{\partial w_\Phi}{\partial \Psi_\mathrm{L}}\right) - \frac{2}{\widetilde{U}}\frac{\partial \ln\widetilde{U}}{\partial \Phi_\mathrm{L}}\frac{\partial w_z}{\partial z_\mathrm{L}}\right],\end{aligned} \tag{2.6}$$

$$\begin{aligned}\frac{1}{\widetilde{U}^2}\frac{\partial w_\Psi}{\partial t_\mathrm{L}} + w_\Phi\frac{\partial w_\Psi}{\partial \Phi_\mathrm{L}} + w_\Psi\frac{\partial w_\Psi}{\partial \Psi_\mathrm{L}} + \frac{1}{\widetilde{U}}w_z\frac{\partial w_\Psi}{\partial z_\mathrm{L}} + \frac{\partial \ln\widetilde{U}}{\partial \Psi_\mathrm{L}}\left(w_\Phi^2 + w_\Psi^2\right) = -\frac{1}{\widetilde{U}^2}\frac{\partial p}{\partial \Psi_\mathrm{L}} + \\ \frac{1}{R_\mathrm{L}}\left[\frac{\partial^2 w_\Psi}{\partial \Phi_\mathrm{L}^2} + \frac{\partial^2 w_\Psi}{\partial \Psi_\mathrm{L}^2} + \frac{1}{\widetilde{U}^2}\frac{\partial^2 w_\Psi}{\partial z_\mathrm{L}^2} + 2\frac{\partial \ln\widetilde{U}}{\partial \Phi_\mathrm{L}}\left(\frac{\partial w_\Psi}{\partial \Phi_\mathrm{L}} - \frac{\partial w_\Phi}{\partial \Psi_\mathrm{L}}\right) - \frac{2}{\widetilde{U}}\frac{\partial \ln\widetilde{U}}{\partial \Psi_\mathrm{L}}\frac{\partial w_z}{\partial z_\mathrm{L}}\right],\end{aligned} \tag{2.7}$$

$$\begin{aligned}\frac{1}{\widetilde{U}^2}\frac{\partial w_z}{\partial t_\mathrm{L}} + w_\Phi\frac{\partial w_z}{\partial \Phi_\mathrm{L}} + w_\Psi\frac{\partial w_z}{\partial \Psi_\mathrm{L}} + \frac{1}{\widetilde{U}}w_z\frac{\partial w_z}{\partial z_\mathrm{L}} + w_z\left(w_\Phi\frac{\partial \ln\widetilde{U}}{\partial \Phi_\mathrm{L}} + w_\Psi\frac{\partial \ln\widetilde{U}}{\partial \Psi_\mathrm{L}}\right) = -\frac{1}{\widetilde{U}^3}\frac{\partial p}{\partial z_\mathrm{L}} + \\ \frac{1}{R_\mathrm{L}}\left[\frac{\partial^2 w_z}{\partial \Phi_\mathrm{L}^2} + \frac{\partial^2 w_z}{\partial \Psi_\mathrm{L}^2} + \frac{1}{\widetilde{U}^2}\frac{\partial^2 w_z}{\partial z_\mathrm{L}^2} + \frac{w_z}{\widetilde{U}}\left(\frac{\partial^2 \widetilde{U}}{\partial \Phi_\mathrm{L}^2} + \frac{\partial^2 \widetilde{U}}{\partial \Psi_\mathrm{L}^2}\right) + 2\left(\frac{\partial w_z}{\partial \Phi_\mathrm{L}}\frac{\partial \ln\widetilde{U}}{\partial \Phi_\mathrm{L}} + \frac{\partial w_z}{\partial \Psi_\mathrm{L}}\frac{\partial \ln\widetilde{U}}{\partial \Psi_\mathrm{L}}\right)\right].\end{aligned} \tag{2.8}$$

The three velocity components w_Φ, w_Ψ and w_z are along the streamlines, the potential lines which are parallel to the streamlines and the spanwise direction respectively.

To enable us to derive the equations for the mean and the perturbation flow, several hypothesis have been made.

- High Reynolds numbers based on the characteristic length of the body are considered.

- Periodicity of the perturbation flow is assumed along z and t.

- The amplitude of the perturbation velocity is much smaller than the amplitude of the mean flow. This hypothesis allows having linearised equations for the perturbation flow. The linearity is expressed mathematically by $\epsilon/k_\Phi \ll 1$ inside the boundary layer and terms of order ϵ^2 are neglected in the equations.

- $k_\Phi \ll 1$, where $k_\Phi = 2\pi\lambda_z^*/\lambda_\Phi^*$ is the dimensionless streamwise wavenumber, λ_Φ^* is the streamwise wavelength and λ_z^* is the spanwise wavelenght. This hypothesis can also be expressed as $\lambda_\Phi^* \gg \lambda_z^*$, following the experimental results which show that the streaks are elongated in the streamwise direction. Since for a flat plate k_Φ does not depend on the streamwise coordinate, we assume that it is the same for a Rankine body.

- λ_z^* and λ_Ψ^* are of the same order, where λ_Ψ^* is the normal wavelength.

- λ_Φ^* is of the same order as L^*, the characteristic length of the body. Since the outer mean flow evolves on scales of order L^*, this hypothesis states that the scale of the mean flow is the same as the streamwise scale of the perturbation.

- $\bar{\Phi} = k_\Phi\Phi$. The barred variables indicate quantities scaled by λ_Φ^*. Following the previous hypothesis, the mean flow is a function of $(\bar{\Phi}, \bar{\Psi})$ while the perturbation flow is a function of $(\bar{\Phi}, \Psi, z, t)$.

- $\bar{t} = k_\Phi t$. The time is also scaled by λ^*_Φ because the streaks modulate slowly in time.

- $Rk_\Phi = \mathcal{O}(1)$, where R is the Reynolds number based on λ^*_z.

2.3 The mean flow

2.3.1 Outer mean flow

In this section the outer mean flow is presented. Here the displacement due to the boundary layer is not considered as we are interested to show the outer mean velocity alongside the body's surface. As in Anderson (2007), a combination of uniform flow with a source is well represented in a polar coordinate system,

$$r = \sqrt{x_{\mathrm{L}}^2 + y_{\mathrm{L}}^2}, \qquad \theta = \operatorname{atan}\left(\frac{y_{\mathrm{L}}}{x_{\mathrm{L}}}\right), \tag{2.9}$$

$$\Psi_{\mathrm{L}} = r\sin\theta + \frac{\Lambda\theta}{2\pi} - \frac{\Lambda}{2}, \tag{2.10}$$

$$\Phi_{\mathrm{L}} = r\cos\theta + \frac{\Lambda}{2\pi}\ln r - \frac{\Lambda}{2\pi}\left[\ln\left(\frac{\Lambda}{2\pi}\right) - 1\right], \tag{2.11}$$

where $\Phi_{\mathrm{L}} = \Phi^*/(U^*_\infty L^*)$ is the potential, $\Psi_{\mathrm{L}} = \Psi^*/(U^*_\infty L^*)$ is the streamfunction associated with the outer mean flow as already defined. Λ is the dimensionless strength of the source.

The absolute value of the mean outer velocity can be found analytically as a function of r and θ.

$$\widetilde{U} = \sqrt{\left(\frac{\partial\Phi_{\mathrm{L}}}{\partial r}\right)^2 + \left(\frac{1}{r}\frac{\partial\Phi_{\mathrm{L}}}{\partial\theta}\right)^2} = \sqrt{1 + \frac{\Lambda\cos\theta}{\pi r} + \frac{\Lambda^2}{4\pi^2 r^2}}, \tag{2.12}$$

and therefore the potential, streamfunction and the mean velocity are found explicitly as functions of r and θ. However, we need the absolute value of the mean outer velocity in optimal coordinates, because the analysis is performed in these coordinates. It is not possible to invert analytically the relationships

	Mean flow	**Perturbation flow**
Outer	• Inviscid-2D. • Uniform plus source flow. • Pressure gradient. • Stagnation point: Hiemenz flow ***Section 2.3.1***	• Viscous-3D. • Pressure gradient. ***Section 2.4.1***
Inner	• Viscous-2D. • Steady nonlinear mean flow equation in optimal coordinates. ***Section 2.3.2***	• Viscous-3D. • Boundary layer equations. • Outer flow used to obtain boundary conditions. • Derivation of initial conditions. ***Section 2.4.2***

Tab. 2.1: Decomposition of the flow around the Rankine body.

between r-θ and Φ-Ψ, thus this is performed numerically by using a Newton-Raphson algorithm. The algorithm is explained in detail in section 3.1.1.

It is interesting to know the distance between the source point and the stagnation point. In order to do that, we start from the expression of r as function of θ and Ψ_{L}

$$r = \frac{1}{\sin\theta}\left(\Psi_{\mathrm{L}} - \frac{\Lambda\theta}{2\pi} + \frac{\Lambda}{2}\right).$$

It is clear that $r = \infty$ at $\theta = 0$ and $\theta = \pi$. This can also be observed in Figure 2.1, because at these two angles the radius is parallel to the streamlines. There is an exception on the body, where $\Psi_{\mathrm{L}} = 0$. Here, the expression of r is

$$r = \frac{\Lambda(\pi - \theta)}{2\pi\sin\theta},$$

and r at $\theta = \pi$ can be easily calculated. This value is the distance between the stagnation point and the origin of the Cartesian coordinate system. It is found to be

$$r = \frac{\Lambda}{2\pi}.$$

Asymptotic behavior of the mean velocity at the stagnation point in Cartesian coordinates

In this section the outer mean velocity at the stagnation point is found as function of the Cartesian coordinates x_{L}-y_{L}. The mean outer velocity field near the stagnation point is known as Hiemenz flow velocity and it is given in Schlichting (1979) in dimensional form as $u^*_{\mathrm{H}} = a^* x^*_{\mathrm{H}}$, where $a^* = (\alpha U^*_\infty)/L^*$ and α is a constant which depends on the strength of the source. In figure 2.1 it is shown where the origin of the x_{HL}-y_{HL} plane is. It is the coordinate system with origin at the stagnation point, very suitable to analyse the flow in this region. Since

x_{H}^* is small at the stagnation point because it is just near the origin, u_{H}^* is small and α is of order 1. To demonstrate that α is of order 1, we start from the streamfunction (2.10) and (2.9) is substituted into it to obtain

$$\Psi_{\mathrm{L}} = \sqrt{x_{\mathrm{L}}^2 + y_{\mathrm{L}}^2} \sin\left(\arctan\frac{y_{\mathrm{L}}}{x_{\mathrm{L}}}\right) + \frac{\Lambda}{2\pi}\arctan\frac{y_{\mathrm{L}}}{x_{\mathrm{L}}} - \frac{\Lambda}{2}. \tag{2.13}$$

In order to calculate u_{H}, the derivative of the streamfunction with respect to x_{L} is calculated. The streamfunction is derived with respect to x_{L} because the streamwise velocity component u_{H} at the stagnation point corresponds to the normal velocity component in the x_{L}-y_{L} plane as the coordinates rotate at the stagnation point (see Figure 2.1).

$$u_{\mathrm{H}} = -\frac{\partial\Psi_{\mathrm{L}}}{\partial x_{\mathrm{L}}} = -\frac{x_{\mathrm{L}}}{\sqrt{x_{\mathrm{L}}^2 + y_{\mathrm{L}}^2}} \sin\left(\arctan\frac{y_{\mathrm{L}}}{x_{\mathrm{L}}}\right) + \frac{y_{\mathrm{L}}}{\sqrt{x_{\mathrm{L}}^2 + y_{\mathrm{L}}^2}} \cos\left(\arctan\frac{y_{\mathrm{L}}}{x_{\mathrm{L}}}\right) + \frac{\Lambda}{2\pi}\frac{y_{\mathrm{L}}^2}{x_{\mathrm{L}}^2 + y_{\mathrm{L}}^2}. \tag{2.14}$$

Once we have obtained u_{H} the coordinates are changed from (x_{L}-y_{L}) to (x_{HL}-y_{HL}) which are the coordinates at the stagnation point.

$$y_{\mathrm{L}} = x_{\mathrm{HL}}, \tag{2.15a}$$

$$x_{\mathrm{L}} = -y_{\mathrm{HL}} - \frac{\Lambda}{2\pi}, \tag{2.15b}$$

$$u_{\mathrm{H}} = -\frac{\partial\Psi_{\mathrm{L}}}{\partial x_{\mathrm{L}}} = +\frac{y_{\mathrm{HL}} + \frac{\Lambda}{2\pi}}{\sqrt{\left(y_{\mathrm{HL}} + \frac{\Lambda}{2\pi}\right)^2 + x_{\mathrm{HL}}^2}} \sin\left(\arctan\frac{x_{\mathrm{HL}}}{\left(y_{\mathrm{HL}} + \frac{\Lambda}{2\pi}\right)}\right) + + \frac{x_{\mathrm{HL}}}{\sqrt{\left(y_{\mathrm{HL}} + \frac{\Lambda}{2\pi}\right)^2 + x_{\mathrm{HL}}^2}} \cos\left(\arctan\frac{x_{\mathrm{HL}}}{\left(y_{\mathrm{HL}} + \frac{\Lambda}{2\pi}\right)}\right) + \frac{\Lambda}{2\pi}\frac{x_{\mathrm{HL}}^2}{\left(y_{\mathrm{HL}} + \frac{\Lambda}{2\pi}\right)^2 + x_{\mathrm{HL}}^2}. \tag{2.15c}$$

Now $y_{\mathrm{HL}} = 0$ and the limit of $x_{\mathrm{HL}} \to 0$ is calculated to obtain

$$u_{\mathrm{H}} = \frac{2\pi}{\Lambda} x_{\mathrm{HL}}. \tag{2.16}$$

From (2.16) it is clear that $\alpha = (2\pi)/\Lambda$. α depends on Λ which is the source, but in a real body it has to depend on L^*, the characteristic length of the body. To find out the value of Λ, it is necessary to write equation (2.10) with dimensions

$$\Psi^* = U^*_\infty r^* \sin\theta + \frac{\Lambda^*\theta}{2\pi} - \frac{\Lambda^*}{2}. \tag{2.17}$$

(2.9) is substituted into (2.17) and in order to find how Λ^* is related to L^* the limit of $x^* \to \infty$ and $y^* = L^*/2$ is evaluated and the result is $\Lambda^* = U^*_\infty L^*$.

Asymptotic behavior of the mean velocity at the stagnation point in optimal coordinates

In this section the outer mean velocity at the stagnation point is found as function of the optimal coordinates Φ_{L}-Ψ_{L}. The asymptotic behavior of the inner mean flow near the stagnation point in optimal coordinates along the body (streamline equal to zero) has been found by Goldstein (1984) as a function of a constant C which depends on the shape of the body. It is

$$|\mathbf{V}_{\mathrm{H}}|^2 = C\Phi_{\mathrm{L}},$$

where $\mathbf{V}_{\mathrm{H}}$ is the velocity vector at the stagnation point. The mean velocity follows the streamlines, thus only the $\Phi-$component has to be considered and it is equal to the absolute value of the mean flow. In the neighbourhood of the stagnation point the Φ-component is actually the x_{HL}-component (see Figure 2.1). Thus it can be stated

$$u_{\mathrm{H}} = \sqrt{C}\Phi_{\mathrm{L}}^{1/2}.$$

In the previous section the Hiemenz solution at the stagnation point in Cartesian coordinates has been found to be

$$u_{\mathrm{H}} = \frac{2\pi}{\Lambda} x_{\mathrm{L}}.$$

The relationship which links the potential to the streamwise coordinate at the stagnation point is

$$\Phi_{\mathrm{L}} = \frac{2\pi}{\Lambda}\frac{x_{\mathrm{L}}^2}{2}.$$

The above relationship can be inverted to evaluate x_{L} as function of Φ_{L}

$$x_{\mathrm{L}} = \sqrt{\frac{\Lambda}{2\pi}}\Phi_{\mathrm{L}}^{1/2}.$$

The constant C is found

$$u_{\mathrm{H}} = \frac{2\pi}{\Lambda}x_{\mathrm{L}} = \frac{2\pi}{\Lambda}\sqrt{\frac{\Lambda}{\pi}}\Phi_{\mathrm{L}}^{1/2} \rightarrow \sqrt{C} = \sqrt{\frac{4\pi}{\Lambda}}.$$

Thus the outer mean flow near the stagnation point can be expressed in optimal coordinates as

$$\widetilde{U}_{\mathrm{b}} = \sqrt{\frac{4\pi}{\Lambda}\Phi_{\mathrm{L}}}. \tag{2.18}$$

To our knowledge, nobody else has found the constant C related with the shape of the body. The outer mean velocity is evaluated numerically in optimal coordinates by inverting equation (2.12) using the Newton-Raphson algorithm. Figure 2.4 (left) shows that in the neighbourhood of the stagnation point the asymptotic solution (2.18) and the mean velocity overlap. Figure 2.4 (right) shows the outer mean velocity on the body surface $\widetilde{U}_b$ as a function of the coordinate s, which is the coordinate along the body (where $\Psi_{\mathrm{L}} = 0$), defined as

$$s = \int_0^{x_{\mathrm{L}}} \sqrt{1 + \frac{\mathrm{d}y_{\mathrm{L}}}{\mathrm{d}x_{\mathrm{L}}}}\mathrm{d}x_{\mathrm{L}}.$$

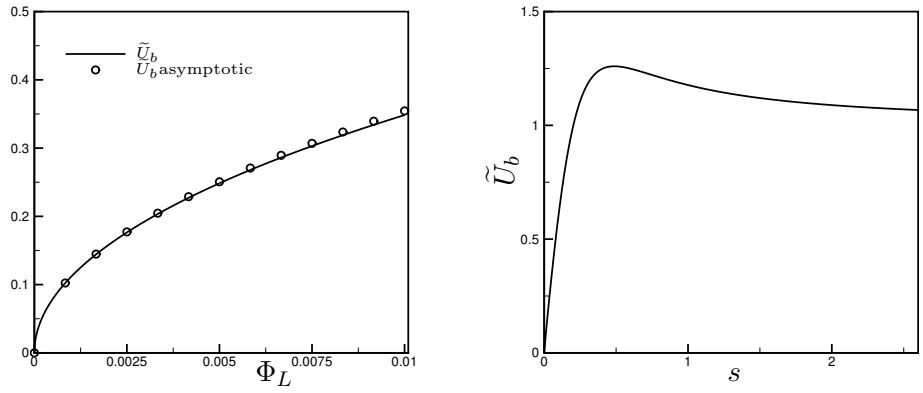

Fig. 2.4: Comparison between the asymptotic solution (2.18) and the outer mean velocity evaluated numerically by inverting equation (2.12) near the stagnation point (left). Outer mean velocity obtained numerically by inverting (2.12) alogside the body's surface as a function of s (right)

2.3.2 Inner mean flow

In this section the equations for the inner mean flow are presented. The boundary layer equations in optimal coordinates are found by considering the limit $R_{\mathrm{L}} \gg 1$. In appendix B the equations are derived and they are

$$\frac{\partial U}{\partial \Phi_{\mathrm{L}}} + \frac{\partial V}{\partial \Psi_{\mathrm{L}}} = 0. \tag{2.19}$$

$$U\frac{\partial U}{\partial \Phi_{\mathrm{L}}} + V\frac{\partial U}{\partial \Psi_{\mathrm{L}}} + \frac{1}{\widetilde{U}_b}\frac{\partial \widetilde{U}_b}{\partial \Phi_{\mathrm{L}}}U^2 = -\frac{1}{\widetilde{U}_b^2}\frac{\partial P}{\partial \Phi_{\mathrm{L}}} + \frac{1}{R_{\mathrm{L}}}\frac{\partial^2 U}{\partial \Psi_{\mathrm{L}}^2}, \tag{2.20}$$

$$\frac{\partial P}{\partial \Psi_{\mathrm{L}}} = 0. \tag{2.21}$$

Here U and V are the velocity components of the inner mean flow and P is the inner mean pressure.

Since the inner mean flow is two dimensional, a streamfunction can be defined

$$\widetilde{\Psi} = F(\Phi_{\mathrm{L}}, \eta)\sqrt{\frac{2\Phi_{\mathrm{L}}}{R_{\mathrm{L}}}}, \tag{2.22}$$

where η is the inner variable

$$\eta = \Psi_{\mathrm{L}} \sqrt{\frac{R_{\mathrm{L}}}{2\Phi_{\mathrm{L}}}}. \tag{2.23}$$

By definition the velocity components are

$$U = \frac{\partial \widetilde{\Psi}}{\partial \Psi_{\mathrm{L}}} = F', \tag{2.24a}$$

$$V = -\frac{\partial \widetilde{\Psi}}{\partial \Phi_{\mathrm{L}}} = -\left[\sqrt{\frac{2\Phi_{\mathrm{L}}}{R_{\mathrm{L}}}} \left(F_{\Phi_{\mathrm{L}}} - F' \frac{\eta}{2\Phi_{\mathrm{L}}} \right) + \frac{F}{2} \sqrt{\frac{2}{R_{\mathrm{L}} \Phi_{\mathrm{L}}}} \right]. \tag{2.24b}$$

By substituting (2.24) in (2.20) and using the Bernoulli equation in optimal coordinates

$$\frac{\mathrm{d}P}{\mathrm{d}\Phi_{\mathrm{L}}} = -\widetilde{U}_b \frac{\mathrm{d}\widetilde{U}_b}{\mathrm{d}\Phi_{\mathrm{L}}},$$

the following is obtained

$$F''' + FF'' + 2m(\Phi_{\mathrm{L}})(1 - F'^2) = 2\Phi_{\mathrm{L}}(F' F'_{\Phi_{\mathrm{L}}} - F_{\Phi_{\mathrm{L}}} F''), \tag{2.25}$$

where

$$F' = \frac{\partial F}{\partial \eta}, \qquad F_{\Phi_{\mathrm{L}}} = \frac{\partial F}{\partial \Phi_{\mathrm{L}}}, \qquad m = \frac{\Phi_{\mathrm{L}}}{\widetilde{U}_b} \frac{\mathrm{d}\widetilde{U}_b}{\mathrm{d}\Phi_{\mathrm{L}}}.$$

Equation (2.25) is the transformed momentum equation in optimal coordinates obtained by using the popular Falker-Skan transformation namely the definition of the similarity variable η. In appendix B the derivation of (2.25) is shown. The velocity components satisfy the following boundary conditions

$$U(\Phi_{\mathrm{L}}, 0) = 0, \qquad V(\Phi_{\mathrm{L}}, 0) = 0, \qquad U(\Phi_{\mathrm{L}}, \infty) = 1. \tag{2.26}$$

The first two are the no-slip condition at the wall for the two velocity components and the last one is the outer boundary condition far from the wall. The latter condition states that the velocity must be equal to the outer velocity $\widetilde{U}_b^*$ because

the inner mean velocity is scaled by it. The boundary conditions for equation (2.25) are then

$$F(\Phi_{\mathrm{L}},0)=0, \qquad F'(\Phi_{\mathrm{L}},0)=0, \qquad F'(\Phi_{\mathrm{L}},\infty)=1. \tag{2.27}$$

Equation (2.25) is the most general steady mean flow equation in optimal coordinates, the flow depends on Φ_{L} therefore it is not similar and an initial condition is needed. The integration starts at the stagnation point where the outer mean flow is given in (2.18) and it is written again here for convenience

$$\widetilde{U}_b=\sqrt{\frac{4\pi}{\Lambda}\Phi_{\mathrm{L}}}.$$

In this particular case the coefficient $m=\frac{\Phi_{\mathrm{L}}}{\widetilde{U}_b}\frac{\mathrm{d}\widetilde{U}_b}{\mathrm{d}\Phi_{\mathrm{L}}}$ in equation (2.25) is $m=1/2$. The equation reduces to a simpler equation with similarity because the function F does not depend on Φ_{L}

$$F'''+FF''-F'^2+1=0, \tag{2.28}$$

with the boundary conditions

$$F(0)=0, \qquad F'(0)=0, \qquad F'(\infty)=1, \tag{2.29}$$

Equation (2.28) is the well known Hiemenz equation which is solved numerically in order to find the inner mean flow close to the stagnation point.

Composite mean flow

In this section the total mean flow is derived by the composite solution. It is given by adding the inner mean flow to the outer mean flow and by subtracting the common part. The last one is $\widetilde{U}_{\mathrm{b}}$, given by the limit of the inner mean velocity for large η and the limit of the outer velocity for small Ψ. The composite solution with dimensions is

$$\widetilde{U}^*_{\mathrm{TOT}} = F'^* + \widetilde{U}^* - \widetilde{U}^*_b. \tag{2.30}$$

By scaling by $\widetilde{U}^*_b = \widetilde{U}_b U^*_\infty$ the following is obtained

$$\widetilde{U}_{\mathrm{TOT}} = F' + \frac{\widetilde{U}^*}{\widetilde{U}^*_b} - 1, \tag{2.31}$$

and dividing and multiplying the second term by U^*_∞ the dimensionless total mean flow is given by

$$\widetilde{U}_{\mathrm{TOT}} = F' + \frac{\widetilde{U}}{\widetilde{U}_b} - 1. \tag{2.32}$$

The composite solution for the wall normal velocity component can be obtained in a similar way. As far as we know this is the first time that the composite solution for a Rankine body has been found.

2.4 Perturbation flow

2.4.1 Outer perturbation flow

In this section the equations for the outer perturbation flow are derived and solved. Goldstein (1984) analyzed the outer perturbation flow over a Rankine body by employing the method illustrated in Appendix E, which involves solving the Eikonal equation, a nonlinear partial differential equation. A few numerical procedures to solve the Eikonal equation are presented in Appendix E. None of these procedures worked, therefore we decided to find the solution of the outer perturbation flow in a different way.

The solution for the perturbation flow in the outer region is of the form suggested by Goldstein (1984), where the flow is given by the mean flow and a three-dimensional, unsteady, periodic in the spanwise direction and time, small amplitude perturbation flow

$$(\mathbf{w}, p) = (1, 0, 0, \widetilde{P}) + \epsilon \left[(\hat{w}_{\Phi \mathrm{H}}, \hat{w}_{\Psi \mathrm{H}}, \hat{w}_{z\mathrm{H}}) e^{ik_z z - i\bar{t}} + \nabla\varphi, p \right], \tag{2.33}$$

with $\epsilon \ll 1$. The velocities are scaled by the absolute value of the local outer mean displaced velocity $\widetilde{U}_d^*$. This is obtained by the displaced potential and stream-function which are derived in Appendix C. The decomposition (2.33) shows that the outer mean flow $\widetilde{U}_d$ is uniform, because it is scaled by itself. We need to do this because in the Navier-Stokes equations (2.5)-(2.8) the velocity components are scaled by the local mean velocity. The three velocity components of the perturbation flow are along the optimal coordinates, namely parallel and orthogonal to the streamlines and in the spanwise direction. The outer perturbation potential is also scaled by $\widetilde{U}_d^*$ while the pressure is scaled by U_∞^*.

$\nabla\varphi$ is the part of the perturbation velocity related with the pressure fluctuations and $\mathbf{w}_{\mathrm{H}}$ is the effect of the imposed upstream vorticity field. This is called Helmholtz decomposition and Ladyzhenskaya & Silverman (1969) provided the existence and uniqueness of this solution for Navier-Stokes equations. The latter part of the perturbation velocity is necessary because the upstream boundary condition would not be satisfied by the potential part only, since upstream the pressure fluctuations are zero thus the potential is zero and it cannot match the imposed upstream perturbation velocity. The velocity $\mathbf{w}_{\mathrm{H}}$ has then to satisfy the homogeneous equation (without pressure term). In the case of a flat plate, $\mathbf{w}_{\mathrm{H}}$ coincides with $\mathbf{u}_\infty$ (initial gust) because there is no distortion due to the curvature. This can be seen mathematically in the equations for $\mathbf{w}_{\mathrm{H}}$ derived in Goldstein (1978) in Cartesian coordinates.

$$\frac{\partial \mathbf{w}_{\mathrm{H}}}{\partial t_{\mathrm{L}}} + \widetilde{\mathbf{U}} \cdot \nabla \mathbf{w}_{\mathrm{H}} + \mathbf{w}_{\mathrm{H}} \cdot \nabla \widetilde{\mathbf{U}} = \frac{1}{R_{\mathrm{L}}} \nabla \cdot (\nabla \mathbf{w}_{\mathrm{H}}). \tag{2.34}$$

The above equation contains the mean flow $\widetilde{\mathbf{U}}$ which for a flat plate is uniform, thus $\tilde{\mathbf{u}}_{\mathrm{H}}$ for a flat plate can only be equal to the initial gust, used as upstream

boundary condition. This is the case studied in Leib *et al.* (1999) where the solution in region I is given by equation (3.1) in their paper. The velocity must satisfy the continuity equation which in their case becomes the Laplace's equation (3.3) in Leib *et al.* (1999) for the perturbation potential. For the case studied herein the mean flow has a spatial variation and $\mathbf{w}_{\mathrm{H}}$ is affected by this variation which physically means that there is a distortion in the perturbation velocity field.

Reduced momentum equations in optimal coordinates

By substituting the decomposition (2.33) into the Navier-Stokes equations in optimal coordinates and collecting terms of order ϵ, the equations for the homogeneous velocity are obtained.

Φ-momentum:

$$-\frac{i}{\widetilde{U}_d^2}\hat{w}_{\Phi\mathrm{H}}+\frac{\partial\hat{w}_{\Phi\mathrm{H}}}{\partial\bar{\Phi}_d}+\frac{2}{\widetilde{U}_d}\frac{\partial\widetilde{U}_d}{\partial\bar{\Phi}_d}\hat{w}_{\Phi\mathrm{H}}=\frac{1}{Rk_\Phi}\left(\frac{\partial^2\hat{w}_{\Phi\mathrm{H}}}{\partial\Psi_d^2}-\frac{k_z^2}{\widetilde{U}_d^2}\hat{w}_{\Phi\mathrm{H}}\right), \tag{2.35}$$

Ψ-momentum:

$$-\frac{i}{\widetilde{U}_d^2}\hat{w}_{\Psi\mathrm{H}}+\frac{\partial\hat{w}_{\Psi\mathrm{H}}}{\partial\bar{\Phi}_d}+\frac{2}{\widetilde{U}_d}\frac{\partial\widetilde{U}_d}{\partial\bar{\Psi}_d}\hat{w}_{\Phi\mathrm{H}}=\frac{1}{Rk_\Phi}\left(\frac{\partial^2\hat{w}_{\Psi\mathrm{H}}}{\partial\Psi_d^2}-\frac{k_z^2}{\widetilde{U}_d^2}\hat{w}_{\Psi\mathrm{H}}\right), \tag{2.36}$$

***z*-momentum:**

$$-\frac{i}{\widetilde{U}_d^2}\hat{w}_{z\mathrm{H}}+\frac{\partial\hat{w}_{z\mathrm{H}}}{\partial\bar{\Phi}_d}+\frac{1}{\widetilde{U}_d}\frac{\partial\widetilde{U}_d}{\partial\bar{\Phi}_d}\hat{w}_{z\mathrm{H}}=\frac{1}{Rk_\Phi}\left(\frac{\partial^2\hat{w}_{z\mathrm{H}}}{\partial\Psi_d^2}-\frac{k_z^2}{\widetilde{U}_d^2}\hat{w}_{z\mathrm{H}}\right). \tag{2.37}$$

The streamwise coordinate $\bar{\Phi}_d$ is scaled by λ_Φ^* for both the mean and the perturbation flow, while the normal coordinate is scaled by λ_Φ^* only for the mean flow, while it is scaled by λ_z^* for the perturbation flow. Therefore, the coordinates used for the perturbation velocity are $\bar{\Phi}_d-\Psi_d$ while the ones used for the mean

flow are $\bar{\Phi}_d - \bar{\Psi}_d$ where $\bar{\Psi}_d = k_\Phi \Psi_d$. This choice follows the hypothesis that the streamwise wavelength λ^*_Φ is of the same order of the characteristic length of the body L^*. The perturbation flow evolves on different scales in the two directions, while the mean flow evolves on scales of order L^* in both the directions, therefore its derivative with respect to the normal coordinate Ψ is of order k_Φ because

$$\frac{\partial \widetilde{U}}{\partial \Psi_d} = \frac{\partial \widetilde{U}}{\partial \bar{\Psi}_d}\frac{\partial \bar{\Psi}_d}{\partial \Psi_d} = \mathcal{O}(1)\cdot k_\Phi.$$

Equation for outer perturbation potential

The outer perturbation potential is found by substituting the decomposition (2.33) into the continuity equation

$$\nabla^2 \varphi^\infty = -\nabla \cdot \mathbf{w}^\infty_{\mathrm{H}}, \tag{2.38}$$

where φ^∞ and $\mathbf{w}^\infty_{\mathrm{H}}$ are scaled by U^*_∞. Then $\hat{\varphi}^\infty$ is introduced

$$\varphi^\infty = \hat{\varphi}^\infty(\Phi_d, \Psi_d) e^{ik_z z - i\bar{t}},$$

and it is substituted into (2.38). The equation in optimal coordinates is

$$\frac{\partial^2 \hat{\varphi}^\infty}{\partial \Phi_d^2} + \frac{\partial^2 \hat{\varphi}^\infty}{\partial \Psi_d^2} - \frac{k_z^2 \hat{\varphi}^\infty}{\widetilde{U}_d^2} = -\left[\frac{\partial \hat{w}_{\Phi\mathrm{H}}}{\partial \Phi_d} + \frac{\partial \hat{w}_{\Psi\mathrm{H}}}{\partial \Psi_d} + ik_z \frac{\hat{w}_{z\mathrm{H}}}{\widetilde{U}_d}\right].$$

By rescaling the streamwise coordinate by λ_Φ the terms of order k_Φ can be neglected. The scale for the potential is changed as $\hat{\varphi}^\infty = \hat{\varphi}\widetilde{U}_d$, where φ is scaled by $\widetilde{U}^*_d$. It is worth remembering that the outer mean flow $\widetilde{U}_d$ can be taken out of the derivative with respect to Ψ_d because its derivative with respect to this variable is of order k_Φ. The following is obtained

$$\widetilde{U}_d \frac{\partial^2 \hat{\varphi}}{\partial \Psi_d^2} - \frac{k_z^2}{\widetilde{U}_d}\hat{\varphi} = -\frac{\partial \hat{w}_{\Psi\mathrm{H}}}{\partial \Psi_d} - \frac{ik_z}{\widetilde{U}_d}\hat{w}_{z\mathrm{H}}. \tag{2.39}$$

The total outer perturbation velocity in optimal coordinates is then given by

$$\mathbf{w} = \mathbf{w}_{\mathrm{H}} + \left[\widetilde{U}_d k_\Phi \frac{\partial \hat{\varphi}}{\partial \bar{\Phi}_d}, \widetilde{U}_d \frac{\partial \hat{\varphi}}{\partial \Psi_d}, i k_z \hat{\varphi}\right]. \tag{2.40}$$

The total velocity satisfies the continuity equation in optimal coordinates (2.5). In fact, the first term of (2.5) can be neglected because the scale of Φ_d is changed and it is multiplied by k_Φ. The remaining terms give

$$\frac{\partial \hat{w}_{\Psi\mathrm{H}}}{\partial \Psi_d} + \widetilde{U}_d \frac{\partial^2 \hat{\varphi}}{\partial \Psi_d^2} + \frac{i k_z}{\widetilde{U}_d} \hat{w}_{z\mathrm{H}} \widetilde{U}_d - \frac{k_z^2}{\widetilde{U}_d} \hat{\varphi} = 0,$$

which is satisfied by construction because the potential is found by (2.39).

Equation for outer perturbation pressure

The equation for the outer perturbation pressure has been found by Goldstein (1978) and is given by

$$p = -\frac{\partial \varphi^\infty}{\partial t} - \widetilde{U}_d \cdot \nabla \varphi^\infty + \frac{1}{R} \nabla^2 \varphi^\infty,$$

where φ^∞ is the potential scaled by U_∞^*. The equation for the pressure is

$$p = -\frac{\partial \varphi^\infty}{\partial t} - \widetilde{U}_d \frac{\partial \varphi^\infty}{\partial \Phi_d} + \frac{1}{R}\left(\widetilde{U}_d^2 \frac{\partial^2 \varphi^\infty}{\partial \Phi_d^2} + \widetilde{U}_d^2 \frac{\partial^2 \varphi^\infty}{\partial \Psi_d^2} + \frac{\partial^2 \varphi^\infty}{\partial z^2}\right).$$

The pressure is written as

$$p = \hat{p}(\Phi_d, \Psi_d) e^{i k_z z - i\bar{t}}.$$

The potential is scaled by $\widetilde{U}_d$ and the coordinate Φ_d is scaled by λ_Φ^* to obtain

$$\hat{p} = k_\Phi \left(i \widetilde{U}_d \hat{\varphi} - \widetilde{U}_d^3 \frac{\partial \hat{\varphi}}{\partial \bar{\Phi}_d} - \hat{\varphi} \widetilde{U}_d^2 \frac{\partial \widetilde{U}_d}{\partial \bar{\Phi}_d} + \frac{\widetilde{U}_d^3}{R k_\Phi} \frac{\partial^2 \hat{\varphi}}{\partial \Psi_d^2} - \widetilde{U}_d \frac{k_z^2}{R k_\Phi} \hat{\varphi}\right). \tag{2.41}$$

The pressure can be written as k_Φ which multiplies a quantity of order 1.

$$\hat{p} = k_\Phi \hat{\hat{p}},$$

where

$$\hat{\tilde{p}} = i\widetilde{U}_d\hat{\varphi} - \widetilde{U}_d^3\frac{\partial\hat{\varphi}}{\partial\bar{\Phi}_d} - \hat{\varphi}\widetilde{U}_d^2\frac{\partial\widetilde{U}_d}{\partial\bar{\Phi}_d} + \frac{\widetilde{U}_d^3}{Rk_\Phi}\frac{\partial^2\hat{\varphi}}{\partial\Psi_d^2} - \widetilde{U}_d\frac{k_z^2}{Rk_\Phi}\hat{\varphi}.$$

Outer perturbation flow solution

In this section the solution for the outer perturbation velocity and potential is found. We start from the z-momentum equation because it only contains $w_{z\mathrm{H}}$. The z-momentum equation is written as

$$\left(-\frac{i}{\widetilde{U}_d^2} + \frac{1}{\widetilde{U}_d}\frac{\partial\widetilde{U}_d}{\partial\bar{\Phi}_d} + \frac{\kappa^2}{\widetilde{U}_d^2}\right)\hat{w}_{z\mathrm{H}} + \frac{\partial\hat{w}_{z\mathrm{H}}}{\partial\bar{\Phi}_d} - \frac{1}{Rk_\Phi}\frac{\partial^2\hat{w}_{z\mathrm{H}}}{\partial\Psi_d^2} = 0,$$

with $\kappa = k_z/\sqrt{Rk_\Phi}$. The function f_z is introduced

$$f_z(\bar{\Phi},\bar{\Psi}) = -\frac{i}{\widetilde{U}_d^2} + \frac{1}{\widetilde{U}_d}\frac{\partial\widetilde{U}_d}{\partial\bar{\Phi}_d} + \frac{\kappa^2}{\widetilde{U}_d^2},$$

and the solution is assumed of the following form in order to simplify the z-momentum equation.

$$\hat{w}_{z\mathrm{H}} = \hat{\hat{w}}_{z\mathrm{H}}(\bar{\Phi},\Psi)\exp\left(-\int_{\bar{\Phi}_{d0}}^{\bar{\Phi}_d} f_z\mathrm{d}\bar{\Phi}_d\right), \tag{2.42}$$

where $\bar{\Phi}_{d0}$ is the position of the grid upstream. Equation (2.42) is substituted into the z-momentum equation and terms of order k_Φ resulting from the derivatives of the mean flow with respect to Ψ_d can be neglected. Leib *et al.* (1999) do a similar thing from equation (5.9) to (5.10) of their work, they also exclude terms of order k_1, which is the dimensionless streamwise wavenumber in Leib *et al.* (1999), by putting them on the right hand side of the equation.

The following equation for $\hat{\hat{w}}_{z\mathrm{H}}$ is obtained

$$\frac{\partial\hat{\hat{w}}_{z\mathrm{H}}}{\partial\bar{\Phi}} - \frac{1}{Rk_\Phi}\frac{\partial^2\hat{\hat{w}}_{z\mathrm{H}}}{\partial\Psi^2} = \mathcal{O}(k_\Phi).$$

As in Leib *et al.* (1999) the matching upstream suggests to take the solution of the form

$$\hat{\tilde{w}}_{z\mathrm{H}} = \tilde{w}_{z\mathrm{H}}(\bar{\Phi})e^{ik_\Psi \Psi_d}.$$

The solution for $\tilde{w}_{z\mathrm{H}}$ can easily be found by substituting the above equation into the equation for $\hat{\tilde{w}}_{z\mathrm{H}}$ obtaining

$$\tilde{w}_{z\mathrm{H}} = Ce^{-\kappa_2^2 \bar{\Phi}},$$

where $\kappa_2 = k_\Psi/\sqrt{Rk_\Phi}$ and the constant C is found by matching upstream with the initial gust. The solution for the homogeneous spanwise velocity component is

$$\hat{w}_{z\mathrm{H}} = \hat{u}_z^\infty \exp\left[-\kappa_2^2(\bar{\Phi}_d - \bar{\Phi}_{d0}) + ik_\Psi \Psi_d - \int_{\bar{\Phi}_{d0}}^{\bar{\Phi}_d} \left(-\frac{i}{\widetilde{U}_d^2} + \frac{1}{\widetilde{U}_d}\frac{\partial \widetilde{U}_d}{\partial \bar{\Phi}_d} + \frac{\kappa^2}{\widetilde{U}_d^2}\right) \mathrm{d}\bar{\Phi}_d\right]. \tag{2.43}$$

The integral in the solution contains the outer mean flow and it is evaluated from upstream for every streamline. Along the streamlines very close to the body, the mean velocity becomes very small approaching the stagnation point. Therefore we need to be in a region sufficiently away from the stagnation point to be able to evaluate the integral. Solution (2.43) is only valid when $\widetilde{U}_d$ and its derivatives are of order 1. It can be observed that if $\widetilde{U}_d$ were uniform, equation (5.11) in Leib *et al.* (1999) would be obtained. Therefore solution (2.43) is an extension to solution (5.11) in Leib *et al.* (1999). The curvature affects the viscous decay.

It is easy to demonstrate that the solution (2.43) satisfies equation (2.37), by taking the derivatives of $\hat{w}_{z\mathrm{H}}$, which are

$$\frac{\partial \hat{w}_{z\mathrm{H}}}{\partial \bar{\Phi}_d} = -\kappa_2^2 \hat{w}_{z\mathrm{H}} - f_z \hat{w}_{z\mathrm{H}},$$

$$\frac{\partial^2 \hat{w}_{z\mathrm{H}}}{\partial \Psi_d^2} = -k_\Psi^2 \hat{w}_{z\mathrm{H}},$$

and substituting into (2.43) the following is obtained

$$-\frac{i}{\widetilde{U}_d^2} - \kappa_2^2 - f_z + \frac{1}{\widetilde{U}_d}\frac{\partial \widetilde{U}_d}{\partial \bar{\Phi}_d} = \frac{1}{Rk_\Phi}\left(-k_\Psi^2 - \frac{1}{\widetilde{U}_d^2}k_z^2\right).$$

Considering that

- $f_z = -\frac{i}{\widetilde{U}_d^2} + \frac{1}{\widetilde{U}_d}\frac{\partial \widetilde{U}_d}{\partial \bar{\Phi}_d} + \frac{\kappa^2}{\widetilde{U}_d^2}$
- $\kappa = k_z/\sqrt{Rk_\Phi}$
- $\kappa_2 = k_\Psi/\sqrt{Rk_\Phi}$

the equation simplifies and the check is complete.

The solution for the Φ-momentum equation (2.35) is obtained in a similar way by introducing the function f_Φ

$$f_\Phi(\bar{\Phi}, \bar{\Psi}) = -\frac{i}{\widetilde{U}_d^2} + \frac{2}{\widetilde{U}_d}\frac{\partial \widetilde{U}_d}{\partial \bar{\Phi}_d} + \frac{\kappa^2}{\widetilde{U}_d^2}.$$

The only difference with f_z is that the term $\frac{1}{\widetilde{U}_d}\frac{\partial \widetilde{U}_d}{\partial \bar{\Phi}_d}$ is multiplied by 2.

The solution for the homogeneous streamwise velocity is

$$\hat{w}_{\Phi\mathrm{H}} = \hat{u}_\Phi^\infty \exp\left[-\kappa_2^2(\bar{\Phi}_d - \bar{\Phi}_{d0}) + ik_\Psi \Psi_d - \int_{\bar{\Phi}_{d0}}^{\bar{\Phi}_d}\left(-\frac{i}{\widetilde{U}_d^2} + \frac{2}{\widetilde{U}_d}\frac{\partial \widetilde{U}_d}{\partial \bar{\Phi}_d} + \frac{\kappa^2}{\widetilde{U}_d^2}\right) d\bar{\Phi}_d\right]. \tag{2.44}$$

Even in this case, if $\widetilde{U}_d$ were uniform, namely upstream or for a flat plate, equation (5.11) in Leib *et al.* (1999) would be obtained and it is easy to demonstrate that the solution (2.44) satisfies equation (2.35).

The Ψ-momentum equation is written as

$$\left(-\frac{i}{\widetilde{U}_d^2}+\frac{\kappa^2}{\widetilde{U}_d^2}\right)\hat{w}_{\Psi\mathrm{H}}+\frac{\partial\hat{w}_{\Psi\mathrm{H}}}{\partial\bar{\Phi}_d}-\frac{1}{Rk_\Phi}\frac{\partial^2\hat{w}_{\Psi\mathrm{H}}}{\partial\Psi_d^2}=-\frac{2}{\widetilde{U}_d}\frac{\partial\widetilde{U}_d}{\partial\bar{\Psi}_d}\hat{w}_{\Phi\mathrm{H}},$$

and the function f_Ψ is introduced

$$f_\Psi(\bar{\Phi},\bar{\Psi})=-\frac{i}{\widetilde{U}_d^2}+\frac{\kappa^2}{\widetilde{U}_d^2}.$$

The solution is assumed of the following form in order to simplify the Ψ-momentum equation.

$$\hat{w}_{\Psi\mathrm{H}}=\hat{\hat{w}}_{\Psi\mathrm{H}}(\bar{\Phi},\Psi)\exp\left(-\int_{\bar{\Phi}_{d0}}^{\bar{\Phi}_d}f_\Psi\mathrm{d}\bar{\Phi}_d\right). \tag{2.45}$$

(2.45) is substituted into the Ψ-momentum equation and terms of order k_Φ resulting from the derivatives of the mean flow with respect to Ψ_d can be neglected.

The following equation for $\hat{\hat{w}}_{\Psi\mathrm{H}}$ is obtained

$$\frac{\partial\hat{\hat{w}}_{\Psi\mathrm{H}}}{\partial\bar{\Phi}}-\frac{1}{Rk_\Phi}\frac{\partial^2\hat{\hat{w}}_{\Psi\mathrm{H}}}{\partial\Psi^2}=-\frac{2}{\widetilde{U}_d}\frac{\partial\widetilde{U}_d}{\partial\bar{\Psi}_d}\hat{w}_{\Phi\mathrm{H}}\exp\left(+\int_{\bar{\Phi}_{d0}}^{\bar{\Phi}_d}f_\Psi\mathrm{d}\bar{\Phi}_d\right)+\mathcal{O}(k_\Phi). \tag{2.46}$$

The solution to equation (2.46) can be obtained in two different ways.

- Using solution $1.1.2-1$ in Polyanin (2001) on page 51.
- Reducing equation (2.46) to a ordinary differential equation by assuming the solution of the form

  $$\hat{\hat{w}}_{\Psi\mathrm{H}}=\tilde{w}_{\Psi\mathrm{H}}(\bar{\Phi})e^{ik_\Psi\Psi},$$

  as for the spanwise and streamwise velocity components.

In both cases, the solution for the homogeneous normal velocity is

$$\hat{w}_{\Psi\mathrm{H}} = \exp\left[-\kappa_2^2(\bar{\Phi}_d - \bar{\Phi}_{d0}) + ik_\Psi \Psi_d - \int_{\bar{\Phi}_{d0}}^{\bar{\Phi}_d} \left(-\frac{i}{\widetilde{U}_d^2} + \frac{\kappa^2}{\widetilde{U}_d^2}\mathrm{d}\bar{\Phi}\right)\right] \left(\hat{u}_\Psi^\infty + \int_{\bar{\Phi}_{d0}}^{\bar{\Phi}_d} \mathrm{RHS}(\chi,\tau)e^{\kappa_2^2\tau}\mathrm{d}\tau\right), \tag{2.47}$$

where

$$\mathrm{RHS} = \frac{1}{\exp\left(ik_\Psi \Psi\right)} \left\{-\frac{2}{\widetilde{U}_d}\frac{\partial \widetilde{U}_d}{\partial \bar{\Psi}_d}\hat{w}_{\Phi\mathrm{H}} \exp\left(+\int_{\bar{\Phi}_{d0}}^{\bar{\Phi}_d} f_\Psi \mathrm{d}\bar{\Phi}_d\right)\right\}.$$

Upstream, where $\bar{\Phi}_d = \bar{\Phi}_{d0}$, the initial gust is found. Moreover, if $\widetilde{U}_d$ were uniform, RHS would be zero, therefore equation (5.11) in Leib *et al.* (1999) would be obtained.

Now that the homogeneous outer perturbation velocity is known, it can be used to find the solution of the outer perturbation potential. Equation (2.39) is inhomogeneous therefore we need to find the solution to the associated homogeneous equation and the particular solution. The solution to the associated homogeneous equation is found by employing WKBJ theory (Bender & Orszag, 1999). This solution is of the form

$$\hat{\varphi} = C_1 \exp\left(\int_{\bar{\Psi}_{d0}}^{\bar{\Psi}_d} \frac{k_z}{\widetilde{U}_d}\mathrm{d}\bar{\Psi}_d\right) + C_2 \exp\left(-\int_{\bar{\Psi}_{d0}}^{\bar{\Psi}_d} \frac{k_z}{\widetilde{U}_d}\mathrm{d}\bar{\Psi}_d\right). \tag{2.48}$$

The outer boundary condition for the potential states that it is zero when $\bar{\Psi}_d \to \infty$, therefore C_1 must be zero in order to satisfy this condition. The part of the solution with C_2 decays very quickly because $k_z = 2\pi$ and $\bar{\Psi}$ is of order 1. The solution is then confined within the boundary layer and it is not relevant for the outer region.

The particular solution could be found by the technique of *variation of parameters*, but we are not able to integrate from $\Psi_d = 0$ because the right hand side of equation (2.39) is only valid in the region where $\widetilde{U}_d$ is of order 1.

The solution for the outer perturbation potential is found by defining $\hat{\varphi}(\bar{\Phi}_d)$

$$\hat{\varphi} = \hat{\hat{\varphi}}(\bar{\Phi}_d) e^{ik_\Psi \Psi_d}, \tag{2.49}$$

because the right hand side of (2.39) is of the same form. (2.49) is substituted into equation (2.39) to obtain

$$\widetilde{U}_d k_\Psi^2 \hat{\hat{\varphi}}(\bar{\Phi}_d) + \frac{k_z^2}{\widetilde{U}_d} \hat{\hat{\varphi}}(\bar{\Phi}_d) = H(\bar{\Phi}_d), \tag{2.50}$$

where

$$\begin{aligned} H(\bar{\Phi}_d) =& e^{-\kappa_2^2(\bar{\Phi}_d - \bar{\Phi}_{d0})} \left[ik_\Psi \left(\hat{u}_\Psi^\infty + \int_{\bar{\Phi}_{d0}}^{\bar{\Phi}_d} \mathrm{RHS}(\chi, \tau) e^{\kappa_2^2 \tau} \mathrm{d}\tau \right) \exp\left(- \int_{\bar{\Phi}_{d0}}^{\bar{\Phi}_d} f_\Psi \mathrm{d}\bar{\Phi}_d \right) \right] + \\ & e^{-\kappa_2^2(\bar{\Phi}_d - \bar{\Phi}_{d0})} \left[\frac{ik_z \hat{w}_z^\infty}{\widetilde{U}_d} \exp\left(- \int_{\bar{\Phi}_{d0}}^{\bar{\Phi}_d} f_z \mathrm{d}\bar{\Phi}_d \right) \right]. \end{aligned}$$

Therefore (2.50) can be solved explicitly for $\hat{\varphi}$.

$$\hat{\varphi} = \frac{\widetilde{U}_d H(\bar{\Phi}_d)}{k_\Psi^2 \widetilde{U}_d^2 + k_z^2} e^{ik_\Psi \Psi_d}. \tag{2.51}$$

The total outer perturbation velocity solution in optimal coordinates is

$$\begin{aligned} \hat{w}_\Phi =& \hat{u}_\Phi^\infty \exp\left(-\kappa_2^2(\bar{\Phi}_d - \bar{\Phi}_{d0}) + ik_\Psi \Psi_d - \int_{\bar{\Phi}_{d0}}^{\bar{\Phi}_d} \left(-\frac{i}{\widetilde{U}_d^2} + \frac{2}{\widetilde{U}_d} \frac{\partial \widetilde{U}_d}{\partial \bar{\Phi}_d} + \frac{\kappa^2}{\widetilde{U}_d^2} \right) \mathrm{d}\bar{\Phi}_d \right) + \\ & \mathcal{O}(k_\Phi), \end{aligned} \tag{2.52}$$

$$\hat{w}_\Psi = \exp\left[-\kappa_2^2(\bar{\Phi}_d - \bar{\Phi}_{d0}) + ik_\Psi \Psi_d - \int_{\bar{\Phi}_{d0}}^{\bar{\Phi}_d} \left(-\frac{i}{\widetilde{U}_d^2} + \frac{\kappa^2}{\widetilde{U}_d^2}\mathrm{d}\bar{\Phi}\right)\right]$$
$$\left(\hat{u}_\Psi^\infty + \int_{\bar{\Phi}_{d0}}^{\bar{\Phi}_d} \mathrm{RHS}(\chi,\tau)e^{\kappa_2^2\tau}\mathrm{d}\tau\right) + \tag{2.53}$$
$$\widetilde{U}_d ik_\Psi \frac{\widetilde{U}_d H(\bar{\Phi}_d)}{k_\Psi^2 \widetilde{U}_d^2 + k_z^2} e^{ik_\Psi \Psi_d},$$

$$\hat{w}_z = \hat{u}_z^\infty \exp\left(-\kappa_2^2(\bar{\Phi}_d - \bar{\Phi}_{d0}) + ik_\Psi \Psi_d - \int_{\bar{\Phi}_{d0}}^{\bar{\Phi}_d} \left(-\frac{i}{\widetilde{U}_d^2} + \frac{1}{\widetilde{U}_d}\frac{\partial \widetilde{U}_d}{\partial \bar{\Phi}_d} + \frac{\kappa^2}{\widetilde{U}_d^2}\right)\mathrm{d}\bar{\Phi}_d\right) +$$
$$ik_z \frac{\widetilde{U}_d H(\bar{\Phi}_d)}{k_\Psi^2 \widetilde{U}_d^2 + k_z^2} e^{ik_\Psi \Psi_d}. \tag{2.54}$$

Solutions (2.52)-(2.54) satisfy the outer perturbation equations and the resolution check has been done numerically. Upstream when $\bar{\Phi}_d = \bar{\Phi}_{d0}$ the amplitudes are the same as the initial gust. By moving downstream, the perturbation velocity decays and it is distorted by the outer mean velocity $\widetilde{U}_d$ which varies alongside the body. The pressure is an explicit function of the potential and it is written again here for convenience

$$\hat{p} = k_\Phi \left(i\widetilde{U}_d - \widetilde{U}_d^3 \frac{\partial}{\partial \bar{\Phi}_d} - \widetilde{U}_d^2 \frac{\partial \widetilde{U}_d}{\partial \bar{\Phi}_d} + \frac{\widetilde{U}_d^3}{Rk_\Phi}\frac{\partial^2}{\partial \Psi_d^2} - \widetilde{U}_d \frac{k_z^2}{Rk_\Phi}\right)\hat{\varphi}.$$

2.4.2 Boundary region equations

In this section the equations for the inner perturbation flow, namely the boundary region equations, are derived. The flow inside the boundary layer is decomposed into the total mean flow (composite solution) and a small amplitude perturbation flow

$$(\mathbf{u}, p) = (\widetilde{U}_{\mathrm{TOT}}, \widetilde{V}_{\mathrm{TOT}}, 0, \widetilde{P}_{\mathrm{TOT}}) + \epsilon \left(\frac{ik_z}{k_\Phi}\bar{u}(\bar{\Phi}, \Psi), \frac{ik_z}{k_\Phi}\sqrt{\frac{2\bar{\Phi}k_\Phi}{R}}\bar{v}(\bar{\Phi}, \Psi), \bar{w}(\bar{\Phi}, \Psi), \frac{ik_z}{\sqrt{Rk_\Phi}}\sqrt{\frac{k_\Phi}{R}}\bar{p}(\bar{\Phi}, \Psi) \right) e^{ikz_z - i\bar{t}}, \tag{2.55}$$

with $\epsilon \ll 1$. The coordinates for the analysis in the boundary layer region are the not displaced ones (see appendix C). The composite solution for the mean flow in these coordinates is given by

$$\widetilde{U}_{\mathrm{TOT}} = \widetilde{U}_b(F' - 1) + \widetilde{U}_d,$$

$$V_{\mathrm{TOT}} = \frac{k_\Phi \widetilde{U}_b}{\sqrt{Rk_\Phi}} \left(\frac{\eta F'}{\sqrt{2\bar{\Phi}}} - \sqrt{2\bar{\Phi}}\frac{\partial F}{\partial \bar{\Phi}} - \frac{F}{\sqrt{2\bar{\Phi}}} - \frac{\partial}{\partial \bar{\Phi}}(\beta(\Phi)\sqrt{2\bar{\Phi}}) \right) + k_\Phi \widetilde{V}_d,$$

with $\widetilde{U}_d$ and $\widetilde{V}_d$ the displaced mean flow components along Φ-Ψ coordinates. The composite mean flow must be used because for large-η the perturbation flow matches the outer perturbation flow and the mean flow is the outer mean flow with the displacement effect taken into account. For the flat plate case of Leib *et al.* (1999) the mean flow is only the inner mean flow which coincides with the composite mean flow without displacement. In fact, the mean flow is uniform in their case and therefore the common and outer part are the same and simplify so that only the inner mean flow is left.

The boundary region equations are obtained by substituting the decomposition (2.55) into the Navier-Stokes equations in optimal coordinates (2.5)-(2.8) and terms of order ϵ are collected. The equations are linearised so that terms of order ϵ^2 are neglected in the equations

Continuity:

$$\frac{\partial \bar{u}}{\partial \bar{\Phi}} - \frac{\eta}{2\bar{\Phi}}\frac{\partial \bar{u}}{\partial \eta} + \frac{\partial \bar{v}}{\partial \eta} + \frac{\bar{w}}{\widetilde{U}} = 0, \tag{2.56}$$

Φ-momentum:

$$
\begin{aligned}
&-\frac{i\bar{u}}{\widetilde{U}^2}+\left[\widetilde{U}_b(F'-1)+\widetilde{U}_d\right]\frac{\partial\bar{u}}{\partial\bar{\Phi}}-\frac{\eta}{2\bar{\Phi}}\left[\widetilde{U}_b(F'-1)+\widetilde{U}_d\right]\frac{\partial\bar{u}}{\partial\eta}+\\
&\frac{\partial}{\partial\bar{\Phi}}\left[\widetilde{U}_b(F'-1)+\widetilde{U}_d\right]\bar{u}-\frac{\eta}{2\bar{\Phi}}F''\bar{u}+\\
&\widetilde{U}_b\left(\frac{\eta F'}{\sqrt{2\bar{\Phi}}}-\sqrt{2\bar{\Phi}}\frac{\partial F}{\partial\bar{\Phi}}-\frac{F}{\sqrt{2\bar{\Phi}}}-\frac{\partial}{\partial\bar{\Phi}}(\beta(\Phi)\sqrt{2\bar{\Phi}})\right)\frac{1}{\sqrt{2\bar{\Phi}}}\frac{\partial\bar{u}}{\partial\eta}+\\
&\widetilde{V}_d\sqrt{\frac{k_\Phi R}{2\bar{\Phi}}}\frac{\partial\bar{u}}{\partial\eta}+F''\bar{v}+2\left[\widetilde{U}_b(F'-1)+\widetilde{U}_d\right]\frac{\partial\widetilde{U}}{\partial\bar{\Phi}}\frac{\bar{u}}{\widetilde{U}}=\frac{1}{2\bar{\Phi}}\frac{\partial^2\bar{u}}{\partial\eta^2}-\frac{\kappa^2}{\widetilde{U}^2}\bar{u},
\end{aligned}
\tag{2.57}
$$

Ψ-momentum:

$$
\begin{aligned}
&-\frac{i\bar{v}}{\widetilde{U}^2}+\left[\widetilde{U}_b(F'-1)+\widetilde{U}_d\right]\frac{\bar{v}}{2\bar{\Phi}}+\left[\widetilde{U}_b(F'-1)+\widetilde{U}_d\right]\frac{\partial\bar{v}}{\partial\bar{\Phi}}-\\
&\frac{\eta}{2\bar{\Phi}}\left[\widetilde{U}_b(F'-1)+\widetilde{U}_d\right]\frac{\partial\bar{v}}{\partial\eta}+\\
&\sqrt{\frac{Rk_\Phi}{2\bar{\Phi}}}\frac{\partial}{\partial\bar{\Phi}}\left[\frac{\widetilde{U}_b}{\sqrt{Rk_\Phi}}\left(\frac{\eta F'}{\sqrt{2\bar{\Phi}}}-\sqrt{2\bar{\Phi}}\frac{\partial F}{\partial\bar{\Phi}}-\frac{F}{\sqrt{2\bar{\Phi}}}-\frac{\partial}{\partial\bar{\Phi}}(\beta(\Phi)\sqrt{2\bar{\Phi}})\right)+\widetilde{V}_d\right]\bar{u}-\\
&\frac{\eta}{2\bar{\Phi}}\sqrt{\frac{Rk_\Phi}{2\bar{\Phi}}}\frac{\partial}{\partial\eta}\left[\frac{\widetilde{U}_b}{\sqrt{Rk_\Phi}}\left(\frac{\eta F'}{\sqrt{2\bar{\Phi}}}-\sqrt{2\bar{\Phi}}\frac{\partial F}{\partial\bar{\Phi}}-\frac{F}{\sqrt{2\bar{\Phi}}}-\frac{\partial}{\partial\bar{\Phi}}(\beta(\Phi)\sqrt{2\bar{\Phi}})\right)+\widetilde{V}_d\right]\bar{u}+\\
&\left[\frac{\widetilde{U}_b}{\sqrt{Rk_\Phi}}\left(\frac{\eta F'}{\sqrt{2\bar{\Phi}}}-\sqrt{2\bar{\Phi}}\frac{\partial F}{\partial\bar{\Phi}}-\frac{F}{\sqrt{2\bar{\Phi}}}-\frac{\partial}{\partial\bar{\Phi}}(\beta(\Phi)\sqrt{2\bar{\Phi}})\right)+\widetilde{V}_d\right]\sqrt{\frac{Rk_\Phi}{2\bar{\Phi}}}\frac{\partial\bar{v}}{\partial\eta}+\\
&\frac{\partial}{\partial\eta}\left[\frac{\widetilde{U}_b}{\sqrt{Rk_\Phi}}\left(\frac{\eta F'}{\sqrt{2\bar{\Phi}}}-\sqrt{2\bar{\Phi}}\frac{\partial F}{\partial\bar{\Phi}}-\frac{F}{\sqrt{2\bar{\Phi}}}-\frac{\partial}{\partial\bar{\Phi}}(\beta(\Phi)\sqrt{2\bar{\Phi}})\right)+\widetilde{V}_d\right]\sqrt{\frac{Rk_\Phi}{2\bar{\Phi}}}\bar{v}+\\
&\boxed{\frac{2}{\widetilde{U}}\frac{\partial\widetilde{U}}{\partial\bar{\Psi}}\left[\widetilde{U}_b(F'-1)+\widetilde{U}_d\right]\sqrt{\frac{R}{2\bar{\Phi}k_\Phi}}\bar{u}}=-\frac{1}{\widetilde{U}^2}\frac{1}{2\bar{\Phi}}\frac{\partial\bar{p}}{\partial\eta}+\frac{1}{2\bar{\Phi}}\frac{\partial^2\bar{v}}{\partial\eta^2}-\frac{\kappa^2}{\widetilde{U}^2}\bar{v}-\\
&\frac{2}{\widetilde{U}}\frac{\partial\widetilde{U}}{\partial\bar{\Phi}}\frac{1}{2\bar{\Phi}}\frac{\partial\bar{u}}{\partial\eta},
\end{aligned}
\tag{2.58}
$$

***z*-momentum:**

$$
\begin{aligned}
&-\frac{i\bar{w}}{\widetilde{U}^2}+\left[\widetilde{U}_b(F'-1)+\widetilde{U}_d\right]\left(\frac{\partial\bar{w}}{\partial\bar{\Phi}}-\frac{\eta}{2\bar{\Phi}}\frac{\partial\bar{w}}{\partial\eta}\right)+\\
&\widetilde{U}_b\left(\frac{\eta F'}{\sqrt{2\bar{\Phi}}}-\sqrt{2\bar{\Phi}}\frac{\partial F}{\partial\bar{\Phi}}-\frac{F}{\sqrt{2\bar{\Phi}}}-\frac{\partial}{\partial\bar{\Phi}}(\beta(\Phi)\sqrt{2\bar{\Phi}})\right)\frac{1}{\sqrt{2\bar{\Phi}}}\frac{\partial\bar{w}}{\partial\eta}+\widetilde{V}_d\sqrt{\frac{k_\Phi R}{2\bar{\Phi}}}\frac{\partial\bar{w}}{\partial\eta}+\\
&\left[\widetilde{U}_b(F'-1)+\widetilde{U}_d\right]\frac{1}{\widetilde{U}}\frac{\partial\widetilde{U}}{\partial\bar{\Phi}}\bar{w}=\frac{1}{\widetilde{U}^3}\kappa^2\bar{p}+\frac{1}{2\bar{\Phi}}\frac{\partial^2\bar{w}}{\partial\eta^2}-\frac{\kappa^2}{\widetilde{U}^2}\bar{w}.
\end{aligned}
\tag{2.59}
$$

The Φ-momentum equation has been obtained by dividing both sides by ik_z while the Ψ-momentum equations has been obtained by dividing both sides by

$ik_z\sqrt{\frac{2\bar{\Phi}k_\Phi}{R}}$. In the boundary region equations $\widetilde{U}$ comes from the Navier-Stokes equations in optimal coordinates, while $\widetilde{U}_b$ and $\widetilde{U}_d$ come from the composite solution of the mean flow.

The boundary conditions are the no slip condition at the wall for the three velocity components and the outer boundary conditions are obtained by matching the outer perturbation flow at large distance from the body. The no slip condition is

$$\bar{u} = \bar{v} = \bar{w} = 0, \qquad \text{at} \quad \eta = 0. \tag{2.60}$$

The perturbation velocity components and pressure in (2.55) are imposed to be equal to the outer perturbation velocity components and pressure obtaining

$$\bar{u} \to -\frac{ik_\Phi}{k_z}\hat{w}_\Phi \qquad \text{as} \quad \eta \to \infty, \tag{2.61}$$

$$\bar{v} \to -i\frac{\hat{w}_\Psi}{\kappa\sqrt{2\bar{\Phi}}} \qquad \text{as} \quad \eta \to \infty, \tag{2.62}$$

$$\bar{w} \to \hat{w}_z \qquad \text{as} \quad \eta \to \infty, \tag{2.63}$$

$$\bar{p} \to -i\frac{\sqrt{Rk_\Phi}}{\kappa}\hat{\bar{p}} \qquad \text{as} \quad \eta \to \infty. \tag{2.64}$$

The framed term is in (2.58) because the order of the derivative of the outer mean flow and the streamwise perturbation velocity change by increasing η. In fact, when η is of order 1 the mean flow is a function of $\bar{\Phi}$ only because it is almost the velocity on the body since the boundary layer is very thin and therefore its derivative with respect to $\bar{\Psi}$ is small while the streamwise velocity component is of order 1. However, when $\eta \to \infty$ the derivative of the the outer mean flow with respect to $\bar{\Psi}$ is of order 1 but the streamwise velocity component is of order k_Φ.

	$\frac{\partial \widetilde{U}}{\partial \bar{\Psi}}$	$\bar{u}$	$\sqrt{\frac{R}{2\bar{\Phi}k_\Phi}}$
$\eta = \mathcal{O}(1)$	$\mathcal{O}(k_\Phi)$	$\mathcal{O}(1)$	$\mathcal{O}(k_\Phi^{-1})$
$\eta \to \infty$	$\mathcal{O}(1)$	$\mathcal{O}(k_\Phi)$	$\mathcal{O}(k_\Phi^{-1})$

Tab. 2.2: Order of the framed term in equation (2.58)

The framed term must then be kept in the equation because it is of order 1 both inside and outside the boundary layer since $\sqrt{\frac{R}{2\bar{\Phi}k_\Phi}} = \mathcal{O}(k_\Phi^{-1})$ and the other two contributes are of order k_Φ. Table 2.2 resumes the order of the different parts of the frame term in (2.58)

Large-η equations

In this section the large-η boundary region equations are derived to show that they coincide with the outer perturbation flow equations. This check is very important because the outer boundary conditions for the boundary region equations are obtained by imposing that the velocity components and pressure are equal to the outer perturbation velocity components and pressure. Therefore, the large-η equations are satisfied by the outer velocity and pressure and for this reason they need to coincide with the outer perturbation flow equations. As $\eta \to \infty$ the inner mean flow F and its derivatives go to the following values

$$F' \to 1,$$

$$F \to \eta - \beta(\bar{\Phi}),$$

$$F'' \to 0,$$

$$\frac{\partial F}{\partial \bar{\Phi}} = -\frac{\partial \beta}{\partial \bar{\Phi}}.$$

These limits have been obtained by considering that the inner mean flow F is scaled by the local outer mean flow and taking into account the displacement

effect given by β. For a Rankine body β is not a constant number as for a flat plate, but it varies along the body because the solution is not self-similar. The composite mean flow at large distance from the body reduces to the outer displaced mean flow and the z-momentum equation reduces to

$$-\frac{i\bar{w}}{\widetilde{U}^2}+\widetilde{U}_d\left(\frac{\partial\bar{w}}{\partial\bar{\Phi}}-\frac{\eta}{2\bar{\Phi}}\frac{\partial\bar{w}}{\partial\eta}\right)+\widetilde{V}_d\frac{\partial\bar{w}}{\partial\eta}\sqrt{\frac{k_\Phi R}{2\bar{\Phi}}}+\frac{\bar{w}\widetilde{U}_d}{\widetilde{U}}\frac{\partial\widetilde{U}}{\partial\bar{\Phi}}=\frac{1}{\widetilde{U}^3}\kappa^2\bar{p}+\frac{1}{2\bar{\Phi}}\frac{\partial^2\bar{w}}{\partial\eta^2}-\frac{\kappa^2}{\widetilde{U}^2}\bar{w}. \tag{2.65}$$

The boundary region equations are in ($\bar{\Phi}$-η) coordinates while the outer perturbation equations are in ($\bar{\Phi}_d$-Ψ_d) coordinates. It is necessary to change the coordinates from ($\bar{\Phi}$-η) to ($\bar{\Phi}$-Ψ) as first step. The z-momentum equation becomes

$$-\frac{i\bar{w}}{\widetilde{U}^2}+\widetilde{U}_d\frac{\partial\bar{w}}{\partial\bar{\Phi}}+\widetilde{V}_d\frac{\partial\bar{w}}{\partial\Psi}+\frac{\bar{w}\widetilde{U}_d}{\widetilde{U}}\frac{\partial\widetilde{U}}{\partial\bar{\Phi}}=\frac{1}{\widetilde{U}^3}\kappa^2\bar{p}+\frac{1}{Rk_\Phi}\frac{\partial^2\bar{w}}{\partial\Psi^2}-\frac{\kappa^2}{\widetilde{U}^2}\bar{w}. \tag{2.66}$$

Here it is important to remark that the displaced outer mean velocity $\widetilde{U}_d^*$ and the inner perturbation velocity $\bar{w}^*$ are scaled by the not displaced outer mean velocity $\widetilde{U}^*$. The last one is scaled instead by the uniform mean flow U_∞^*, namely $\widetilde{U}_d=\widetilde{U}_d^*/\widetilde{U}^*$, $\bar{w}=w_z^*/\widetilde{U}^*$ and $\widetilde{U}=\widetilde{U}^*/U_\infty^*$. The coordinates must be changed from ($\bar{\Phi}$-Ψ) to ($\bar{\Phi}_d$-Ψ_d). The displaced potential and streamfunction are functions of the not displaced ones as explained in detail in appendix C, so that they can be written as

$$\Psi_d=\Psi+\Psi_d(\bar{\Phi},\bar{\Psi}),$$

$$\bar{\Phi}_d=\bar{\Phi}+\bar{\Phi}_d(\bar{\Phi},\bar{\Psi}).$$

Ψ_d and Φ_d are a correction of the streamfunction and potential and they are of order k_Φ. The components of the displaced mean velocity can be found by deriving the displaced potential and streamfunction with respect to the not displaced

coordinates because they play the role of the Cartesian coordinates. By deriving the displaced potential and streamfunction the following are obtained

$$\frac{\partial \Psi_d}{\partial \Psi} = 1 + \mathcal{O}(k_\Phi) = \widetilde{U}_d, \qquad \frac{\partial \bar{\Phi}_d}{\partial \bar{\Phi}} = 1 + \mathcal{O}(k_\Phi) = \widetilde{U}_d,$$

$$\frac{\partial \Psi_d}{\partial \bar{\Phi}} = k_\Phi \frac{\partial \Psi_d}{\partial \bar{\Phi}} = k_\Phi \widetilde{V}_d, \qquad \frac{\partial \bar{\Phi}_d}{\partial \Psi} = k_\Phi \frac{\partial \bar{\Phi}_d}{\partial \Psi} = k_\Phi \widetilde{V}_d.$$

The coordinates of (2.66) are changed from ($\bar{\Phi}$-Ψ) to ($\bar{\Phi}_d$-Ψ_d) by using the chain rule and considering the relationships obtained by deriving the displaced coordinates so that equation (2.66) becomes

$$-\frac{i\bar{w}}{\widetilde{U}^2} + \widetilde{U}_d^2 \frac{\partial \bar{w}}{\partial \bar{\Phi}_d} + \frac{\bar{w}\widetilde{U}_d}{\widetilde{U}} \frac{\partial \widetilde{U}}{\partial \bar{\Phi}_d} \widetilde{U}_d = \frac{1}{\widetilde{U}^3} \kappa^2 \bar{p} + \frac{1}{Rk_\Phi} \frac{\partial^2 \bar{w}}{\partial \Psi_d^2} - \frac{\kappa^2}{\widetilde{U}^2} \bar{w}. \tag{2.67}$$

Since the limit of $\eta \to \infty$ is being considered, all $\widetilde{U}$ become $\widetilde{U}_d$ scaled by U_∞^* including the ones which divide $\bar{w}$ and the boundary conditions (2.63) and (2.64) are used because the inner perturbation flow matches the outer perturbation flow at large distance from the body. The boundary conditions used are written again here for convenience

$$\bar{w} \to \hat{w}_z \qquad \text{as} \quad \eta \to \infty,$$

$$\bar{p} \to -i \frac{\sqrt{Rk_\Phi}}{\kappa} \hat{\hat{p}} \qquad \text{as} \quad \eta \to \infty.$$

The displaced outer mean flow scaled by $\widetilde{U}^*$ goes to 1 namely $\widetilde{U}_d \to 1 + \mathcal{O}(k_\Phi)$ because $\widetilde{U}_d^* \to \widetilde{U}^* + \mathcal{O}(k_\Phi)$. Therefore equation (2.67) reduces to the following equation which is the equation for the outer perturbation flow.

$$-\frac{i\hat{w}_z}{\widetilde{U}_d^2} + \frac{\partial \hat{w}_z}{\partial \bar{\Phi}_d} + \frac{\hat{w}_z}{\widetilde{U}_d} \frac{\partial \widetilde{U}_d}{\partial \bar{\Phi}_d} = \frac{-i\kappa}{\widetilde{U}_d^3} \sqrt{Rk_\Phi} \hat{\hat{p}} + \frac{1}{Rk_\Phi} \frac{\partial^2 \hat{w}_z}{\partial \Psi_d^2} - \frac{\kappa^2}{\widetilde{U}_d^2} \hat{w}_z. \tag{2.68}$$

It is interesting to verify that the outer solution satisfies the large-η z-momentum equation. By substituting in equation (2.68) the total spanwise outer velocity component and outer perturbation pressure the following is obtained

$$
\begin{aligned}
&-\frac{i(\hat{w}_{z\mathrm{H}}+ik_z\hat{\varphi})}{\widetilde{U}_d^2}+\frac{\partial(\hat{w}_{z\mathrm{H}}+ik_z\hat{\varphi})}{\partial\bar{\Phi}_d}+\frac{(\hat{w}_{z\mathrm{H}}+ik_z\hat{\varphi})}{\widetilde{U}_d}\frac{\partial\widetilde{U}_d}{\partial\bar{\Phi}_d}= \\
&=\frac{-i\kappa}{\widetilde{U}_d^3}\sqrt{Rk_\Phi}\left(i\widetilde{U}_d\hat{\varphi}-\widetilde{U}_d^3\frac{\partial\hat{\varphi}}{\partial\bar{\Phi}_d}-\hat{\varphi}\widetilde{U}_d^2\frac{\partial\widetilde{U}_d}{\partial\bar{\Phi}_d}+\frac{\widetilde{U}_d^3}{Rk_\Phi}\frac{\partial^2\hat{\varphi}}{\partial\Psi_d^2}-\widetilde{U}_d\frac{k_z^2}{Rk_\Phi}\hat{\varphi}\right)+ \\
&+\frac{1}{Rk_\Phi}\frac{\partial^2(\hat{w}_{z\mathrm{H}}+ik_z\hat{\varphi})}{\partial\Psi_d^2}-\frac{\kappa^2}{\widetilde{U}_d^2}(\hat{w}_{z\mathrm{H}}+ik_z\hat{\varphi}).
\end{aligned}
$$

The homogeneous velocity satisfies the equation without the pressure term and therefore the pressure and the potential terms simplify. Similar steps are employed to check the large-η Ψ-momentum equation coincides with the outer Ψ-momentum equation. The boundary-region Ψ-momentum equation as $\eta\to\infty$ becomes

$$
\begin{aligned}
&-\frac{i\bar{v}}{\widetilde{U}^2}+\widetilde{U}_d\frac{\bar{v}}{2\bar{\Phi}}+\widetilde{U}_d\frac{\partial\bar{v}}{\partial\bar{\Phi}}-\frac{\eta}{2\bar{\Phi}}\widetilde{U}_d\frac{\partial\bar{v}}{\partial\eta}+\underbrace{\sqrt{\frac{Rk_\Phi}{2\bar{\Phi}}}\bar{u}\frac{\partial\widetilde{V}_d}{\partial\bar{\Phi}}}_{\mathcal{O}(k_\Phi)}-\underbrace{\frac{\eta}{2\bar{\Phi}}\sqrt{\frac{Rk_\Phi}{2\bar{\Phi}}}\bar{u}\frac{\partial\widetilde{V}_d}{\partial\eta}}_{\mathcal{O}(k_\Phi)}+ \\
&\widetilde{V}_d\frac{\partial\bar{v}}{\partial\eta}\sqrt{\frac{Rk_\Phi}{2\bar{\Phi}}}+\bar{v}\frac{\partial\widetilde{V}_d}{\partial\eta}\sqrt{\frac{Rk_\Phi}{2\bar{\Phi}}}+\frac{2}{\widetilde{U}}\frac{\partial\widetilde{U}}{\partial\bar{\Psi}}\widetilde{U}_d\bar{u}\sqrt{\frac{R}{2\bar{\Phi}k_\Phi}}=-\frac{1}{\widetilde{U}^2}\frac{1}{2\bar{\Phi}}\frac{\partial\bar{p}}{\partial\eta}+ \\
&\frac{1}{2\bar{\Phi}}\frac{\partial^2\bar{v}}{\partial\eta^2}-\frac{\kappa^2}{\widetilde{U}^2}\bar{v}-\underbrace{\frac{2}{\widetilde{U}}\frac{\partial\widetilde{U}}{\partial\bar{\Phi}}\frac{\partial\bar{u}}{\partial\eta}\frac{1}{2\bar{\Phi}}}_{\mathcal{O}(k_\Phi)}.
\end{aligned}
\tag{2.69}
$$

Terms of order k_Φ deriving from the order of $\bar{u}$ at large η can be neglected. The coordinates are changed from ($\bar{\Phi}$-η) to ($\bar{\Phi}$-Ψ)

$$
\begin{aligned}
&-\frac{i\bar{v}}{\widetilde{U}^2}+\widetilde{U}_d\frac{\bar{v}}{2\bar{\Phi}}+\widetilde{U}_d\frac{\partial\bar{v}}{\partial\bar{\Phi}}+\widetilde{V}_d\frac{\partial\bar{v}}{\partial\Psi}+\bar{v}\frac{\partial\widetilde{V}_d}{\partial\Psi}+\frac{2}{\widetilde{U}}\frac{\partial\widetilde{U}}{\partial\bar{\Psi}}\widetilde{U}_d\bar{u}\sqrt{\frac{R}{2\bar{\Phi}k_\Phi}}= \\
&=-\frac{1}{\widetilde{U}^2}\frac{1}{2\bar{\Phi}}\frac{\partial\bar{p}}{\partial\Psi}\sqrt{\frac{Rk_\Phi}{2\bar{\Phi}}}+\frac{1}{Rk_\Phi}\frac{\partial^2\bar{v}}{\partial\Psi^2}-\frac{\kappa^2}{\widetilde{U}^2}\bar{v}.
\end{aligned}
\tag{2.70}
$$

The coordinates are changed from ($\bar{\Phi}$-Ψ) to ($\bar{\Phi}_d$-Ψ_d) and the boundary conditions (2.61), (2.62) and (2.64) are used

$$-\frac{1}{\widetilde{U}_d^2}\frac{\hat{w}_\Psi}{\kappa\sqrt{2\bar{\Phi}_d}}-\cancel{\frac{i\hat{w}_\Psi}{\kappa(2\bar{\Phi}_d)^{3/2}}}-\frac{\partial\hat{w}_\Psi}{\partial\bar{\Phi}_d}\frac{i}{\kappa\sqrt{2\bar{\Phi}_d}}+\cancel{\frac{i\hat{w}_\Psi}{\kappa(2\bar{\Phi}_d)^{3/2}}}-\underbrace{\cancel{\frac{i\hat{w}_\Psi}{\kappa\sqrt{2\bar{\Phi}_d}}\frac{\partial\widetilde{V}_d}{\partial\bar{\Psi}_d}}k_\Phi}_{\mathcal{O}(k_\Phi)}-$$
$$i\frac{2}{\widetilde{U}_d}\frac{\partial\widetilde{U}_d}{\partial\bar{\Psi}_d}\frac{\hat{w}_\Phi}{\kappa\sqrt{2\bar{\Phi}_d}}=\frac{i}{\widetilde{U}_d^2}\frac{1}{\kappa\sqrt{2\bar{\Phi}_d}}\frac{\partial\hat{\tilde{p}}}{\partial\Psi_d}-\frac{i}{Rk_\Phi}\frac{1}{\kappa\sqrt{2\bar{\Phi}_d}}\frac{\partial\hat{w}_\Psi}{\partial\Psi_d}+i\frac{\kappa^2}{\widetilde{U}_d^2}\frac{\hat{w}_\Psi}{\kappa\sqrt{2\bar{\Phi}_d}}. \tag{2.71}$$

Both sides are multiplied by $i\kappa\sqrt{2\bar{\Phi}}$

$$-\frac{i}{\widetilde{U}_d^2}\hat{w}_\Psi+\frac{\partial\hat{w}_\Psi}{\partial\bar{\Phi}_d}+\frac{2}{\widetilde{U}_d}\frac{\partial\widetilde{U}_d}{\partial\bar{\Psi}_d}\hat{w}_\Phi=-\frac{1}{\widetilde{U}_d^2}\frac{\partial\hat{\tilde{p}}}{\partial\Psi_d}+\frac{1}{Rk_\Phi}\frac{\partial\hat{w}_\Psi}{\partial\Psi_d}-\frac{\kappa^2}{\widetilde{U}_d^2}\hat{w}_\Psi. \tag{2.72}$$

The outer solution satisfies the large-η Ψ-momentum equation and it can be verified by following the same line of reasoning for the z-momentum equation. The outer streamwise, normal velocity components and outer pressure are substitute in equation (2.72)

$$-\frac{i}{\widetilde{U}_d^2}\left(\hat{w}_{\Psi\mathrm{H}}+\widetilde{U}_d\frac{\partial\hat{\varphi}}{\partial\Psi_d}\right)+\frac{\partial\left(\hat{w}_{\Psi\mathrm{H}}+\widetilde{U}_d\frac{\partial\hat{\varphi}}{\partial\bar{\Psi}_d}\right)}{\partial\bar{\Phi}_d}+\frac{2}{\widetilde{U}_d}\frac{\partial\widetilde{U}_d}{\partial\bar{\Psi}_d}\hat{w}_{\Phi\mathrm{H}}=$$
$$-\frac{1}{\widetilde{U}_d^2}\frac{\partial\left(i\widetilde{U}_d\hat{\varphi}-\widetilde{U}_d^3\frac{\partial\hat{\varphi}}{\partial\bar{\Phi}_d}-\hat{\varphi}\widetilde{U}_d^2\frac{\partial\widetilde{U}_d}{\partial\bar{\Phi}_d}+\frac{\widetilde{U}_d^3}{Rk_\Phi}\frac{\partial^2\hat{\varphi}}{\partial\Psi_d^2}-\widetilde{U}_d\frac{k_z^2}{Rk_\Phi}\hat{\varphi}\right)}{\partial\Psi_d}+$$
$$+\frac{1}{Rk_\Phi}\frac{\partial\left(\hat{w}_{\Psi\mathrm{H}}+\widetilde{U}_d\frac{\partial\hat{\varphi}}{\partial\bar{\Psi}_d}\right)}{\partial\Psi_d}-\frac{\kappa^2}{\widetilde{U}_d^2}\left(\hat{w}_{\Psi\mathrm{H}}+\widetilde{U}_d\frac{\partial\hat{\varphi}}{\partial\Psi_d}\right).$$

The homogeneous velocity satisfies the equation without the pressure term and therefore the pressure and the potential terms simplify.

2.4.3 Initial conditions

In this section the initial condition for the boundary region equations is derived. It is necessary because the equations are parabolic in the streamwise direction and they are solved numerically by marching downstream. The initial condition

is in the vicinity of the stagnation point where the mean flow solution is the well known Hiemenz flow. Here, the coordinates are x_{H} and y_{H} as shown in figure 2.1. They are respectively parallel and orthogonal at the stagnation point. The coordinates x_{H}-y_{H} are rescaled as

$$\bar{x}_{\text{H}} = k_\Phi x_{\text{H}}, \qquad \eta_{\text{H}} = y_{\text{H}} \sqrt{\frac{\alpha R k_\Phi}{k}},$$

where $k = 2\pi L^*/\lambda_\Phi^* = \mathcal{O}(1)$. The flow at the stagnation point is decomposed in the Hiemenz composite mean flow and a small perturbation

$$(\mathbf{u}_{\text{H}}, p_{\text{H}}) = (U_{\text{HM}}, V_{\text{HM}}, 0, P) + \epsilon \left(\frac{ik_z}{k_\Phi} \bar{u}_{\text{H}}, \frac{ik_z}{A} \bar{v}_{\text{H}}, \bar{w}_{\text{H}}, i\kappa \sqrt{\frac{k_\Phi}{R}} \bar{p}_{\text{H}} \right), \tag{2.73}$$

where $\bar{u}_{\text{H}}$, $\bar{v}_{\text{H}}$ and $\bar{w}_{\text{H}}$ are the velocity components along x_{H}, η_{H} and z respectively, $\bar{p}_{\text{H}}$ is the pressure at the stagnation point and

$$A = \sqrt{\frac{\alpha R k_\Phi}{k}} = \mathcal{O}(1), \tag{2.74}$$

and all the velocities are scaled by the uniform flow U_∞^*.

Composite Hiemenz flow

In this section the composite Hiemenz mean flow is derived. It is given by the summation of the inner and the outer velocity and the subtraction of the common part. The latter is the limit of the inner velocity for large η_{H} and the limit of the outer velocity for small y_{H}. These two limits are the same

$$U_{\text{HM}} = \frac{\alpha}{k} \bar{x}_{\text{Hd}} (F'_{\text{H}} - 1) + U_{\text{Hd}}, \tag{2.75}$$

$$V_{\text{HM}} = -k_\Phi \sqrt{\frac{\alpha}{k R k_\Phi}} (F_{\text{H}} - \eta_{\text{H}} + \beta_{\text{H}}) + V_{\text{Hd}}, \tag{2.76}$$

where β_{H} is the displacement thickness of the Hiemenz boundary layer. It is observed that the streamwise velocity component is of order 1, while the normal component is of order k_Φ near the body and of order 1 at large distance from it. The outer velocity components U_{Hd} and V_{Hd} are found analytically as functions of the displaced stagnation point coordinates. This is possible because the potential is known analytically in x_{HL}-y_{HL} coordinates

$$\Phi_{\mathrm{L}} = -y_{\mathrm{HL}} + \frac{\Lambda}{2\pi}\ln\left(y_{\mathrm{HL}}^2 + \frac{\Lambda^2}{4\pi^2} + \frac{\Lambda}{\pi}y_{\mathrm{HL}} + x_{\mathrm{HL}}^2\right) - \frac{\Lambda}{2\pi}\left[\ln\left(\frac{\Lambda}{2\pi}\right) - 1\right]. \quad (2.77)$$

The outer velocity components are obtained by deriving the potential with respect to x_{HL} and y_{HL} and by changing the scales

$$x_{\mathrm{HL}} = \frac{\bar{x}_{\mathrm{Hd}}}{k} \qquad\qquad y_{\mathrm{HL}} = \frac{k_\Phi y_{\mathrm{Hd}}}{k},$$

$$U_{\mathrm{Hd}} = \frac{\Lambda \bar{x}_{\mathrm{Hd}}}{2\pi k}\frac{1}{\left[\left(\frac{k_\Phi}{k}y_{\mathrm{Hd}}\right)^2 + \frac{\Lambda^2}{4\pi^2} + \frac{\Lambda k_\Phi}{\pi k}y_{\mathrm{Hd}}\right]}, \quad (2.78)$$

$$V_{\mathrm{Hd}} = -1 + \frac{\Lambda}{4\pi}\frac{\frac{-2k_\Phi}{k}y_{\mathrm{Hd}} + \frac{\Lambda}{\pi}}{\left[\left(\frac{k_\Phi}{k}y_{\mathrm{Hd}}\right)^2 + \frac{\Lambda^2}{4\pi^2} + \frac{\Lambda k_\Phi}{\pi k}y_{\mathrm{Hd}}\right]}. \quad (2.79)$$

The outer mean flow Hiemenz components (2.78)-(2.79) have been obtained by considering that $\bar{x}_{\mathrm{Hd}}$ is small because the stagnation point is near the origin of the system.

The limit of (2.78) and (2.79) for $y_{\mathrm{Hd}} \to 0$ is the common part of the composite solution (2.75)-(2.76)

$$\lim_{y_{\mathrm{Hd}}\to 0} U_{\mathrm{Hd}} = \frac{\alpha}{k}\bar{x}_{\mathrm{Hd}},$$

$$\lim_{y_{\mathrm{Hd}}\to 0} V_{\mathrm{Hd}} = -\frac{\alpha k_\Phi}{k}y_{\mathrm{Hd}}.$$

The limit of (2.78) and (2.79) for $y_{\mathrm{Hd}} \to \infty$ is the uniform mean flow upstream. However, the velocity components are swapped because the coordinates at the stagnation point are rotated compared to the ones upstream.

$$\lim_{y_{\mathrm{Hd}}\to\infty} U_{\mathrm{Hd}} = 0,$$

$$\lim_{y_{\mathrm{Hd}}\to\infty} V_{\mathrm{Hd}} = -1.$$

Since the inner Hiemenz velocity is a function of η_{H} it is convenient to write the outer velocity in the same coordinate

$$y_{\mathrm{Hd}} = \sqrt{\frac{k}{\alpha R k_\Phi}}(\eta_{\mathrm{H}} - \beta_{\mathrm{H}}),$$

$$U_{\mathrm{Hd}} = \frac{\Lambda \bar{x}_{\mathrm{H}}}{2\pi k} \frac{1}{\left[\left(\frac{k_\Phi}{k}\sqrt{\frac{k}{\alpha R k_\Phi}}(\eta_{\mathrm{H}} - \beta_{\mathrm{H}})\right)^2 + \frac{\Lambda^2}{4\pi^2} + \frac{\Lambda k_\Phi}{\pi k}\sqrt{\frac{k}{\alpha R k_\Phi}}(\eta_{\mathrm{H}} - \beta_{\mathrm{H}})\right]}, \tag{2.80}$$

$$V_{\mathrm{Hd}} = -1 + \frac{\Lambda}{4\pi} \frac{\frac{-2k_\Phi}{k}\sqrt{\frac{k}{\alpha R k_\Phi}}(\eta_{\mathrm{H}} - \beta_{\mathrm{H}}) + \frac{\Lambda}{\pi}}{\left[\left(\frac{k_\Phi}{k}\sqrt{\frac{k}{\alpha R k_\Phi}}(\eta_{\mathrm{H}} - \beta_{\mathrm{H}})\right)^2 + \frac{\Lambda^2}{4\pi^2} + \frac{\Lambda k_\Phi}{\pi k}\sqrt{\frac{k}{\alpha R k_\Phi}}(\eta_{\mathrm{H}} - \beta_{\mathrm{H}})\right]}. \tag{2.81}$$

Hiemenz-boundary region equations

In this section the Hiemenz boundary region equations are derived. They are obtained by substituting the decomposition (2.73) into the Navier-Stokes equations in Cartesian coordinates and collecting terms of order ϵ

$$\frac{\partial \bar{u}_{\mathrm{H}}}{\partial \bar{x}_{\mathrm{H}}} + \frac{\partial \bar{v}_{\mathrm{H}}}{\partial \eta_{\mathrm{H}}} + \bar{w}_{\mathrm{H}} = 0, \tag{2.82}$$

$$-i\bar{u}_{\mathrm{H}} + U_{\mathrm{HM}}\frac{\partial \bar{u}_{\mathrm{H}}}{\partial \bar{x}_{\mathrm{H}}} + \bar{u}_{\mathrm{H}}\frac{\partial U_{\mathrm{HM}}}{\partial \bar{x}_{\mathrm{H}}} + A\widetilde{V}_{\mathrm{HM}}\frac{\partial \bar{u}_{\mathrm{H}}}{\partial \eta_{\mathrm{H}}} + \bar{v}_{\mathrm{H}}\frac{\partial U_{\mathrm{HM}}}{\partial \eta_{\mathrm{H}}} = \frac{k_\Phi}{R}\frac{\partial^2 \bar{u}_{\mathrm{H}}}{\partial \bar{x}_{\mathrm{H}}^2} + \frac{A^2}{Rk_\Phi}\frac{\partial^2 \bar{u}_{\mathrm{H}}}{\partial \eta_{\mathrm{H}}^2} - \kappa^2 \bar{u}_{\mathrm{H}}, \tag{2.83}$$

$$-i\frac{\bar{v}_{\mathrm{H}}}{A}+\frac{U_{\mathrm{HM}}}{A}\frac{\partial\bar{v}_{\mathrm{H}}}{\partial\bar{x}_{\mathrm{H}}}+\widetilde{V}_{\mathrm{HM}}\frac{\partial\bar{v}_{\mathrm{H}}}{\partial\eta_{\mathrm{H}}}+\bar{v}_{\mathrm{H}}\frac{\partial\widetilde{V}_{\mathrm{HM}}}{\partial\eta_{\mathrm{H}}}=-\frac{\kappa}{k_z}\frac{A}{\sqrt{Rk_\Phi}}\frac{\partial\bar{p}_{\mathrm{H}}}{\partial\eta_{\mathrm{H}}}+\frac{k_\Phi}{AR}\frac{\partial^2\bar{v}_{\mathrm{H}}}{\partial\bar{x}_{\mathrm{H}}^2}+\frac{A}{Rk_\Phi}\frac{\partial^2\bar{v}_{\mathrm{H}}}{\partial\eta_{\mathrm{H}}^2}-\frac{\kappa^2}{A}\bar{v}_{\mathrm{H}},\tag{2.84}$$

$$-i\bar{w}_{\mathrm{H}}+U_{\mathrm{HM}}\frac{\partial\bar{w}_{\mathrm{H}}}{\partial\bar{x}_{\mathrm{H}}}+A\widetilde{V}_{\mathrm{HM}}\frac{\partial\bar{w}_{\mathrm{H}}}{\partial\eta_{\mathrm{H}}}=\kappa^2\bar{p}_{\mathrm{H}}+\frac{k_\Phi}{R}\frac{\partial^2\bar{w}_{\mathrm{H}}}{\partial\bar{x}_{\mathrm{H}}^2}+\frac{A^2}{Rk_\Phi}\frac{\partial^2\bar{w}_{\mathrm{H}}}{\partial\eta_{\mathrm{H}}^2}-\kappa^2\bar{w}_{\mathrm{H}},\tag{2.85}$$

where $\widetilde{V}_{\mathrm{HM}}=V_{\mathrm{HM}}/k_\Phi$. The second derivative with respect to $\bar{x}_{\mathrm{H}}$ are not neglected even if they are of order k_Φ because in the large-η_{H} limit that term becomes important. From equations (2.82)-(2.85) it is observed that inside the boundary layer, where η_{H} is of order 1 and the normal mean velocity component is of order k_Φ, all the terms are of order 1. However, as η_{H} becomes very large, the outer mean normal component becomes of order 1 as in the limit of large-η_{H}, $V_{\mathrm{Hd}}\to-1$, but the coordinates rotate moving upstream and their scale changes as well. Therefore even for large η_{H} all the terms in equations (2.82)-(2.85) are of order 1. It is worth checking if the upstream limit of the outer solution written in Hiemenz-coordinates satisfies the large-η_{H} limit of the Hiemenz boundary region equations. The limit is where the mean flow is still uniform but after the grid where the gust has already started to decay. The outer solution upstream for the three velocity components in optimal displaced coordinates is given by

$$\hat{w}_\Phi=\hat{u}_\Phi^\infty e^{i(\bar{\Phi}_d-\bar{\Phi}_{d0})+ik_\Psi\Psi_d-(\kappa^2+\kappa_2^2)(\bar{\Phi}_d-\bar{\Phi}_{d0})},$$

$$\hat{w}_\Psi=\hat{u}_\Psi^\infty e^{i(\bar{\Phi}_d-\bar{\Phi}_{d0})+ik_\Psi\Psi_d-(\kappa^2+\kappa_2^2)(\bar{\Phi}_d-\bar{\Phi}_{d0})},$$

$$\hat{w}_z=\hat{u}_z^\infty e^{i(\bar{\Phi}_d-\bar{\Phi}_{d0})+ik_\Psi\Psi_d-(\kappa^2+\kappa_2^2)(\bar{\Phi}_d-\bar{\Phi}_{d0})}.$$

The above equations need to be written in the same coordinates as the Hiemenz boundary region equations without displacement. The transformation is easy because in the upstream limit the optimal coordinates coincide with the Cartesian coordinates

$$\Phi = -y_{\mathrm{H}} \Rightarrow \Phi = -\frac{\eta_{\mathrm{H}}}{A} \Rightarrow \bar{\Phi} = -\frac{k_\Phi \eta_{\mathrm{H}}}{A},$$

$$\Psi = x_{\mathrm{H}} \Rightarrow \Psi = \frac{\bar{x}_{\mathrm{H}}}{k_\Phi}.$$

The upstream limit of the outer solution in the Hiemenz coordinates is then

$$\hat{w}_\Phi = \hat{u}_\Phi^\infty \exp\left[i\left(-\frac{k_\Phi \eta_{\mathrm{H}}}{A} + \frac{k_\Phi \eta_{\mathrm{H0}}}{A}\right) + ik_\Psi \frac{\bar{x}_{\mathrm{H}}}{k_\Phi} - (\kappa^2 + \kappa_2^2)\left(-\frac{k_\Phi \eta_{\mathrm{H}}}{A} + \frac{k_\Phi \eta_{\mathrm{H0}}}{A}\right)\right],$$

$$\hat{w}_\Psi = \hat{u}_\Psi^\infty \exp\left[i\left(-\frac{k_\Phi \eta_{\mathrm{H}}}{A} + \frac{k_\Phi \eta_{\mathrm{H0}}}{A}\right) + ik_\Psi \frac{\bar{x}_{\mathrm{H}}}{k_\Phi} - (\kappa^2 + \kappa_2^2)\left(-\frac{k_\Phi \eta_{\mathrm{H}}}{A} + \frac{k_\Phi \eta_{\mathrm{H0}}}{A}\right)\right],$$

$$\hat{w}_z = \hat{u}_z^\infty \exp\left[i\left(-\frac{k_\Phi \eta_{\mathrm{H}}}{A} + \frac{k_\Phi \eta_{\mathrm{H0}}}{A}\right) + ik_\Psi \frac{\bar{x}_{\mathrm{H}}}{k_\Phi} - (\kappa^2 + \kappa_2^2)\left(-\frac{k_\Phi \eta_{\mathrm{H}}}{A} + \frac{k_\Phi \eta_{\mathrm{H0}}}{A}\right)\right].$$

The amplitude of the gust is scaled by U_∞^* as are the velocity components at the stagnation point. In the large-η_{H} limit the streamwise composite mean flow velocity goes to 0, the normal composite mean flow velocity goes to -1, the pressure goes to 0 and the three velocity components go to the decaying upstream gust, but the streamwise and the normal components are swapped, because the coordinates rotate

$$\bar{u}_{\mathrm{H}} \to -i\frac{k_\Phi}{k_z}\hat{u}_\Psi^\infty e^{i(-\frac{k_\Phi \eta_{\mathrm{H}}}{A} + \frac{k_\Phi \eta_{\mathrm{H0}}}{A}) + ik_\Psi \frac{\bar{x}_{\mathrm{H}}}{k_\Phi} - (\kappa^2+\kappa_2^2)(-\frac{k_\Phi \eta_{\mathrm{H}}}{A} + \frac{k_\Phi \eta_{\mathrm{H0}}}{A})},$$

$$\bar{v}_{\mathrm{H}} \to i\frac{A}{k_z}\hat{u}_\Phi^\infty e^{i(-\frac{k_\Phi \eta_{\mathrm{H}}}{A} + \frac{k_\Phi \eta_{\mathrm{H0}}}{A}) + ik_\Psi \frac{\bar{x}_{\mathrm{H}}}{k_\Phi} - (\kappa^2+\kappa_2^2)(-\frac{k_\Phi \eta_{\mathrm{H}}}{A} + \frac{k_\Phi \eta_{\mathrm{H0}}}{A})},$$

$$\bar{w}_{\mathrm{H}} \rightarrow \hat{u}_z^{\infty} e^{i(-\frac{k_\Phi \eta_{\mathrm{H}}}{A}+\frac{k_\Phi \eta_{\mathrm{H}0}}{A})+ik_\Psi \frac{\bar{x}_{\mathrm{H}}}{k_\Phi}-(\kappa^2+\kappa_2^2)(-\frac{k_\Phi \eta_{\mathrm{H}}}{A}+\frac{k_\Phi \eta_{\mathrm{H}0}}{A})}.$$

Taking the large-η_{H} limit of the continuity Hiemenz boundary region equation gives the equation of the gust

$$k_\Phi \hat{u}_\Phi^{\infty} + k_\Psi \hat{u}_\Psi^{\infty} + k_z \hat{u}_z^{\infty} + \frac{ik_\Phi}{k_z}(\kappa^2+\kappa_2^2) = 0,$$

where k_Φ is small, thus the balance upstream is between the normal and spanwise velocity component, as expected. Following the same line of reasoning for the momentum equations it is demonstrated that the upstream limit of the outer solution satisfies the large-η_{H} limit of the Hiemenz boundary region equations

Expansion Hiemenz flow

The velocity and pressure at $\bar{x}_{\mathrm{Hd}} \ll 1$ can be expressed as a power series, where the exponents for the first term of the series are found by the dominant balance of the boundary region equations.

$$\bar{u}_{\mathrm{H}} = \bar{x}_{\mathrm{H}} U_0(\eta_{\mathrm{H}}),$$

$$\bar{v}_{\mathrm{H}} = V_0(\eta_{\mathrm{H}}),$$

$$\bar{w}_{\mathrm{H}} = W_0(\eta_{\mathrm{H}}),$$

$$\bar{p}_{\mathrm{H}} = P_0(\eta_{\mathrm{H}}),$$

$$U_{\mathrm{HM}} = \bar{x}_{\mathrm{Hd}} \bar{U}_{\mathrm{HM}}(\eta_{\mathrm{H}}),$$

$$\widetilde{V}_{\text{НМ}} = \bar{V}_{\text{НМ}}(\eta_{\text{Н}}).$$

The expansion of the streamwise mean flow is validated by (2.78). By substituting the above expansions in equations (2.82)-(2.85) a system of ordinary differential equations is obtained

$$U_0 + V_0' + W_0 = 0, \tag{2.86}$$

$$-iU_0 + 2\bar{U}_{\text{НМ}}U_0 + \frac{A}{k_\Phi}\bar{V}_{\text{НМ}}U_0' + V_0\bar{U}_{\text{НМ}}' = \frac{A^2}{Rk_\Phi}U_0'' - \kappa^2 U_0, \tag{2.87}$$

$$-\frac{i}{A}V_0 + \frac{\bar{V}_{\text{НМ}}}{k_\Phi}V_0' + \frac{V_0}{k_\Phi}\bar{V}_{\text{НМ}}' = -\frac{\kappa}{k_z}\frac{A}{\sqrt{Rk_\Phi}}P_0' + \frac{A}{Rk_\Phi}V_0'' - \frac{\kappa^2}{A}V_0, \tag{2.88}$$

$$-iW_0 + \frac{A}{k_\Phi}\bar{V}_{\text{НМ}}W_0' = \kappa^2 P_0 + \frac{A^2}{Rk_\Phi}W_0'' - \kappa^2 W_0. \tag{2.89}$$

The system (2.86)-(2.89) needs 7 boundary conditions.

- Three of them are the no slip boundary conditions at the wall for the three velocity components

$$U_0 = V_0 = W_0 = 0. \tag{2.90}$$

- The outer boundary condition for the streamwise velocity component U_0 is zero because it cannot match the outer perturbation velocity as this is of smaller order outside the boundary layer

$$U_0 \to 0 \qquad \text{when} \qquad \eta_{\text{Н}} \gg 1. \tag{2.91}$$

- From the continuity equation (2.86) it is evident that for large $\eta_{\text{Н}}$ the balance is between the normal and spanwise velocity components as the streamwise velocity component is zero. Since the continuity equation must

be satisfied for large η_{H}, the outer boundary conditions for the spanwise velocity component and the derivative with respect to η_{H} of the normal velocity component must be equal and opposite. Therefore, the outer boundary condition for the spanwise velocity component is given by matching the outer flow and the outer boundary condition for the normal velocity component is imposed on its derivative

$$V_0' \to -\hat{w}_z \qquad \text{when} \qquad \eta_{\mathrm{H}} \gg 1, \tag{2.92}$$

$$W_0 \to \hat{w}_z \qquad \text{when} \qquad \eta_{\mathrm{H}} \gg 1. \tag{2.93}$$

- The inner pressure matches the outer perturbation pressure of the Hiemenz flow

$$P_0 \to \hat{\hat{p}} \qquad \text{when} \qquad \eta_{\mathrm{H}} \gg 1. \tag{2.94}$$

An important consideration on the boundary conditions for equations (2.86)-(2.89) must be pointed out. For $\eta_{\mathrm{H}} \to \infty$ the streamwise and normal velocity components are swapped because the coordinates are rotated at the stagnation point. The streamwise component matches the normal component of the gust and the normal component matches the streamwise component of the gust with opposite sign. Therefore, upstream the balance of the continuity equation is between the streamwise U_0 and spanwise W_0 components. The maximum η_{H} where the boundary condition for equations (2.86)-(2.89) is imposed must be large enough to be outside the Hiemenz boundary layer but not too large because the contribution of the streamwise velocity component must still be small in order to have the balance between the normal and spanwise velocities. Table 2.3 gives a further explanation of the changing of the contributions of the velocity components.

$\eta_{\mathrm{H}} = \mathcal{O}(1)$	$\frac{\partial \bar{u}_{\mathrm{H}}}{\partial \bar{x}_{\mathrm{H}}} + \frac{\partial \bar{v}_{\mathrm{H}}}{\partial \eta_{\mathrm{H}}} + \bar{w}_{\mathrm{H}} = 0$	Inside the boundary layer the balance is among the three terms.
$\eta_{\mathrm{H}} \gg 1$	$\frac{\partial \bar{u}_{\mathrm{H}}}{\partial \bar{x}_{\mathrm{H}}} + \boxed{\frac{\partial \bar{v}_{\mathrm{H}}}{\partial \eta_{\mathrm{H}}}} + \boxed{\bar{w}_{\mathrm{H}}} = 0$	At large η_{H} the balance is between the normal and spanwise components.
$\eta_{\mathrm{H}} \to \infty$	$\boxed{\frac{\partial \bar{u}_{\mathrm{H}}}{\partial \bar{x}_{\mathrm{H}}}} + \frac{\partial \bar{v}_{\mathrm{H}}}{\partial \eta_{\mathrm{H}}} + \boxed{\bar{w}_{\mathrm{H}}} = 0$	As $\eta_{\mathrm{H}} \to \infty$ the balance is between the streamwise and spanwise components.

Tab. 2.3: Balance of the continuity equation by varying η_{H}

The solution to equations (2.86)-(2.89) is solved numerically with the boundary conditions (2.90),(2.91),(2.92),(2.93) and (2.94) and it gives the velocity components along the $\bar{x}_{\mathrm{H}}$-η_{H} coordinates. However, the boundary region equations are in optimal coordinates and the initial condition is imposed at the initial $\bar{\Phi}$. The following considerations are drawn:

- The spanwise initial component W_0 is a function of η_{H} only, therefore it can be used as it is.

- The streamwise velocity component U_0 is a function of $\bar{x}_{\mathrm{H}}$-η_{H}. In order to find the initial streamwise component, the initial $\bar{\Phi}$ is fixed and for every η the corresponding $\bar{x}_{\mathrm{H}}$ is found and the initial streamwise velocity component is found by multiplying $\bar{x}_{\mathrm{H}}$ by U_0.

- The initial normal velocity component is found by integrating the continuity equation in optimal coordinates.

- The initial velocity components obtained must also be rescaled by the local outer mean flow as the velocities in the boundary region equations.

2.5 Summary of equations

In this section a summary of the equations derived is presented.

2.5.1 Outer mean flow

The outer mean flow is known in polar and Cartesian coordinates, given by a uniform flow combined with a source flow. Equation (2.12)

$$\widetilde{U} = \sqrt{\left(\frac{\partial \Phi_{\mathrm{L}}}{\partial r}\right)^2 + \left(\frac{1}{r}\frac{\partial \Phi_{\mathrm{L}}}{\partial \theta}\right)^2} = \sqrt{1 + \frac{\Lambda \cos\theta}{\pi r} + \frac{\Lambda^2}{4\pi^2 r^2}},$$

is inverted numerically to have the outer mean flow as function of the independent coordinates Φ-Ψ by using Newton-Raphson algorithm. The displaced outer mean flow $\widetilde{U}_d$ is then found in the same fashion in coordinates Φ_d-Ψ_d.

2.5.2 Inner mean flow

The inner mean flow is found by numerically solving the partial differential equation (2.25)

$$F''' + FF'' + 2m(\Phi_{\mathrm{L}})(1 - F'^2) = 2\Phi_{\mathrm{L}}(F'F'_{\Phi_{\mathrm{L}}} - F_{\Phi_{\mathrm{L}}}F''),$$

with the boundary conditions (2.27)

$$F(\Phi_{\mathrm{L}}, 0) = 0, \qquad F'(\Phi_{\mathrm{L}}, 0) = 0, \qquad F'(\Phi_{\mathrm{L}}, \infty) = 1.$$

Equation (2.25) needs an initial condition, which is found by solving the ordinary differential equation (2.28), also known as Hiemenz equation for a stagnation point flow

$$F''' + FF'' - F'^2 + 1 = 0,$$

with the boundary conditions (2.29)

$$F(0) = 0, \qquad F'(0) = 0, \qquad F'(\infty) = 1.$$

2.5.3 Outer perturbation flow

The outer perturbation velocity is solved by employing Helmholtz decomposition which consists in dividing the velocity into two contributions: the homogeneous part $\mathbf{w}_{\mathrm{H}}$ related with the imposed upstream velocity field and the potential part $\nabla\hat{\varphi}$ related with the pressure fluctuations. The three components of $\mathbf{w}_{\mathrm{H}}$ are found by solving the partial differential equations (2.35)-(2.37)

$$-\frac{i}{\widetilde{U}_d^2}\hat{w}_{\Phi\mathrm{H}}+\frac{\partial\hat{w}_{\Phi\mathrm{H}}}{\partial\bar{\Phi}_d}+\frac{2}{\widetilde{U}_d}\frac{\partial\widetilde{U}_d}{\partial\bar{\Phi}_d}\hat{w}_{\Phi\mathrm{H}}=\frac{1}{Rk_\Phi}\left(\frac{\partial^2\hat{w}_{\Phi\mathrm{H}}}{\partial\Psi_d^2}-\frac{k_z^2}{\widetilde{U}_d^2}\hat{w}_{\Phi\mathrm{H}}\right),$$

$$-\frac{i}{\widetilde{U}_d^2}\hat{w}_{\Psi\mathrm{H}}+\frac{\partial\hat{w}_{\Psi\mathrm{H}}}{\partial\bar{\Phi}_d}+\frac{2}{\widetilde{U}_d}\frac{\partial\widetilde{U}_d}{\partial\bar{\Psi}_d}\hat{w}_{\Phi\mathrm{H}}=\frac{1}{Rk_\Phi}\left(\frac{\partial^2\hat{w}_{\Psi\mathrm{H}}}{\partial\Psi_d^2}-\frac{k_z^2}{\widetilde{U}_d^2}\hat{w}_{\Psi\mathrm{H}}\right),$$

$$-\frac{i}{\widetilde{U}_d^2}\hat{w}_{z\mathrm{H}}+\frac{\partial\hat{w}_{z\mathrm{H}}}{\partial\bar{\Phi}_d}+\frac{1}{\widetilde{U}_d}\frac{\partial\widetilde{U}_d}{\partial\bar{\Phi}_d}\hat{w}_{z\mathrm{H}}=\frac{1}{Rk_\Phi}\left(\frac{\partial^2\hat{w}_{z\mathrm{H}}}{\partial\Psi_d^2}-\frac{k_z^2}{\widetilde{U}_d^2}\hat{w}_{z\mathrm{H}}\right).$$

The semi-analytical solution of (2.35)-(2.37) is found by matching the gust upstream and it is given by (2.44),(2.47),(2.43)

$$\hat{w}_{\Phi\mathrm{H}}=\hat{u}_\Phi^\infty\exp\left[-\kappa_2^2(\bar{\Phi}_d-\bar{\Phi}_{d0})+ik_\Psi\Psi_d-\int_{\bar{\Phi}_{d0}}^{\bar{\Phi}_d}\left(-\frac{i}{\widetilde{U}_d^2}+\frac{2}{\widetilde{U}_d}\frac{\partial\widetilde{U}_d}{\partial\bar{\Phi}_d}+\frac{\kappa^2}{\widetilde{U}_d^2}\right)d\bar{\Phi}_d\right],$$

$$\hat{w}_{\Psi\mathrm{H}}=\exp\left[-\kappa_2^2(\bar{\Phi}_d-\bar{\Phi}_{d0})+ik_\Psi\Psi_d-\int_{\bar{\Phi}_{d0}}^{\bar{\Phi}_d}\left(-\frac{i}{\widetilde{U}_d^2}+\frac{\kappa^2}{\widetilde{U}_d^2}\mathrm{d}\bar{\Phi}\right)\right]$$
$$\left(\hat{u}_\Psi^\infty+\int_{\bar{\Phi}_{d0}}^{\bar{\Phi}_d}\mathrm{RHS}(\chi,\tau)e^{\kappa_2^2\tau}\mathrm{d}\tau\right),$$

$$\hat{w}_{z\mathrm{H}}=\hat{u}_z^\infty\exp\left[-\kappa_2^2(\bar{\Phi}_d-\bar{\Phi}_{d0})+ik_\Psi\Psi_d-\int_{\bar{\Phi}_{d0}}^{\bar{\Phi}_d}\left(-\frac{i}{\widetilde{U}_d^2}+\frac{1}{\widetilde{U}_d}\frac{\partial\widetilde{U}_d}{\partial\bar{\Phi}_d}+\frac{\kappa^2}{\widetilde{U}_d^2}\right)\mathrm{d}\bar{\Phi}_d\right].$$

The perturbation potential $\hat{\varphi}$ is found by solving the partial differential equation (2.39)

$$\widetilde{U}_d\frac{\partial^2\hat{\varphi}}{\partial\Psi_d^2}-\frac{k_z^2}{\widetilde{U}_d}\hat{\varphi}=-\frac{\partial\hat{w}_{\Psi\mathrm{H}}}{\partial\Psi_d}-\frac{ik_z}{\widetilde{U}_d}\hat{w}_{z\mathrm{H}},$$

whose the semi-analytical solution is given by (2.51)

$$\hat{\varphi} = \frac{\widetilde{U}_d H(\bar{\Phi}_d)}{k_\Psi^2 \widetilde{U}_d^2 + k_z^2} e^{ik_\Psi \Psi_d},$$

where

$$H(\bar{\Phi}_d) = e^{-\kappa_2^2(\bar{\Phi}_d - \bar{\Phi}_{d0})} \left[ik_\Psi \left(\hat{u}_\Psi^\infty + \int_{\bar{\Phi}_{d0}}^{\bar{\Phi}_d} \mathrm{RHS}(\chi,\tau) e^{\kappa_2^2 \tau} \mathrm{d}\tau \right) \exp\left(- \int_{\bar{\Phi}_{d0}}^{\bar{\Phi}_d} f_\Psi \mathrm{d}\bar{\Phi}_d \right) \right] +$$
$$e^{-\kappa_2^2(\bar{\Phi}_d - \bar{\Phi}_{d0})} \left[\frac{ik_z \hat{w}_z^\infty}{\widetilde{U}_d} \exp\left(- \int_{\bar{\Phi}_{d0}}^{\bar{\Phi}_d} f_z \mathrm{d}\bar{\Phi}_d \right) \right].$$

The perturbation pressure $\hat{p}$ is an explicit function of the potential given by (2.41)

$$\hat{p} = k_\Phi \left(i\widetilde{U}_d \hat{\varphi} - \widetilde{U}_d^3 \frac{\partial \hat{\varphi}}{\partial \bar{\Phi}_d} - \hat{\varphi} \widetilde{U}_d^2 \frac{\partial \widetilde{U}_d}{\partial \bar{\Phi}_d} + \frac{\widetilde{U}_d^3}{R k_\Phi} \frac{\partial^2 \hat{\varphi}}{\partial \Psi_d^2} - \widetilde{U}_d \frac{k_z^2}{R k_\Phi} \hat{\varphi} \right).$$

2.5.4 Inner perturbation flow

The equations for the inner perturbation flow are the boundary region equations (2.56)-(2.59)

Continuity:

$$\frac{\partial \bar{u}}{\partial \bar{\Phi}} - \frac{\eta}{2\bar{\Phi}} \frac{\partial \bar{u}}{\partial \eta} + \frac{\partial \bar{v}}{\partial \eta} + \frac{\bar{w}}{\widetilde{U}} = 0,$$

Φ-momentum:

$$- \frac{i\bar{u}}{\widetilde{U}^2} + \left[\widetilde{U}_b (F' - 1) + \widetilde{U}_d \right] \frac{\partial \bar{u}}{\partial \bar{\Phi}} - \frac{\eta}{2\bar{\Phi}} \left[\widetilde{U}_b (F' - 1) + \widetilde{U}_d \right] \frac{\partial \bar{u}}{\partial \eta} +$$
$$\frac{\partial}{\partial \bar{\Phi}} \left[\widetilde{U}_b (F' - 1) + \widetilde{U}_d \right] \bar{u} - \frac{\eta}{2\bar{\Phi}} F'' \bar{u} +$$
$$\widetilde{U}_b \left(\frac{\eta F'}{\sqrt{2\bar{\Phi}}} - \sqrt{2\bar{\Phi}} \frac{\partial F}{\partial \bar{\Phi}} - \frac{F}{\sqrt{2\bar{\Phi}}} - \frac{\partial}{\partial \bar{\Phi}} (\beta(\Phi) \sqrt{2\bar{\Phi}}) \right) \frac{1}{\sqrt{2\bar{\Phi}}} \frac{\partial \bar{u}}{\partial \eta} +$$
$$\widetilde{V}_d \sqrt{\frac{k_\Phi R}{2\bar{\Phi}}} \frac{\partial \bar{u}}{\partial \eta} + F'' \bar{v} + 2 \left[\widetilde{U}_b (F' - 1) + \widetilde{U}_d \right] \frac{\partial \widetilde{U}}{\partial \bar{\Phi}} \frac{\bar{u}}{\widetilde{U}} = \frac{1}{2\bar{\Phi}} \frac{\partial^2 \bar{u}}{\partial \eta^2} - \frac{\kappa^2}{\widetilde{U}^2} \bar{u},$$

Ψ-momentum:

$$-\frac{i\bar{v}}{\widetilde{U}^2}+\left[\widetilde{U}_b(F'-1)+\widetilde{U}_d\right]\frac{\bar{v}}{2\bar{\Phi}}+\left[\widetilde{U}_b(F'-1)+\widetilde{U}_d\right]\frac{\partial\bar{v}}{\partial\bar{\Phi}}-$$
$$\frac{\eta}{2\bar{\Phi}}\left[\widetilde{U}_b(F'-1)+\widetilde{U}_d\right]\frac{\partial\bar{v}}{\partial\eta}+$$
$$\sqrt{\frac{Rk_\Phi}{2\bar{\Phi}}}\frac{\partial}{\partial\bar{\Phi}}\left[\frac{\widetilde{U}_b}{\sqrt{Rk_\Phi}}\left(\frac{\eta F'}{\sqrt{2\bar{\Phi}}}-\sqrt{2\bar{\Phi}}\frac{\partial F}{\partial\bar{\Phi}}-\frac{F}{\sqrt{2\bar{\Phi}}}-\frac{\partial}{\partial\bar{\Phi}}(\beta(\Phi)\sqrt{2\bar{\Phi}})\right)+\widetilde{V}_d\right]\bar{u}-$$
$$\frac{\eta}{2\bar{\Phi}}\sqrt{\frac{Rk_\Phi}{2\bar{\Phi}}}\frac{\partial}{\partial\eta}\left[\frac{\widetilde{U}_b}{\sqrt{Rk_\Phi}}\left(\frac{\eta F'}{\sqrt{2\bar{\Phi}}}-\sqrt{2\bar{\Phi}}\frac{\partial F}{\partial\bar{\Phi}}-\frac{F}{\sqrt{2\bar{\Phi}}}-\frac{\partial}{\partial\bar{\Phi}}(\beta(\Phi)\sqrt{2\bar{\Phi}})\right)+\widetilde{V}_d\right]\bar{u}+$$
$$\left[\frac{\widetilde{U}_b}{\sqrt{Rk_\Phi}}\left(\frac{\eta F'}{\sqrt{2\bar{\Phi}}}-\sqrt{2\bar{\Phi}}\frac{\partial F}{\partial\bar{\Phi}}-\frac{F}{\sqrt{2\bar{\Phi}}}-\frac{\partial}{\partial\bar{\Phi}}(\beta(\Phi)\sqrt{2\bar{\Phi}})\right)+\widetilde{V}_d\right]\sqrt{\frac{Rk_\Phi}{2\bar{\Phi}}}\frac{\partial\bar{v}}{\partial\eta}+$$
$$\frac{\partial}{\partial\eta}\left[\frac{\widetilde{U}_b}{\sqrt{Rk_\Phi}}\left(\frac{\eta F'}{\sqrt{2\bar{\Phi}}}-\sqrt{2\bar{\Phi}}\frac{\partial F}{\partial\bar{\Phi}}-\frac{F}{\sqrt{2\bar{\Phi}}}-\frac{\partial}{\partial\bar{\Phi}}(\beta(\Phi)\sqrt{2\bar{\Phi}})\right)+\widetilde{V}_d\right]\sqrt{\frac{Rk_\Phi}{2\bar{\Phi}}}\bar{v}+$$
$$\boxed{\frac{2}{\widetilde{U}}\frac{\partial\widetilde{U}}{\partial\bar{\Psi}}\left[\widetilde{U}_b(F'-1)+\widetilde{U}_d\right]\sqrt{\frac{R}{2\bar{\Phi}k_\Phi}}\bar{u}}=-\frac{1}{\widetilde{U}^2}\frac{1}{2\bar{\Phi}}\frac{\partial\bar{p}}{\partial\eta}+\frac{1}{2\bar{\Phi}}\frac{\partial^2\bar{v}}{\partial\eta^2}-\frac{\kappa^2}{\widetilde{U}^2}\bar{v}-$$
$$\frac{2}{\widetilde{U}}\frac{\partial\widetilde{U}}{\partial\bar{\Phi}}\frac{1}{2\bar{\Phi}}\frac{\partial\bar{u}}{\partial\eta},$$

z-momentum:

$$-\frac{i\bar{w}}{\widetilde{U}^2}+\left[\widetilde{U}_b(F'-1)+\widetilde{U}_d\right]\left(\frac{\partial\bar{w}}{\partial\bar{\Phi}}-\frac{\eta}{2\bar{\Phi}}\frac{\partial\bar{w}}{\partial\eta}\right)+$$
$$\widetilde{U}_b\left(\frac{\eta F'}{\sqrt{2\bar{\Phi}}}-\sqrt{2\bar{\Phi}}\frac{\partial F}{\partial\bar{\Phi}}-\frac{F}{\sqrt{2\bar{\Phi}}}-\frac{\partial}{\partial\bar{\Phi}}(\beta(\Phi)\sqrt{2\bar{\Phi}})\right)\frac{1}{\sqrt{2\bar{\Phi}}}\frac{\partial\bar{w}}{\partial\eta}+\widetilde{V}_d\sqrt{\frac{k_\Phi R}{2\bar{\Phi}}}\frac{\partial\bar{w}}{\partial\eta}+$$
$$\left[\widetilde{U}_b(F'-1)+\widetilde{U}_d\right]\frac{1}{\widetilde{U}}\frac{\partial\widetilde{U}}{\partial\bar{\Phi}}\bar{w}=\frac{1}{\widetilde{U}^3}\kappa^2\bar{p}+\frac{1}{2\bar{\Phi}}\frac{\partial^2\bar{w}}{\partial\eta^2}-\frac{\kappa^2}{\widetilde{U}^2}\bar{w},$$

solved numerically subjected to the boundary conditions (2.60)-(2.64)

$$\bar{u}=\bar{v}=\bar{w}=0,\qquad\text{at}\quad\eta=0,$$

$$\bar{u}\to-\frac{ik_\Phi}{k_z}\hat{w}_\Phi\qquad\text{as}\quad\eta\to\infty,$$

$$\bar{v}\to-i\frac{\hat{w}_\Psi}{\kappa\sqrt{2\bar{\Phi}}}\qquad\text{as}\quad\eta\to\infty,$$

$$\bar{w}\to\hat{w}_z\qquad\text{as}\quad\eta\to\infty,$$

$$\bar{p}\to-i\frac{\sqrt{Rk_\Phi}}{\kappa}\hat{\hat{p}}\qquad\text{as}\quad\eta\to\infty.$$

Equations (2.56)-(2.59) need an initial condition, found by solving numerically the system of ordinary differential equations (2.86)-(2.89)

$$U_0 + V_0' + W_0 = 0,$$

$$-iU_0 + 2\bar{U}_{\text{НМ}}U_0 + \frac{A}{k_\Phi}\bar{V}_{\text{НМ}}U_0' + V_0\bar{U}_{\text{НМ}}' = \frac{A^2}{Rk_\Phi}U_0'' - \kappa^2 U_0,$$

$$-\frac{i}{A}V_0 + \frac{\bar{V}_{\text{НМ}}}{k_\Phi}V_0' + \frac{V_0}{k_\Phi}\bar{V}_{\text{НМ}}' = -\frac{\kappa}{k_z}\frac{A}{\sqrt{Rk_\Phi}}P_0' + \frac{A}{Rk_\Phi}V_0'' - \frac{\kappa^2}{A}V_0,$$

$$-iW_0 + \frac{A}{k_\Phi}\bar{V}_{\text{НМ}}W_0' = \kappa^2 P_0 + \frac{A^2}{Rk_\Phi}W_0'' - \kappa^2 W_0,$$

with the boundary conditions (2.90)-(2.94)

$$U_0 = V_0 = W_0 = 0,$$

$$U_0 \to 0 \qquad \text{when} \qquad \eta_{\text{Н}} \gg 1,$$

$$V_0' \to -\hat{w}_z \qquad \text{when} \qquad \eta_{\text{Н}} \gg 1,$$

$$W_0 \to \hat{w}_z \qquad \text{when} \qquad \eta_{\text{Н}} \gg 1,$$

$$P_0 \to \hat{\hat{p}} \qquad \text{when} \qquad \eta_{\text{Н}} \gg 1.$$

3. NUMERICAL RESULTS

3.1 Numerical procedure

In this section the numerical procedures used to solve the equations are illustrated. The Newton-Raphson algorithm is employed to invert the relationships (2.10)-(2.11) in order to find the potential and streamfunction as functions of r and θ. Block elimination method is used to solve the system (2.86)-(2.87), the Newton's method is employed to solve the nonlinear equation (2.25) and the boundary region equations (2.56)-(2.59) are solved with the block elimination method.

3.1.1 Newton-Raphson algorithm

The Newton-Raphson algorithm is an iterative method used to find the approximated solution of nonlinear systems of equations. The procedure consists in guessing an initial solution and using it to find a better approximation of the solution until convergence. Assuming that we are looking for the solution (x_0, y_0) to the nonlinear system

$$\begin{cases} f_1(x, y) = 0, \\ f_2(x, y) = 0. \end{cases} \tag{3.1}$$

The solution at the iteration $n + 1$ is given by

$$\mathbf{x}_{n+1} = \mathbf{x}_n - \mathbf{J}^{-1}(x_n)\mathbf{F}(x_n),$$

where $\mathbf{x}$ is the vector of the solution, $\mathbf{F} = (f_1, f_2)^T$ is the vector of the equations and $\mathbf{J}$ is the Jacobian of the system (3.1) defined as

$$\mathbf{J} = \begin{bmatrix} \frac{\partial f_1}{\partial x} & \frac{\partial f_1}{\partial y} \\ \frac{\partial f_2}{\partial x} & \frac{\partial f_2}{\partial y} \end{bmatrix}. \tag{3.2}$$

Since the solution at the iteration $n+1$ is found by using the inverse of the Jacobian, it must be invertible, therefore its determinant cannot be null. The Newton-Raphson algorithm has a quadratic convergence and the only restriction is that the initial guess must be close enough to the solution.

We want to find r-θ as functions of Φ_{L}-Ψ_{L} because the latter are the independent coordinates, therefore we want to have the velocity field for each Φ_{L}-Ψ_{L} given. In our case the nonlinear system is given by the potential and streamfunction as functions of r-θ

$$\Psi_{\mathrm{L}} = r\sin\theta + \frac{\Lambda\theta}{2\pi} - \frac{\Lambda}{2},$$

$$\Phi_{\mathrm{L}} = r\cos\theta + \frac{\Lambda}{2\pi}\ln r - \frac{\Lambda}{2\pi}\left[\ln\left(\frac{\Lambda}{2\pi}\right) - 1\right].$$

For a specific point Φ_{L0}-Ψ_{L0}, the nonlinear system is given by

$$a(r,\theta) = \Psi_{L0} - r\sin\theta - \frac{\Lambda\theta}{2\pi} + \frac{\Lambda}{2},$$

$$b(r,\theta) = \Phi_{L0} - r\cos\theta - \frac{\Lambda}{2\pi}\ln r + \frac{\Lambda}{2\pi}\left[\ln\left(\frac{\Lambda}{2\pi}\right) - 1\right],$$

and we require that at the $(n+1)^{th}$ iteration $a = 0$ and $b = 0$. In this case

$$F = \begin{pmatrix} a \\ b \end{pmatrix},$$

$$\mathbf{J} = \begin{pmatrix} \frac{\partial a}{\partial r} & \frac{\partial a}{\partial \theta} \\ \frac{\partial b}{\partial r} & \frac{\partial a}{\partial \theta} \end{pmatrix}.$$

At the stagnation point, where $\Phi_{\mathrm{L}} = 0$ and $\Psi_{\mathrm{L}} = 0$, we know that $\theta = \pi$ and $r = \Lambda/(2\pi)$. Therefore the solution of the system is known at the stagnation point and it can be used as initial guess. Part of the algorithm is shown in Appendix D. The routine takes Φ_{L0},Ψ_{L0} and it gives the corresponding r-θ. Suppose that we want to evaluate r and θ at Φ_{L4} and Ψ_{L1} shown in figure 3.1, the initial guess is the stagnation point where the solution is known, then we move along the streamline $\Psi_{\mathrm{L}} = 0$, namely along the body and find the solution for Φ_{L1} in order to use it as initial guess for the next point. The same line of reasoning is used by moving away from the body, at fixed Φ_{L}, until the desired point Φ_{L4}-Ψ_{L1} is reached. The index *opt* is used to optimize the code. In fact, in the codes used to solve the inner mean flow and the perturbation flow, a marching procedure along the streamwise coordinate Φ is employed. Therefore, every time that we move downstream and call the function to obtain the outer mean flow at the specific point, we do not want to always start form the stagnation point, because this would require much more time. The index *opt* is used for this purpose. It can be set as 0 or 1. If *opt*= 0 the initial guess for the Newton-Raphson method in the routine is the stagnation point. If *opt*= 1 the initial guess is set as the previous value, because the solution of the nonlinear system is close to that value, since the iteration step is small.

Fig. 3.1: Newton-raphson procedure.

3.1.2 Initial condition equations: block elimination method

Equations (2.86)-(2.89) are solved by employing the block elimination method described in Cebeci (2002) on pages 260-264. The 7th-order system of 4 equations is reduced to a system of 7 first-order equations by introducing the new variables $U_1 = U_0'$, $V_1 = V_0'$ and $W_1 = W_0'$

$$\begin{cases} C_1 U_0 + C_2 V_0' + C_3 W_0 = 0, \\ A_1 U_1 + A_2 U_0' = 0, \\ X_1 U_0 + X_2 U_0' + X_3 U_1' + X_4 V_0 = 0, \\ B_1 V_1 + B_2 V_0' = 0, \\ Y_1 V_0 + Y_2 V_0' + Y_3 V_1' + Y_4 P_0' = 0, \\ D_1 W_1 + D_2 W_0' = 0, \\ Z_1 W_0 + Z_2 W_0' + Z_3 W_1' + Z_4 P_0 = 0, \end{cases} \tag{3.3}$$

where

$$C_1 = 1, \quad C_2 = 1, \quad C_3 = 1,$$

$$A_1 = 1, \quad A_2 = -1,$$

$$X_1 = -i + 2\bar{U}_{\text{НМ}} + \kappa^2, \quad X_2 = A\frac{\bar{V}_{\text{НМ}}}{k_\Phi}, \quad X_3 = -\frac{A^2}{Rk_\Phi}, \quad X_4 = \bar{U}'_{\text{НМ}},$$

$$B_1 = 1, \quad B_2 = -1,$$

$$Y_1 = -\frac{i}{A} + \frac{\bar{V}'_{\text{НМ}}}{k_\Phi} + \frac{\kappa^2}{A}, \quad Y_2 = \frac{\bar{V}_{\text{НМ}}}{k_\Phi}, \quad Y_3 = -\frac{1}{Rk_\Phi}, \quad Y_4 = -\frac{i\kappa A}{ik_z\sqrt{Rk_\Phi}},$$

$$D_1 = 1, \quad D_2 = -1,$$

$$Z_1 = -i + \kappa^2, \quad Z_2 = A\frac{\bar{V}_{\text{НМ}}}{k_\Phi}, \quad Z_3 = \frac{A^2}{Rk_\Phi}, \quad Z_4 = -\kappa^2.$$

The ordinary differential equations in the system (3.3) are discretized around the point $\Phi_n, \eta_{j-1/2}$ in figure 3.2. Since they are linear, the system can be written in a block tridiagonal matrix-vector form

$$\begin{pmatrix} A_0 & C_0 & \\ B_j & A_j & C_j \\ & B_{N-1} & A_{N-1} \end{pmatrix} \begin{pmatrix} \delta_0 \\ \delta_j \\ \delta_{N-1} \end{pmatrix} = \begin{pmatrix} r_0 \\ r_j \\ r_{N-1} \end{pmatrix},$$

where A,B, C are the 7×7 matrices of coefficients, δ is the vector of the unknown variables at the j^{th} point and r is the vector of the right hand side. At $j = 0$ and $j = N - 1$ we have the boundary conditions, which are the no-slip condition at the wall for the three velocity components and the matching with the outer perturbation flow at large η. The solution is obtained by the block elimination method which consists of two sweeps, one *forward* and one *backward*. At each step j the unknown functions are computed from recursion formulas.

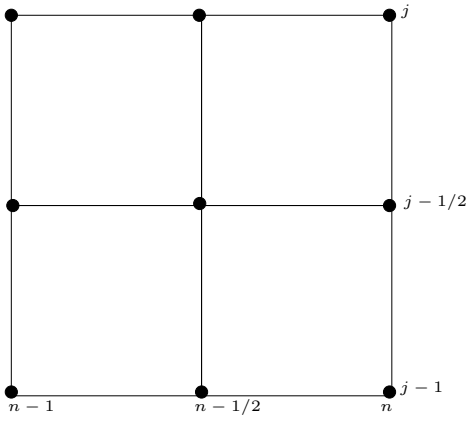

Fig. 3.2: Grid used to compute the the initial conditions and the inner mean flow.

3.1.3 Inner mean flow equation: Newton's method

Equation (2.25) is a nonlinear partial differential equation. Its solution is computed by employing the Keller's Box method. We write the equation and the boundary conditions as a first-order system by introducing new dependent variables $F_1 = F'$ and $F_2 = F_1'$

$$\begin{cases} F_1 = F', \\ F_2 = F_1', \\ F_2' + FF_2 + 2m(1 - F_1^2) = 2\Phi_{\mathrm{L}} \left(F_1 \dfrac{\partial F_1}{\partial \Phi_{\mathrm{L}}} - F_2 \dfrac{\partial F}{\partial \Phi_{\mathrm{L}}} \right), \end{cases} \tag{3.4}$$

$$F(\Phi_{\mathrm{L}}, 0) = 0, \qquad F_1(\Phi_{\mathrm{L}}, 0) = 0, \qquad F_1(\Phi_{\mathrm{L}}, \infty) = 1. \tag{3.5}$$

The grid used for the computation is shown in figure 3.2. The first two equations of (3.4) are discretized around the point $\Phi_n, \eta_{j-1/2}$ while the third equation of (3.4) is discretized around the point $\Phi_{n-1/2}, \eta_{j-1/2}$. We assume that F_j^{n-1}, F_{1j}^{n-1} and F_{2j}^{n-1} are known so that, given an initial condition, a marching procedure along Φ can be used to solve the equation at every streamwise position. Since we have the solution of the Hiemenz equation (2.28), we can use that as the initial condition. The system (3.4) is solved using Newton's Method at every streamwise position. The iterates $F_j^{(i)}$, $F_{1j}^{(i)}$, $F_{2j}^{(i)}$ are introduced and their initial guess is set as the solution at Φ_{n-1}. We write

$$F^{(i+1)} = F^{(i)} + \delta F^{(i)}, \tag{3.6a}$$

$$F_1^{(i+1)} = F_1^{(i)} + \delta F_1^{(i)}, \tag{3.6b}$$

$$F_2^{(i+1)} = F_2^{(i)} + \delta F_2^{(i)}, \tag{3.6c}$$

and substitute (3.6) in the system (3.4). The system is linearized by neglecting terms of order $(\delta F^{(i)})^2$, $(\delta F_1^{(i)})^2$, $(\delta F_2^{(i)})^2$ and it is solved at each iteration by using the block-elimination method (Cebeci (2002)). Once $\delta F^{(i)}$, $\delta F_1^{(i)}$ and $\delta F_2^{(i)}$ are null the iterative procedure is interrupted.

3.1.4 Boundary region equations

In order to solve the boundary region equations a marching procedure along $\bar{\Phi}$ is used. The method is based on second-order central differences in η and backward

differences in $\bar{\Phi}$. The grid used to compute the pressure is staggered compared to the grid used for the velocity components as shown in Figure 3.3.

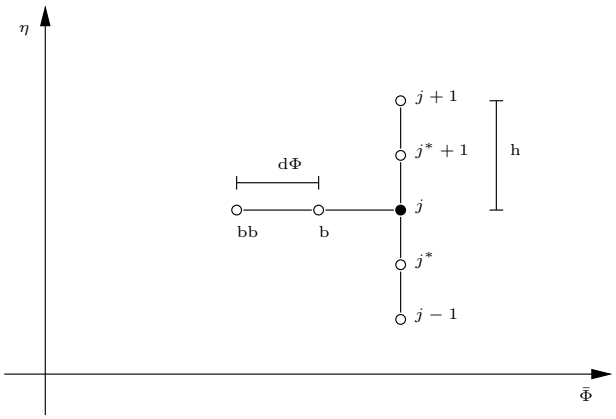

Fig. 3.3: Grid used to compute the velocity components and pressure.

With the second-order central differences method a function f and its first and second derivatives are approximated as follows

$$f = f_j, \tag{3.7}$$

$$\frac{\partial f}{\partial \eta} = \frac{f_{j+1} - f_{j-1}}{2h}, \tag{3.8}$$

$$\frac{\partial^2 f}{\partial \eta^2} = \frac{f_{j+1} - 2f_j + f_{j-1}}{h^2}. \tag{3.9}$$

With the second-order backward differences method the first derivative of a function f is given by

$$\frac{\partial f}{\partial \bar{\Phi}} = \frac{af_j + bf_{bj} + cf_{bbj}}{\mathrm{d}\Phi}, \tag{3.10}$$

where a, b and c are assigned values.

The grid of pressure is staggered, therefore the value of the pressure and its derivative with respect to η have been expressed in terms of the staggered index, namely

$$\bar{p} = \frac{\bar{p}_{j^*+1} + \bar{p_{j^*}}}{2}, \tag{3.11}$$

$$\frac{\partial \bar{p}}{\partial \eta} = \frac{\bar{p}_{j^*+1} - \bar{p}_{j^*}}{h}, \tag{3.12}$$

as can be easily seen in Figure 3.3.

The index j goes from 0 to $N-1$, thus the boundary conditions are

$$\bar{u}_{j=0} = \bar{v}_{j=0} = \bar{w}_{j=0} = 0, \tag{3.13}$$

$$\bar{u}_{j=N-1} = 0, \tag{3.14}$$

$$\bar{v}_{j=N-1} = -i\frac{\hat{w}_\Psi(j, N-1)}{\kappa\sqrt{2\bar{\Phi}}}, \tag{3.15}$$

$$\bar{w}_{j=N-1} = \hat{w}_z(j, N-1), \tag{3.16}$$

$$\bar{p}_{j=N-1} = -i\frac{\sqrt{Rk_\Phi}}{\kappa}\hat{\bar{p}}(j, N-1). \tag{3.17}$$

The linear system of the discretized equations can be written in the form of a block tridiagonal matrix-vector and it is solved by the block elimination method as described on page 263-264 in Cebeci (2002).

3.2 Previous numerical results

In this section some of the numerical results of Leib *et al.* (1999) are shown. They are relevant to make a comparison with the results obtained for the Rankine body.

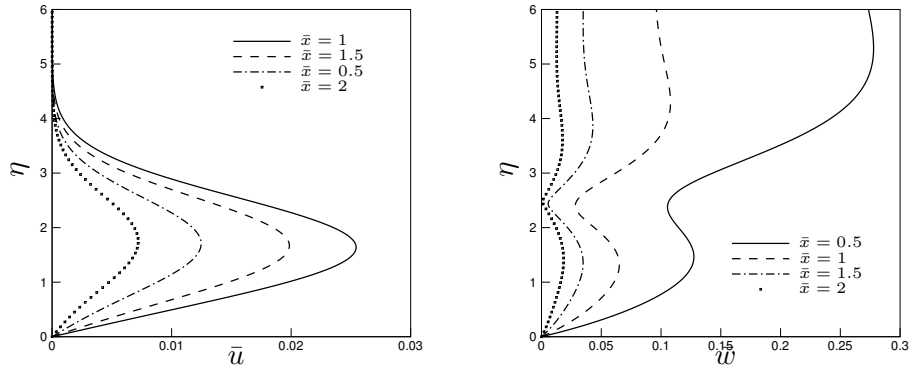

Fig. 3.4: Profile of the streamwise (left) and spanwise (right) perturbation velocities at the indicated values of $\bar{x}$.

Figures 3.4 and 3.5 have been obtained by numerically solving the boundary region equations in Leib *et al.* (1999). They exactly reproduce the results shown in their paper, giving a further confirmation that the algorithms used to solve the equations for the Rankine body work. Figures 3.4 show the profiles of the amplitudes streamwise and spanwise velocity at different values of the streamwise variable $\bar{x}$ (η is normal variable). It is seen that the maximum value of the streamwise velocity increases initially with $\bar{x}$ and then it quickly decreases to zero. This can better be seen in figure 3.5 where the amplitude of the streamwise velocity is plotted in $\bar{x}$ at the fixed value of η where the peaks occur. The spanwise velocity increases with η and it keeps constant, due to the matching conditions.

The results of Leib *et al.* (1999) have been compared to those ones of Choudhari (1996) who studied the interaction of a vortical perturbation transported from the free stream to the flat plate boundary layer. The streamwise velocity profiles look similar to each other while the spanwise velocity profile are quite different. Figure 3.4 was obtained at fixed value of κ and κ_2 which are the scaled transverse wavenumbers. Other computations show that by increasing the value of both κ and κ_2 the peak of the streamwise profiles decrease very quickly to zero

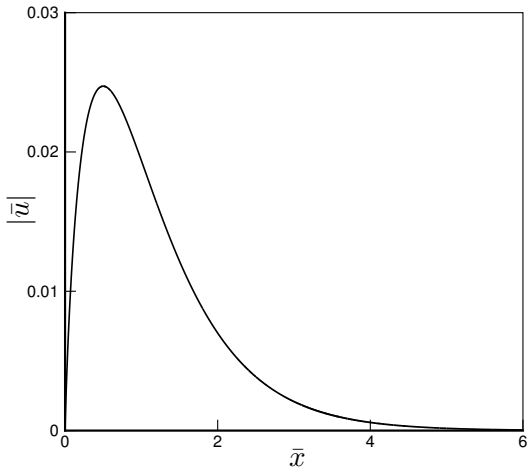

Fig. 3.5: Evolution of the boundary region streamwise velocity perturbation magnitude at $\eta = 1.64$.

after having reached its highest value. Contrarily, the decay is slower.

In the limit case where $\kappa \to \infty$ and $\kappa_2/\kappa = \mathcal{O}(1)$ the steady boundary region equations of Leib *et al.* (1999) have an asymptotic solution. Results show that the steady solution increases linearly with the boundary layer thickness, even if this is not valid near the origin. These results led Bertolotti (1997) to think that Klebanoff modes could be well represented by one single steady mode, while Leib *et al.* (1999) demonstrated that the unsteady low frequency solutions have the dominant effect on the streamwise velocity in the boundary layer. They also showed that for $\kappa \to 0$ the boundary region equations reduce to the steady ones and the solutions overlap. The results of Leib *et al.* (1999) have been presented because the solution of the Rakine-body boundary region equations will be compared with their results in section 3.6.

3.3 Mean flow solution

In this section the results for the mean flow are presented and compared to the analytical expressions presented in Panton (1995). In particular, the pressure coefficient, the boundary layer thickness and the composite mean flow are shown and discussed.

The mean pressure coefficient is defined as

$$C_p = 1 - \widetilde{U}^2.$$

The pressure changes along the body surface because of the curvature and it is studied as a function of s. The behavior of C_p is obtained numerically and shown in figure 3.6. At the stagnation point $C_p = 1$ and since there is symmetry the slope of the curve is zero. Then the fluid accelerates and the pressure decreases until the fluid starts to decelerate and the pressure increases. The same behavior is obtained by Panton (1995) and the two curves perfectly overlap as shown in figure 3.6.

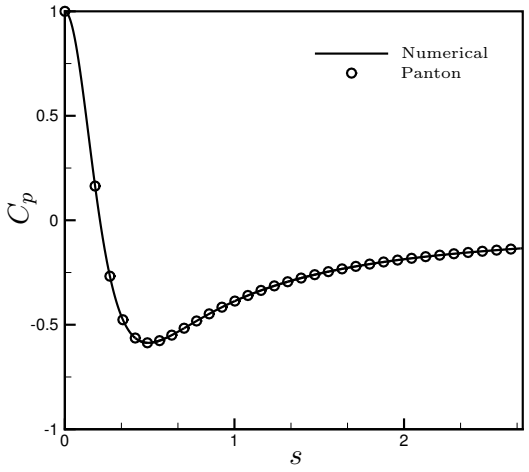

Fig. 3.6: Mean pressure as a function of s along the body.

The boundary layer thickness is the distance from the body to a point where the velocity reaches the free stream velocity value, in particular it is defined as the distance where $u^* = 0.99U^*_\infty$. This distance can be numerically found by the definition of η, which is the inner variable used to find the solution in the viscous boundary layer. In optimal coordinates η is define as

$$\eta = \Psi_{\text{L}} \sqrt{\frac{R_{\text{L}}}{2\Phi_{\text{L}}}}.$$

Once we have obtained the solution of the inner mean flow the value of η where the velocity has the free stream value can be found for every streamwise coordinate Φ_{L} and this value is supposed to be different on the curvature where the solution is not similar. Two important checks can be done analytically and numerically: at the stagnation point and downstream, where the flow is uniform, the boundary layer thickness is well known. In particular at the stagnation point the potential and streamfunction are

$$\Psi_{\text{L}} = \frac{2\pi}{\Lambda} x_{\text{HL}} y_{\text{HL}}, \qquad \Phi_{\text{L}} = \frac{\pi x^2_{\text{HL}}}{\Lambda}.$$

By substituting the two above equations in the definition of η the following is obtained

$$\eta = y_{\text{HL}} \sqrt{\frac{2\pi R_{\text{L}}}{\Lambda}}.$$

Thus the boundary layer thickness for the stagnation point is constant and equal to

$$y_{\text{HL}} = \eta_\delta \sqrt{\frac{\Lambda}{2\pi R_{\text{L}}}},$$

where η_δ is the value of η where the velocity is 0.99 and it is numerically found to be $\eta_\delta = 2.4$. This result is in agreement with Schlichting (1979)

$$\delta^* = 2.4\sqrt{\frac{\nu^*}{a^*}},$$

where $a^* = \alpha U_\infty^*/L^*$, $\alpha = 2\pi/\Lambda$. By substituting the value of a^* in the boundary layer thickness found by Schlichting (1979) it is obtained

$$\delta_{\text{L}} = 2.4\sqrt{\frac{\Lambda}{2\pi R_{\text{L}}}},$$

which is the thickness previously found. The same analytical check can be done downstream where the potential and streamfunction are

$$\Psi_{\text{L}} = y_{\text{L}}, \qquad \Phi_{\text{L}} = x_{\text{L}},$$

and therefore

$$y_{\text{L}} = \eta_\delta\sqrt{\frac{2x_{\text{L}}}{R_{\text{L}}}}.$$

Downstream the boundary layer grows as $x_{\text{L}}^{1/2}$. On the body is not possible to find analytically the boundary layer thickness since the expressions of the potential and streamfunction are more complicated. Therefore, the boundary layer thickness is numerically evaluated and its value is compared to Hiemenz boundary layer at the stagnation point and Blasius boundary layer downstream.

Figure 3.7 shows the composite solution for the total mean flow given by equation (2.32) at $s = 1.48$. In figure 3.8 the profiles of the velocity are shown at different positions on the body. At each position the velocity reaches a different free-stream value, as expected since the outer mean velocity is not constant. The point where the velocity has the free stream value increases following the boundary layer thickness.

The behavior of the boundary layer thickness along the body is shown in figure 3.8. At the stagnation point, the Hiemenz boundary layer is constant because

there is a perfect balance between the wall-normal viscous diffusion, which lets the boundary layer thickness increase and the favourable pressure gradient, which lets the boundary layer thickness decrease. Downstream the pressure gradient effect never overcomes the wall-normal diffusion and eventually wall-normal diffusion takes over completely.

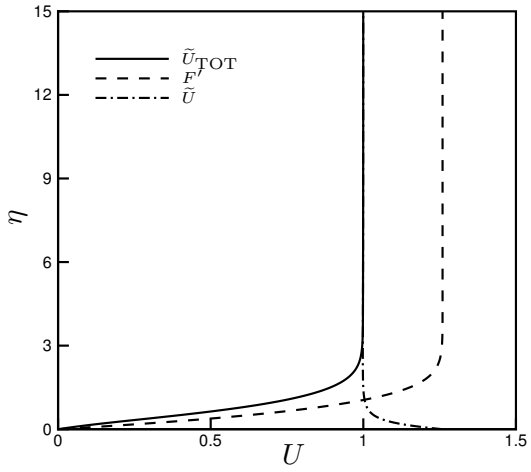

Fig. 3.7: Composite solution of the mean flow at $s = 1.48$

.

3.4 Outer perturbation flow solution

The analytical solution of the outer perturbation flow has been found and it depends on the outer mean flow. The integral in equation (**??**) is evaluated numerically for every streamline, from the position of the grid to a downstream position. Along the streamline $\Psi = 0$, the flow encounters the stagnation point at $\Phi = 0$ where the velocity is null. It is then not possible to evaluate the integral near the stagnation point where the velocity is close to zero because the function to be integrated becomes singular. The first value of the displaced streamline Ψ_d where it is possible to calculate the integral is found numerically. Figure

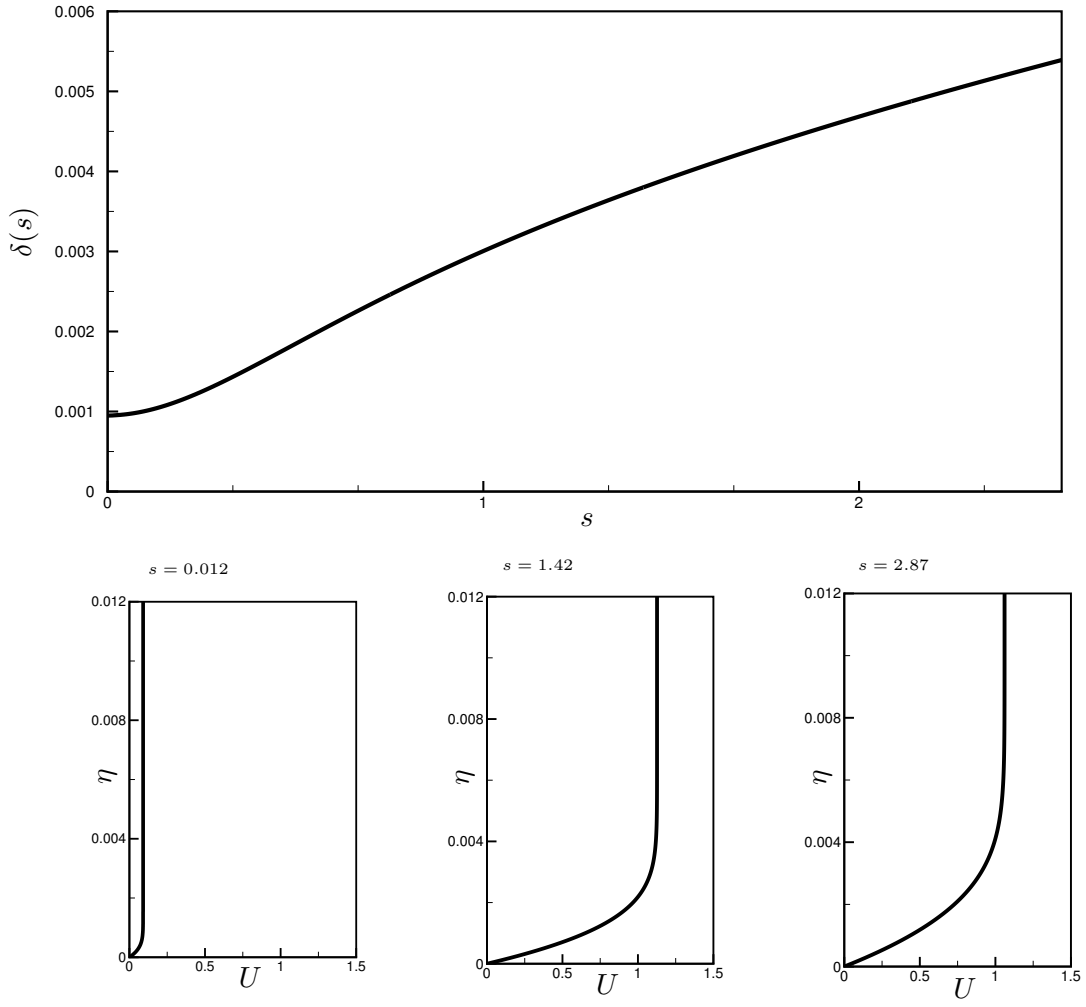

Fig. 3.8: Boundary layer thickness as a function of s (top) and inner mean velocity profiles at different positions on the body (bottom).

3.9 (left) shows the spanwise perturbation velocity at two different streamlines near the body. The other two velocity components are not shown because the behavior is the same as the spanwise velocity component. The velocity decays exponentially as expected. The position of the grid Φ_{d0} is very important for the exponential decay. In fact, if the grid was too far away from the body, the perturbation flow would decay before encountering the body. However, the grid cannot be positioned too close to the stagnation point. Figure 3.9 (right) shows the outer perturbation pressure at different streamlines.

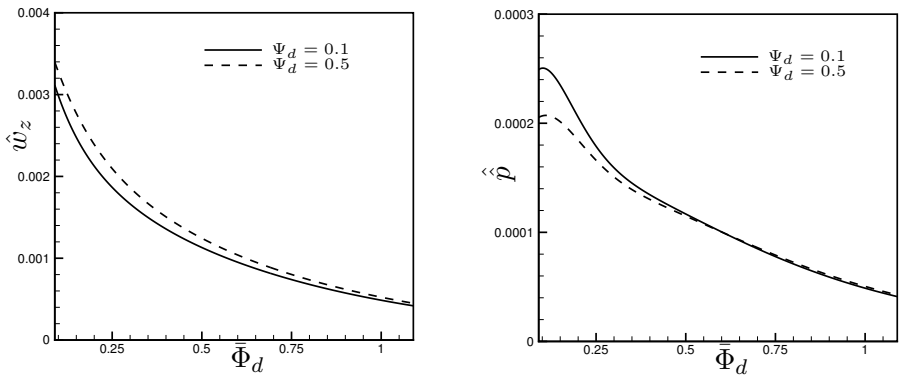

Fig. 3.9: Spanwise outer perturbation velocity (left) and pressure (right) at different streamlines.

Figure 3.10 shows how the outer spanwise perturbation velocity changes by moving the grid. The chosen numerical range is between $\bar{\Phi}_{d0} = -3$ and $\bar{\Phi}_{d0} = -2$. As the analytical solution (2.43) suggests, changing the grid position has an effect on the viscous decay. If the grid was positioned too far from the body, the perturbation flow would decay before reaching the body. In figure 3.10 the spanwise perturbation velocity is shown for three different values of the position of the grid $\bar{\Phi}_{d0}$. The velocity is smaller when the grid is farther.

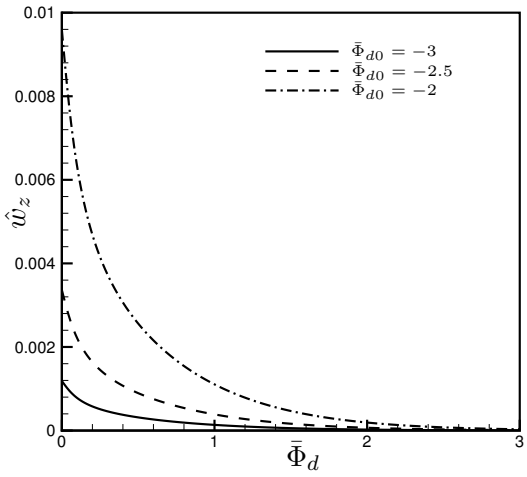

Fig. 3.10: Effect of the grid position on the outer perturbation velocity.

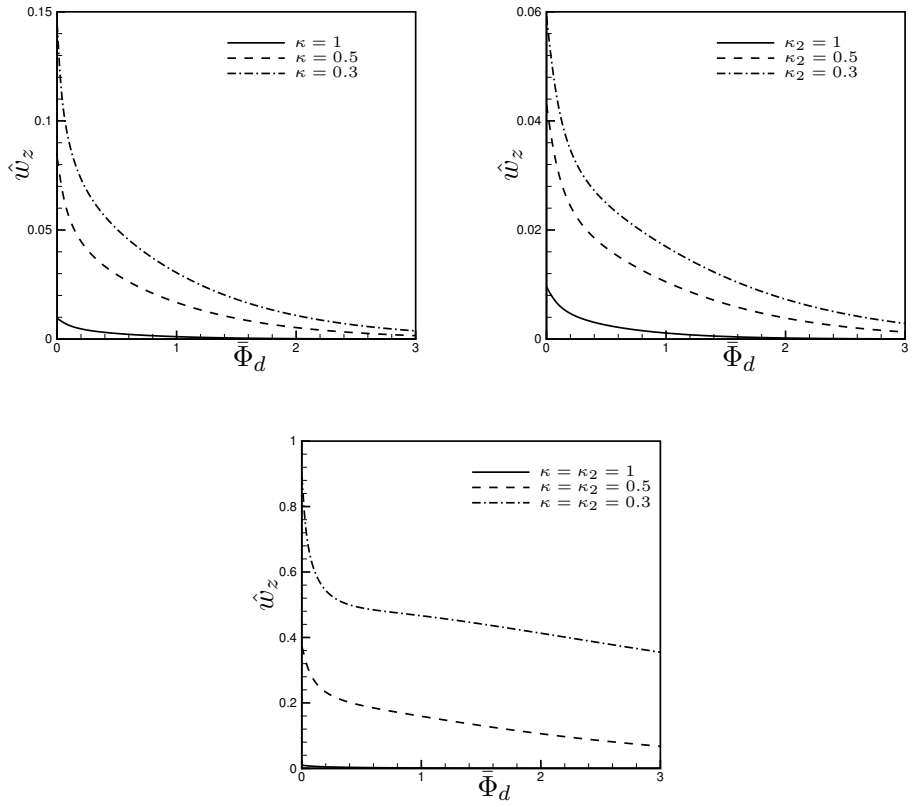

Fig. 3.11: Effect of changing κ and κ_2 on the outer perturbation velocity.

Figure 3.11 shows the effect of changing κ and κ_2 on the outer perturbation spanwise velocity component. Changing these two parameters is interesting to see the role of the viscous effects, because decreasing κ and κ_2 means increasing the Reynolds number. On the top-left figure 3.11 $\kappa_2 = 1$ is kept constant and κ is varied at the three indicated values. In the analytical solution (2.43) it can be seen that the parameter κ is in the integral. Upstream, where the mean flow is uniform, κ only multiplies $\bar{\Phi}_d$, therefore it is responsible for the exponential decay. Decreasing κ lets the velocity have a higher value upstream. However, the contribution of κ is different moving downstream as the mean velocity varies. On the top-right figure 3.11 $\kappa = 1$ is kept constant and κ_2 is varied at the three indicated values. As is clearly evident in the analytical solution (2.43), the only contribution of κ_2 is on the exponential decay, therefore by decreasing the value of κ_2 the velocity decays slower. The bottom figure 3.11 shows the effect of simultaneously changing both κ and κ_2. As expected, since the two parameters have an effect on the exponential decay, by decrasing them, the exponential decay is also decreased.

3.5 Initial conditions solution

Stagnation point coordinates

In this section considerations on coordinates used at the stagnation point are illustrated. The results obtained for the initial conditions cannot be compared with the works in the literature as the approach used in this thesis to find the initial condition is presented herein for the first time. It is interesting to show the relationship between the optimal coordinates and the coordinates used at the stagnation point. In particular, it is worth to see the effect of the Reynolds number on the coordinates. The lines at constant Φ and Ψ in the (x_{H}-η_{H}) plane are shown in figure 3.12 for different Reynolds numbers. It can be observed that

moving along the line at constant Φ, the same value of $\bar{x}_{\mathrm{H}}$ is reached at larger η_{H} by increasing the Reynolds number. This occurs because changing the Reynolds number has an effect on the vertical scale, since the definition of η_{H} contains the Reynolds number. The lines at constant Φ have been obtained numerically with the following steps.

- Φ is fixed to the chosen value and Ψ is varied from a value upstream to a certain value not too downstream because we are interested in the region around the stagnation point.
- For each Ψ and the assigned Φ, the corresponding value of x and y is found numerically by inverting the relationship of the potential and stream function.
- The value of x_{H} and η_{H} is found from the value of the coordinates with origin in source x-y.

The same line of reasoning is used to find the line at constant Ψ. Since η_{H} is y_{H} rescaled with the Reynolds number, the latter has an effect on the curves, as shown in figure 3.12. In particular, by increasing the Reynolds number, the lines at constant Ψ become more perpendicular to the stagnation point.

Another important observation is that when $\eta_{\mathrm{H}} \to \infty$ the optimal coordinate Φ is negative, because the coordinates rotate at the stagnation point, therefore moving away from the stagnation point corresponds to moving upstream. The optimal coordinate Φ is zero at the stagnation point and it becomes negative along the streamline $\Psi = 0$ moving away from the stagnation point. This is shown in figure 3.13, where the coordinate x_{H} is fixed at three different small values and η_{H} is increased. In the (Φ-Ψ) plane it is clear that the more x_{H} is small, the more Φ is immediately negative for positive η_{H}. In other words, for a given x_{H}, by increasing η_{H} the corresponding Φ is negative because we are moving

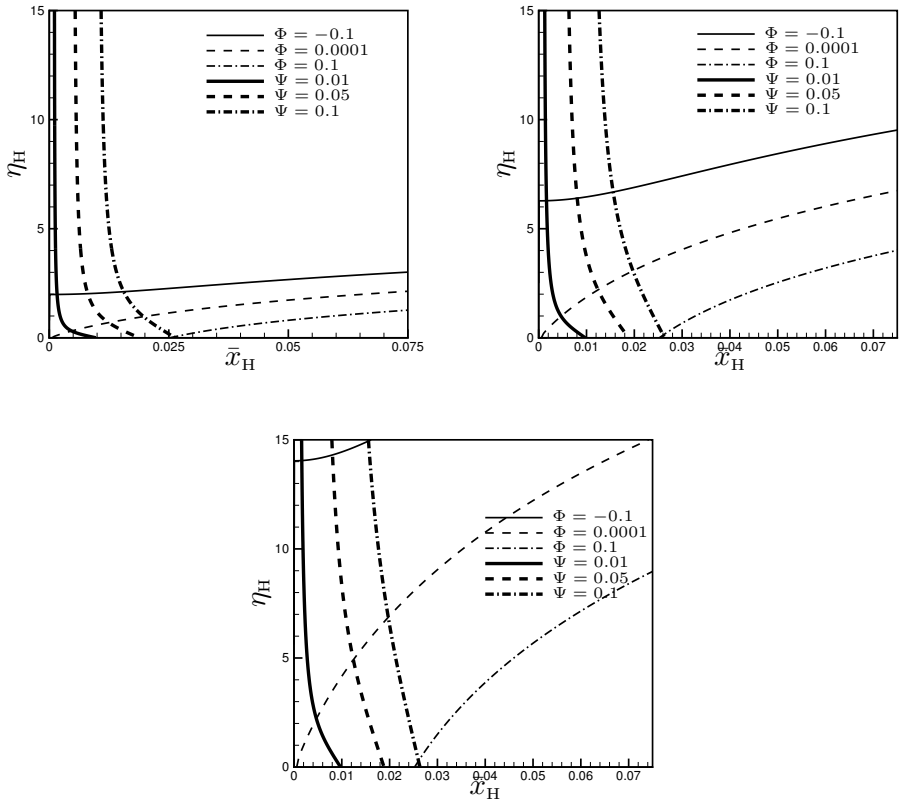

Fig. 3.12: Constant Φ and Ψ lines at $R = 100$ (top left), $R = 1000$ (top right) and $R = 5000$ (bottom) in $x_H - \eta_H$ plane.

upstream. Starting exactly at the stagnation point, namely taking $x_{\mathrm{H}} = 0$, would only give negative Φ, because $\Phi < 0$ upstream, $\Phi = 0$ at the stagnation point and $\Phi > 0$ along the body. The value of the streamline, which play the role of the vertical coordinate, does not change significantly because moving upstream the streamlines are uniform, therefore changing the Reynolds number does not have a big effect. The boundary condition for the initial condition equations is given at negative Φ.

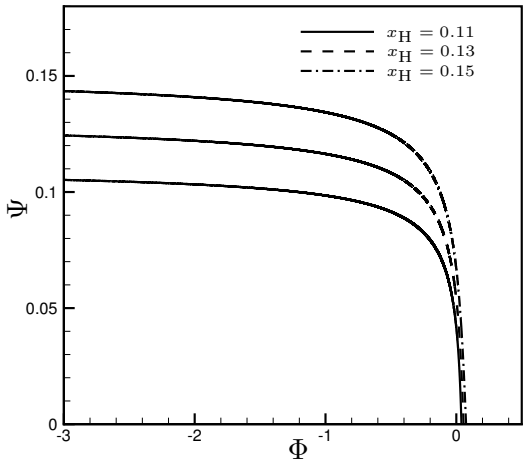

Fig. 3.13: Constant x_{H} lines at $R = 100$.

The optimal coordinates follow the shape of the body, therefore at the stagnation point they are rotated and perfectly coincide with the coordinates used at the stagnation point x_{H}-η_{H}. We used two different coordinates to analyse the flow at the stagnation point and the flow around the Rankine body. It is shown that η used for the boundary region equations and η_{H} used at the stagnation point coincide by taking the limit of small $\bar{\Phi}$, namely approaching the stagnation point. The scaled normal coordinate used in the boundary region equation is

$$\eta = \Psi \sqrt{\frac{Rk_{\Phi}}{2\bar{\Phi}}},$$

which can only be defined for positive Φ. It has been checked numerically (Figure

3.14 top left) that if $\bar{\Phi}$ is small enough, $\bar{x}_{\mathrm{H}}$ remains small even when η is large, because the curvature has no effect yet and η remains orthogonal to the stagnation point, that is to x_{H} which remains small and constant. In this case $\eta = \eta_{\mathrm{H}}$. On the other hand, by increasing the value of $\bar{\Phi}$, $\bar{x}_{\mathrm{H}}$ becomes too large for η large because of the curvature. Figure 3.14 (top right) shows that for small Ψ and $\bar{\Phi}$ the two coordinates η and η_{H} overlap. By increasing the value of $\bar{\Phi}$, namely moving away from the stagnation point, the two normal coordinates are not the same. Figure 3.14 (bottom) shows a further confirmation that η and η_{H} only coincide near the stagnation point. In fact the plot of η versus η_{H} has a slope of 45 degrees only for $\bar{\Phi}$ small enough.

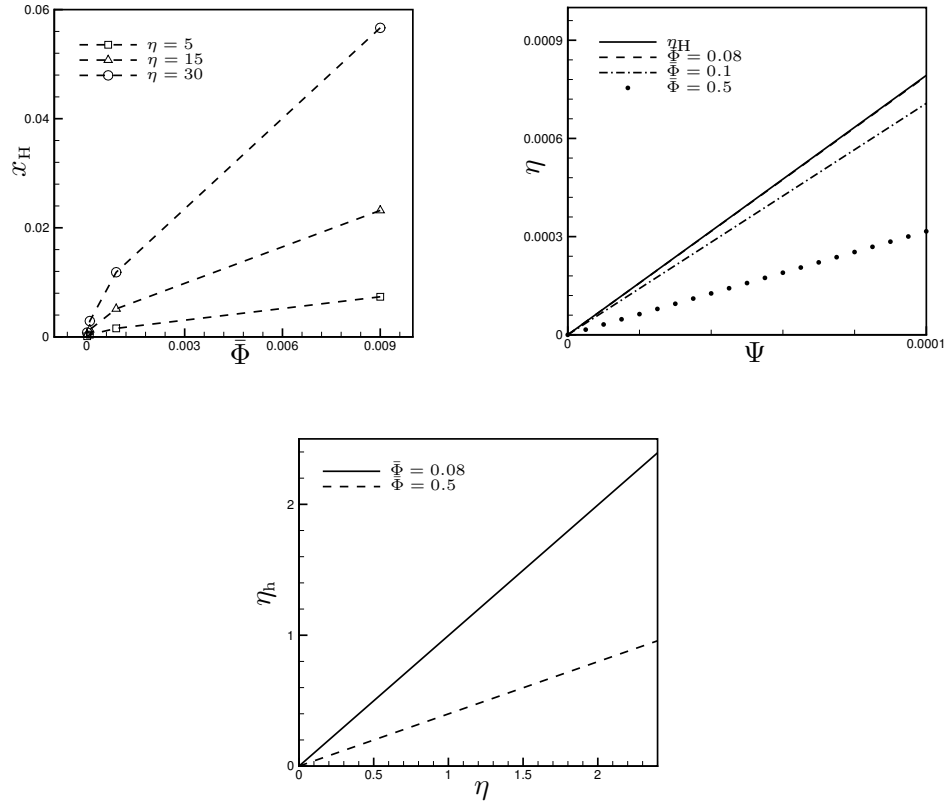

Fig. 3.14: x_{H} as function of $\bar{\Phi}$ at different η (top left), η as a function of Ψ at different $\bar{\Phi}$ (top right) and η_{h} against η at different $\bar{\Phi}$.

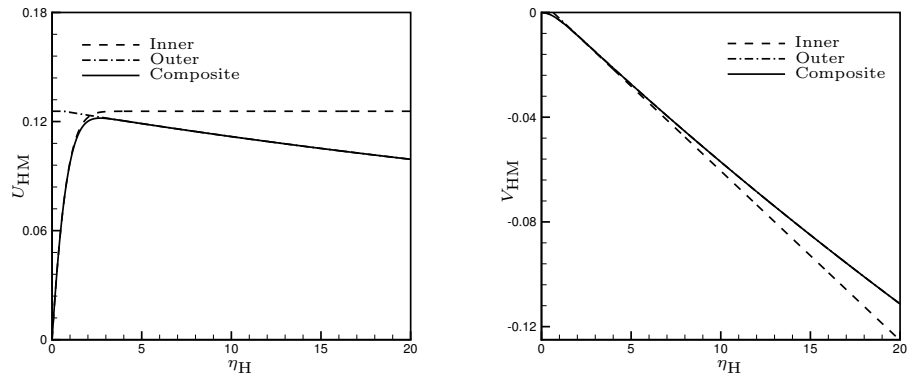

Fig. 3.15: Hiemenz streamwise (left) and normal (right) composite velocity components.

Results of initial condition equations

In this section results of the equations derived in section 2.4.3 are presented. Figure 3.15 shows the streamwise and normal composite velocity components. The composite is equal to the inner velocity inside the boundary layer (for $\eta_H < \beta_H$, where β_H is the Hiemenz displacement thickness) and it is equal to the outer velocity outside the boundary layer. In the limit of η_H very large the velocity will eventually go to 0 (streamwise) and -1 (normal). This is not evident in the figures because η_H would need to be very large to see it, since it happens upstream, far away from the stagnation point.

Figure 3.16 shows the profiles of U_0 (left) and W_0 (right) obtained by solving equations (2.86)-(2.89). The streamwise component is confined within the boundary layer because outside it is of smaller order and the outer boundary condition is set as 0. The spanwise component reaches the value of the outer perturbation velocity at large η_H because it matches the outer solution. Figure 3.17 shows the maximum residual, Res, of the x-momentum equation (2.87) as a function of the number of points N used to find the solution. The plot is in logarithmic scale and the residual decreases linearly by increasing the number of points.

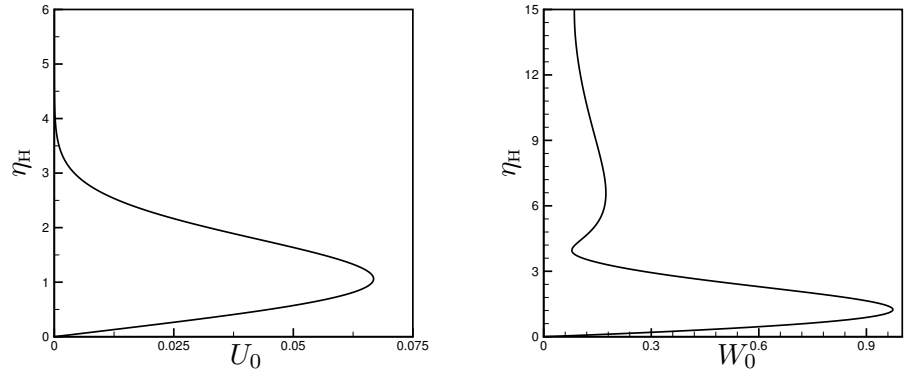

Fig. 3.16: Streamwise (left) and spanwise (right) solution of the system (2.86)-(2.89).

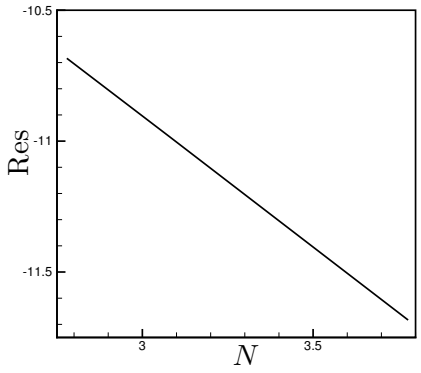

Fig. 3.17: Maximum residual Res of x-momentum equation (2.87) as a function of number of points N in a $\log - \log$ scale.

As explained in section 2.4.3, the solution of the system (2.86)-(2.89) cannot be used as initial condition because the profiles obtained are in coordinates x_H-η_H while the boundary region equations are in optimal coordinates. To find the initial streamwise component, the initial $\bar{\Phi}$ is fixed and for every η the corresponding $\bar{x}_H$ is found and the initial streamwise velocity component is found by multiplying $\bar{x}_H$ by U_0. The initial normal velocity component is found by integrating the continuity equation in optimal coordinates and the initial velocity components obtained are rescaled by the local outer mean flow as the velocities in the bound-

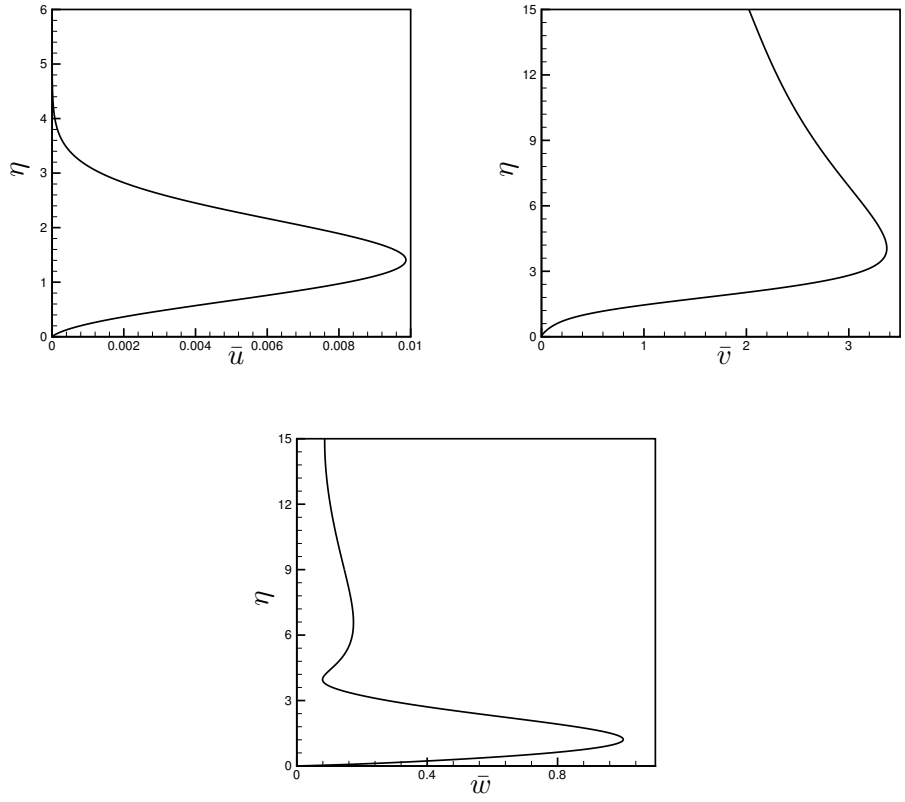

Fig. 3.18: Initial profile of the streamwise (top left), normal (top right) and spanwise (bottom) perturbation velocities.

ary region equations. Figure 3.18 shows the initial value of the streamwise (top left), normal (top right) and spanwise (bottom) velocity components at the initial $\bar{\Phi}$ in optimal coordinates. The velocity components and pressure obtained for the initial profile satisfy the boundary region equation at the initial $\bar{\Phi}$. Figure 3.19 shows the resolution check for the continuity (top left) and momentum equations (top right, bottom left and bottom right) in optimal coordinates at the initial $\bar{\Phi}$ in logarithmic scale. The residual decreases linearly by increasing the number of points N.

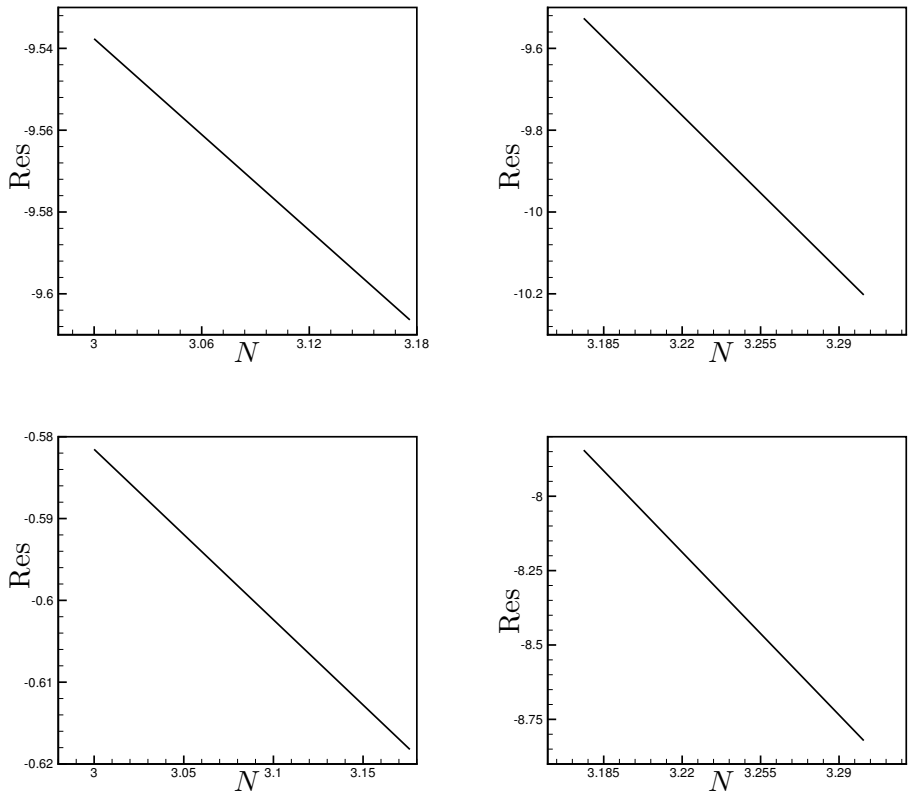

Fig. 3.19: Resolution check for the continuity (top left), Φ-momentum (top right), Ψ-momentum (bottom left) and z-momentum (bottom right) equations at the initial $\bar{\Phi}$ as a function of number of points N in a $\log - \log$ scale.

3.6 Boundary region equations solution

In this section the results of the boundary region equations are illustrated and compared with those of Leib *et al.* (1999) for the flat-plate boundary layer. Figure 3.20 shows the amplitude of the streamwise (top) and spanwise (bottom) velocity components at different values of the streamwise coordinate $\bar{\Phi}$. It is found that, while the dynamic of the streamwise velocity component is the same as the streamwise velocity component of the flat plate, the dynamic of the spanwise velocity component is significantly different from the spanwise velocity component of the flat plate. This is due to the matching requirements which

indicate that the effect of the pressure gradient plays a fundamental role in the outer flow dynamics. The streamwise streaks are initially amplified and then they decay downstream, behavior known as transient growth. The behavior of the spanwise velocity amplitude is due to the free-stream matching requirements. In fact, at a large distance from the body the value is the same as the outer spanwise perturbation velocity component. It decays by moving downstream as shown in figure 3.20 and the free-stream value is also smaller downstream because the outer perturbation flow decays with $\bar{\Phi}$. Figure 3.21 illustrates the contour plot of the streamwise velocity component. It is observed that at large distance from the body the velocity is null and that its maximum value decreases moving downstream.

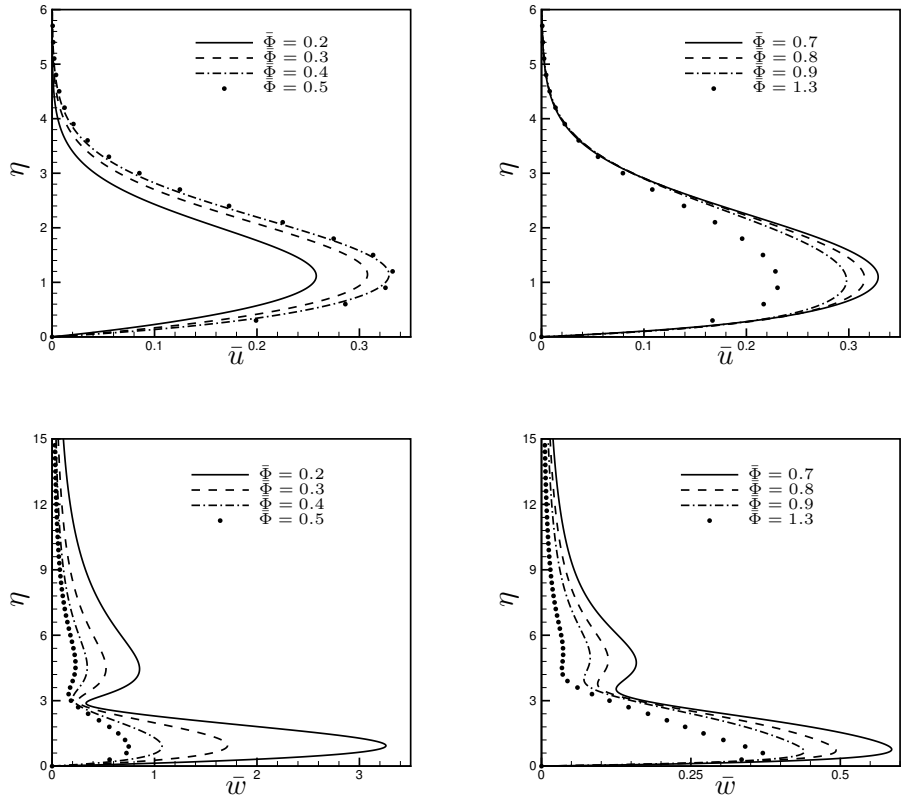

Fig. 3.20: Streamwise (top) and spanwise (bottom) velocity profiles at the indicated values of $\bar{\Phi}$.

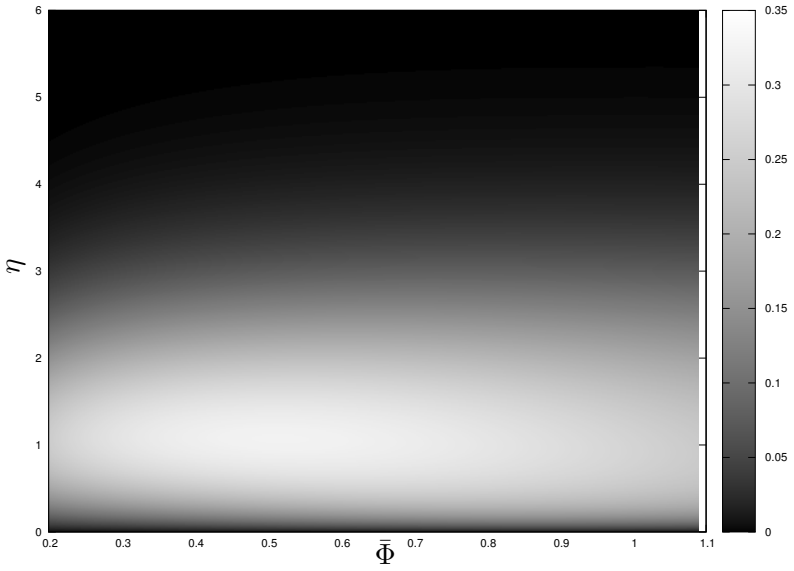

Fig. 3.21: Contour plot of the streamwise velocity component.

The peak of the streamwise velocity component has a different value to the one on the flat-plate boundary layer and it occurs at different η moving along the body. This is due to the curvature and the fact that the inner mean flow is not similar. Figure 3.22 (left) shows the maximum value of $\bar{u}$ at each streamwise location: it increases at the beginning and then decreases moving downstream because the streaks decay. This behavior is similar for the flat-plate boundary layer analysed in Leib *et al.* (1999) because they also considered the linear case. The drawback of such choice is that the streaks decay moving downstream, therefore we cannot obtain an information on the perturbation flow farther downstream. Figure 3.22 (right) shows the η value where the streamwise velocity has its maximum value for every $\bar{\Phi}$. Differently from the flat-plate case the value of η_{MAX} varies along the body, showing the difference of considering a Rankine body, namely variable mean flow, instead of a flat plate, namely a uniform mean flow.

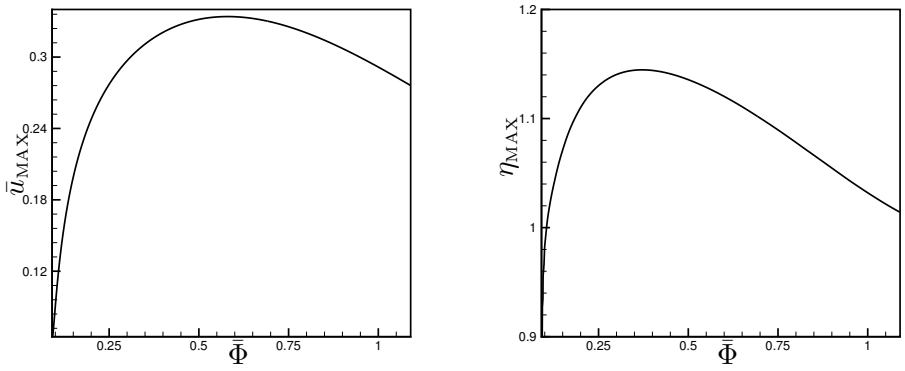

Fig. 3.22: Maximum value of the streamwise velocity component as a function of $\bar{\Phi}$ (left) and the η value where the streamwise velocity component is maximum along $\bar{\Phi}$ (right).

The effect of κ on the solution is interesting. The equations have been obtained considering that $Rk_\Phi = \mathcal{O}(1)$. This assumption follows the experimental observations on the streaks performed on the flat plate. The parameter κ in the boundary region equation must be of order 1 because it is given by

$$\kappa = \frac{k_z}{\sqrt{Rk_\Phi}}.$$

Therefore, as $k_z = 2\pi$ and $Rk_\Phi = \mathcal{O}(1)$, κ must also be of order 1. However its value can be changed to see the effect of the Reynolds number or the effect of the streamwise perturbation wavelength. For the flat plate, in the limit of $\kappa \to 0$ the boundary region equations reduce to the boundary layer equations which are the equations that describe the two dimensional flow inside the boundary layer. This is not the case considered herein, where the leading edge corresponds to the stagnation point where the boundary layer already has a nonzero thickness and the perturbation flow is already three-dimensional. Figure 3.23 (left) shows that, when the ratio between κ and κ_2 is kept constant, for large κ the solution of the boundary region equations coincides with the solution of the steady boundary region equations as in Leib *et al.* (1999). However, for a Rankine body the

boundary region equations do not have an asymptotic solution for large κ, namely the solutions for different κ do not overlap. In the case of Leib *et al.* (1999) the solution for large κ is proportional to the inverse of κ^2 which multiplies a function of $\bar{x}$ and η. Both the solution and the streamwise coordinate scale with κ^2. For a Rankine body, due to the non-similarity of the mean flow, the curves at different values of large κ cannot be rescaled by a constant, as well as the streamwise coordinate as shown in figure 3.23 (right).

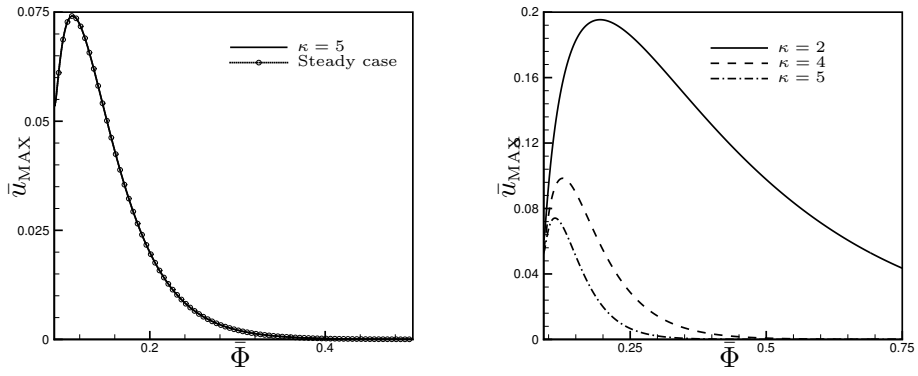

Fig. 3.23: Maximum value of $\bar{u}$ as a function of $\bar{\Phi}$ for $\kappa = 5$ compared to the steady solution of the boundary region equations (left) and maximum value of $\bar{u}$ at the indicated values of κ.

In figure 3.24 the amplitude of the streamwise velocity component is plotted as a function of η at $\bar{\Phi} = 0.5$ for different values of κ. It is shown that the amplitude of the streamwise velocity component increases as κ decreases. This confirms what already observed in figure 3.23 (right) where it is evident that for larger values of κ the maximum value of the streamwise velocity component is smaller for every streamwise position.

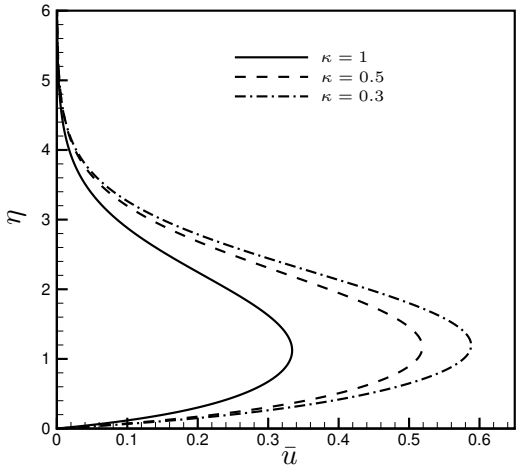

Fig. 3.24: Streamwise velocity component at $\bar{\Phi} = 0.5$ for different values of κ.

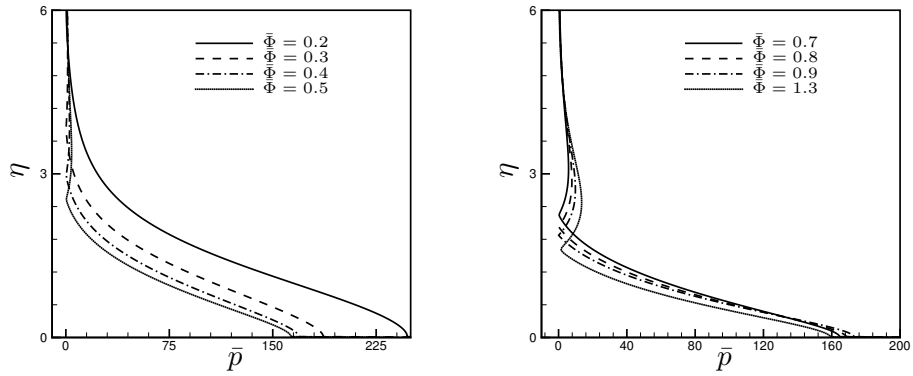

Fig. 3.25: Pressure profiles at the indicated values of $\bar{\Phi}$.

Figure 3.25 show the perturbation pressure at the indicated values of $\bar{\Phi}$. The behavior of the pressure is due to the free-stream matching requirements. The outer perturbation pressure is small, therefore the inner perturbation pressure is small at large distance form the body, however its value at the wall is significantly high.

Figure 3.26 shows the shear at the wall as a function of $\bar{\Phi}$. It has been obtained by evaluating the derivative of the streamwise velocity component with respect

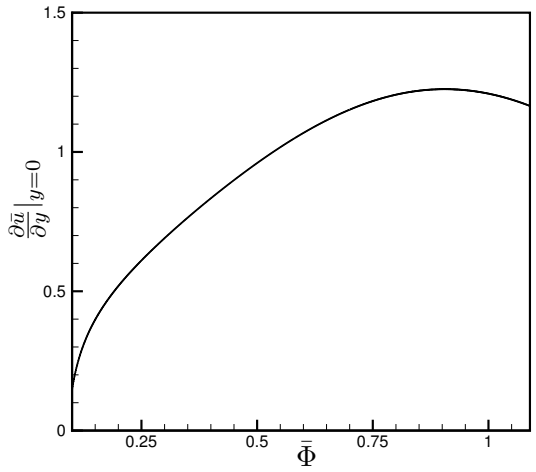

Fig. 3.26: Shear at the wall along the body.

to the normal variable at each streamwise position. The shear increases at first, then it reaches a maximum value and eventually it decreases downstream.

Figure 3.27 shows the effect of changing the grid position on the spanwise velocity component. The outer perturbation velocity decays downstream, therefore by decreasing the distance between the grid and the body, the outer velocity would have a higher value at the same streamwise position and since the matching has been employed, the inner perturbation velocity would have a higher value for large η. However the grid cannot be too close to the body because there would be a singularity in the outer perturbation velocity solution due to the stagnation point, where the mean flow is zero. This is why the outer value is always small for positive $\bar{\Phi}$, as shown in figure 3.27.

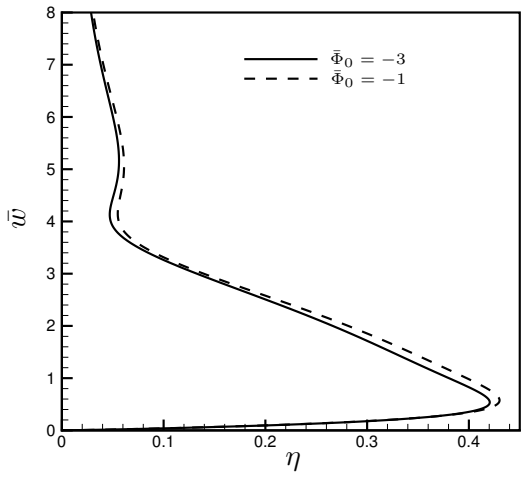

Fig. 3.27: Effect of the grid position on the spanwise velocity component.

4. CONCLUSIONS AND FUTURE WORK

The downstream evolution of a perturbed incompressible flow at high Reynolds numbers around a Rankine body has been analysed. In the outer region around the body the flow is decomposed in a mean flow and a perturbation flow. The first one is given by a uniform flow which encounters a source flow because the considered geometry is well represented by this flow. The outer mean velocity and pressure are analysed along the body's surface. The solution for the outer perturbation flow is found in a new set of coordinates which are called optimal coordinates because they follow the shape of the body. The velocity components are made dimensionless by the local outer mean flow and the outer perturbation velocity is decomposed in a homogeneous part and a potential part which is linked with the perturbation pressure variation. The homogeneous perturbation velocity solution is found by solving analytically the homogeneous Navier-Stokes equations in optimal coordinates. The perturbation potential is then found by using the continuity equations and the perturbation pressure is a function of the perturbation potential.

In the boundary layer region the mean flow satisfies the steady nonlinear mean flow equations without similarity in optimal coordinates while the perturbation flow is governed by the linearised unsteady boundary region equations in optimal coordinates. As for the outer region, the scale for the inner perturbation velocity is the local outer mean velocity. The boundary region equations satisfy appropriate boundary conditions derived from matching with the solution in the outer region and no-slip condition at the wall. Initial conditions for boundary

layer equations have been derived considering that at the stagnation point the inner mean flow is the well known Hiemenz flow and a set of equations in Cartesian coordinates for the perturbation flow at the stagnation point is derived. In order to obtain a solution independent by the streamwise coordinate a power series solution is assumed and substituted into the linearised Hiemenz Navier-Stokes equations. The solution for the series is found numerically and it is used to build the initial condition for the boundary region equations. The spanwise velocity component is only rescaled because the spanwise direction is the same for the stagnation point and the Rankine body. The streamwise velocity component is calculated at the initial streamwise coordinate Φ for each stagnation point streamwise coordinate x_{H}. The two coordinates do not coincide because of the curvature therefore it is necessary to build the initial condition from the solution of the series as well as rescaling the velocity component by the local outer mean velocity. The normal initial velocity component is found by integrating the continuity equation in optimal coordinates.

The effect of the curvature and the mean pressure gradient on the velocity profiles has been analyzed. The streamwise wavenumber also plays a role on the streaks amplitude. It has also been demonstrated that the inner perturbation pressure matches the outer perturbation pressure which has a very important role in the boundary layer dynamics. The shape of the streaks is different compared to flat-plate boundary layer, but the behavior is the same: the streamwise velocity component initially increases in magnitude and then it decreases by moving downstream while the spanwise velocity component, which matches the outer perturbation spanwise velocity component at large distance from the body, decreases in magnitude moving downstream. The value and the location of the maximum of the streamwise velocity component also changes from the flat plate case. In fact, the η value where the velocity has its maximum value is different at each

streamwise position, due to the non-similarity of the problem. The effect of the Reynolds number and the streamwise wavenumber on the streaks has also been analysed, showing an influence on the amplitude of the streaks. The numerical solution of the boundary region equations shows a perturbation pressure which is significantly high at the wall and its behavior is due to the matching with the outer perturbation pressure, which is very small. The shear at the wall along the body has been shown to initially increse up to a maximum value and then slowly decrease moving downstream. The position of the grid where the disturbance is generated plays a relevant role on the value of the velocity at large distance from the body because it determines the position where the outer perturbation flow has decayed.

In this thesis we have constructed the unsteady and three-dimensional flow generated by the free-stream forcing. This is the first step towards the formulation of the nonlinear problem, where the interactions between the mean flow and the perturbation flow inside the boundary layer are considered. To our knowledge, this is the first study to deal with investigate both the perturbation outer and inner flows around a Rankine body, considering the effects of the curvature and the pressure gradient. To verify our results, a comparison with the flat-plate case has been performed and we observed a good match between our solution and the flat-plate solution. The findings of our research are quite convincing, but additional theoretical and experimental work is required in order to fully understand the Klebanoff mode generation and growth over a Rankine body.

The rigorous mathematical approach used in this work could be useful to extend the results to more complex cases and some ideas have already been developed.

- Studying the evolution of order-one disturbances by solving the nonlinear boundary-region equations. It is interesting because in real applications

the superimposed perturbation flow is of the same order of the mean flow. In effect, experimental results on bypass transitions show the interaction between the mean and the perturbation flow which leads to turbulence. In this case the amplitude ϵ of the disturbance is of the same order of the amplitude of the mean flow therefore when the boundary region equations are derived, terms of order ϵ^2 cannot be neglected. The equations for the perturbation flow are then nonlinear and the modes are coupled so that it is not possible to analyse only a single mode as for the linear case studied herein.

- Using nonlinear streaks as a base flow to study secondary instabilities. This is useful to have correct initial conditions for direct numerical simulation. In fact, DNS could be employed to analyze secondary instabilities by solving numerically the complete Navier-Stokes equations, but an initial condition is still required. This could be provided by the nonlinear streaks.

- Studying the perturbed flow around a wedge body. In this case there would be Falkner-Skan boundary layer with self similar equations along the entire body. The only parameter which would be interesting to change is the angle β in the equations of the inner mean flow. The boundary layer equations are the same for the Rankine body and the analysis of the outer flow is the same. The only difference is in defining the outer mean flow which for a Rankine body is given by a uniform flow plus a source flow and upstream the flow is uniform, which allows us to define the gust. The challenge is finding a way to describe the wedge flow with a combination of sources which is also uniform upstream.

APPENDIX

A. DERIVATION OF CONTINUITY AND NAVIER-STOKES EQUATIONS IN OPTIMAL COORDINATES

Since the body is not a flat plate the analysis of the outer and inner flows is made in a new coordinate system. In order to fully understand the significance of this choice, it is necessary to make a regression to explain how a general change of coordinates is made. Switching from $x-y$ orthogonal coordinate system to an another generic orthogonal coordinate system $\Phi-\Psi$, the following relation is valid

$$\mathrm{d}x^2+\mathrm{d}y^2=h_\Phi^2\mathrm{d}\Phi^2+h_\Psi^2\mathrm{d}\Psi^2,$$

where h_Φ and h_Ψ are the transformation coefficients.

It can be easily demonstrated that

$$h_\Psi^2=\frac{(\frac{\partial\Phi}{\partial y})^2-(\frac{\partial\Phi}{\partial x})^2}{(\frac{\partial\Psi}{\partial x})^2(\frac{\partial\Phi}{\partial y})^2-(\frac{\partial\Phi}{\partial x})^2(\frac{\partial\Psi}{\partial y})^2}, \tag{A.1a}$$

$$h_\Phi^2=\frac{(\frac{\partial\Psi}{\partial x})^2-(\frac{\partial\Psi}{\partial y})^2}{(\frac{\partial\Psi}{\partial x})^2(\frac{\partial\Phi}{\partial y})^2-(\frac{\partial\Phi}{\partial x})^2(\frac{\partial\Psi}{\partial y})^2}. \tag{A.1b}$$

Now the general transformation coefficients can be calculated. A special orthogonal coordinate system is chosen, Φ-Ψ where Φ is the potential function and Ψ is the streamfunction of the outer mean flow $\widetilde{U}$ of components $\widetilde{U}$ and $\widetilde{V}$. By definition the following relations are valid

$$\widetilde{U} = \frac{\partial \Phi}{\partial x} = \frac{\partial \Psi}{\partial y}, \tag{A.2a}$$

$$\widetilde{V} = \frac{\partial \Phi}{\partial y} = -\frac{\partial \Psi}{\partial x}. \tag{A.2b}$$

By calculating the transformation coefficient from (A.1a) and (A.1b) the result is that

$$h_\Phi^2 = h_\Psi^2 = \frac{1}{|\widetilde{\mathbf{U}}|^2} = \frac{1}{\widetilde{U}^2 + \widetilde{V}^2}.$$

Then

$$\mathrm{d}x^2 + \mathrm{d}y^2 = h_\Phi^2 \mathrm{d}\Phi^2 + h_\Psi^2 \mathrm{d}\Psi^2 = \frac{\mathrm{d}\Phi^2 + \mathrm{d}\Psi^2}{|\widetilde{\mathbf{U}}|^2}. \tag{A.3}$$

Now it is important to see how gradient, divergence and curl operations change when the coordinate system changes. The function a is a scalar and $\mathbf{A}$ is a vector with components (A_Φ, A_Ψ, A_z) (these components are in the new directions); The new coordinate system is Φ, Ψ, z, the new directions are $\hat{e}_\Phi, \hat{e}_\Psi, \hat{e}_z$ and the transformation coefficients are h_Φ, h_Ψ, h_z. The divergence, gradient and curl are defined as follows:

$$\begin{aligned} \nabla \cdot \mathbf{A} = \frac{\partial A_x}{\partial x} + \frac{\partial A_y}{\partial y} + \frac{\partial A_z}{\partial z} = \\ \frac{1}{h_\Phi h_\Psi h_z}\left[\frac{\partial (h_\Psi h_z A_\Phi)}{\partial \Phi} + \frac{\partial (h_\Phi h_z A_\Psi)}{\partial \Psi} + \frac{\partial (h_\Phi h_\Psi A_z)}{\partial z}\right], \end{aligned} \tag{A.4a}$$

$$\nabla a = \hat{i}\frac{\partial a}{\partial x} + \hat{j}\frac{\partial a}{\partial y} + \hat{k}\frac{\partial a}{\partial z} = \hat{e}_\Phi \frac{1}{h_\Phi}\frac{\partial a}{\partial \Phi} + \hat{e}_\Psi \frac{1}{h_\Psi}\frac{\partial a}{\partial \Psi} + \hat{e}_z \frac{1}{h_z}\frac{\partial a}{\partial z}, \tag{A.4b}$$

$$\begin{aligned} \nabla \times \mathbf{A} = \hat{i}\left(\frac{\partial A_z}{\partial y} - \frac{\partial A_y}{\partial z}\right) - \hat{j}\left(\frac{\partial A_z}{\partial x} - \frac{\partial A_x}{\partial z}\right) + \hat{k}\left(\frac{\partial A_y}{\partial x} - \frac{\partial A_x}{\partial y}\right) = \\ \frac{1}{h_\Phi h_\Psi h_z}\left[\hat{e}_\Phi h_\Phi \left(\frac{\partial (h_z A_z)}{\partial \Psi} - \frac{\partial (h_\Psi A_\Psi)}{\partial z}\right) - \hat{e}_\Psi h_\Psi \left(\frac{\partial (h_z A_z)}{\partial \Phi} - \frac{\partial (h_\Phi A_\Phi)}{\partial z}\right)\right] + \\ \frac{\hat{e}_z h_z}{h_\Phi h_\Psi h_z}\left(\frac{\partial (h_\Psi A_\Psi)}{\partial \Phi} - \frac{\partial (h_\Phi A_\Phi)}{\partial \Psi}\right). \end{aligned} \tag{A.4c}$$

Relations (A.4) are used to obtain the continuity and Navier-Stokes equations in the new coordinate system. In the case considered here

$$h_\Phi = h_\Psi = \frac{1}{|\widetilde{\mathbf{U}}|},$$

$$h_z = 1.$$

In order to derive the continuity and Navier-Stokes equations in optimal coordinates namely from (x,y,z) to (Φ,Ψ,z), the following equation is used to write the term $\nabla \cdot (\nabla \mathbf{V})$ in another way

$$\nabla \cdot \nabla \mathbf{V} = \nabla(\nabla \cdot \mathbf{V}) - \nabla \times \nabla \times \mathbf{V}. \tag{A.5}$$

By the continuity equation the term $\nabla \cdot \mathbf{V}$ is zero. Thus (A.5) becomes

$$\nabla \cdot \nabla \mathbf{V} = -\nabla \times \nabla \times \mathbf{V}. \tag{A.6}$$

Moreover, it is easy to demonstrate the following relation:

$$\mathbf{V} \cdot \nabla \mathbf{V} = \nabla \left(\frac{|\mathbf{V}|^2}{2} \right) - \mathbf{V} \times \nabla \times \mathbf{V}. \tag{A.7}$$

By substituting (A.6) and (A.7) in the continuity equation and the following Navier-Stokes equations

$$\nabla \cdot \mathbf{V} = 0, \tag{A.8}$$

$$\frac{\partial \mathbf{V}}{\partial t} + \mathbf{V} \cdot \nabla \mathbf{V} = -\nabla p + \frac{1}{R} \nabla \cdot (\nabla \mathbf{V}), \tag{A.9}$$

where R is the Reynolds number, it is obtained

$$\frac{\partial \mathbf{V}}{\partial t} + \nabla \left(\frac{|\mathbf{V}|^2}{2} \right) - \mathbf{V} \times \nabla \times \mathbf{V} = -\nabla p - \frac{1}{R} \nabla \times \nabla \times \mathbf{V}, \tag{A.10}$$

which is another form of the Navier-Stokes equation.

By equations (A.4) it is easy to see the the continuity equation in optimal coordinates is

$$\widetilde{U}\frac{\partial w_\Phi}{\partial \Phi}+\widetilde{U}\frac{\partial w_\Psi}{\partial \Psi}+\frac{\partial w_z}{\partial z}=0, \tag{A.11}$$

where $\widetilde{U}=|\widetilde{\mathbf{U}}|$, $w_\Phi = u/\widetilde{U}$, $w_\Psi = u/\widetilde{U}$ and $w_z = w/\widetilde{U}$, with u and u the velocity components in the Φ and Ψ directions respectively.

In order to find the Navier-Stokes equations in optimal coordinates the following passages are made

$$\nabla\left(\frac{\mathbf{V}^2}{2}\right)=\begin{pmatrix}\widetilde{U}\frac{\partial}{\partial\Phi}\left(\frac{u^2+v^2+w^2}{2}\right)\\ \widetilde{U}\frac{\partial}{\partial\Psi}\left(\frac{u^2+v^2+w^2}{2}\right)\\ \frac{\partial}{\partial z}\left(\frac{u^2+v^2+w^2}{2}\right)\end{pmatrix},$$

$$\mathbf{V}\times\nabla\times\mathbf{V}=\widetilde{U}^2\begin{vmatrix} 1 & 1 & 1\\ u & v & w\\ \frac{1}{\widetilde{U}}\left[\frac{\partial w}{\partial\Psi}-\frac{\partial}{\partial z}\left(\frac{v}{\widetilde{U}}\right)\right] & \frac{1}{\widetilde{U}}\left[\frac{\partial}{\partial z}\left(\frac{u}{\widetilde{U}}\right)-\frac{\partial w}{\partial\Phi}\right] & \left[\frac{\partial}{\partial\Phi}\left(\frac{v}{\widetilde{U}}\right)-\frac{\partial}{\partial\Psi}\left(\frac{u}{\widetilde{U}}\right)\right]\end{vmatrix}=$$

$$= \widetilde{U}^2 \begin{pmatrix} v\left[\frac{\partial}{\partial\Phi}\left(\frac{v}{\widetilde{U}}\right) - \frac{\partial}{\partial\Psi}\left(\frac{u}{\widetilde{U}}\right)\right] - \frac{w}{\widetilde{U}}\left[\frac{\partial}{\partial z}\left(\frac{u}{\widetilde{U}}\right) - \frac{\partial w}{\partial\Phi}\right] \\ \\ \frac{w}{\widetilde{U}}\left[\frac{\partial w}{\partial\Psi} - \frac{\partial}{\partial z}\left(\frac{v}{\widetilde{U}}\right)\right] - u\left[\frac{\partial}{\partial\Phi}\left(\frac{v}{\widetilde{U}}\right) - \frac{\partial}{\partial\Psi}\left(\frac{u}{\widetilde{U}}\right)\right] \\ \\ \frac{u}{\widetilde{U}}\left[\frac{\partial}{\partial z}\left(\frac{u}{\widetilde{U}}\right) - \frac{\partial w}{\partial\Phi}\right] - \frac{v}{\widetilde{U}}\left[\frac{\partial w}{\partial\Psi} - \frac{\partial}{\partial z}\left(\frac{v}{\widetilde{U}}\right)\right] \end{pmatrix},$$

$$\nabla \times \nabla \times \mathbf{V} = \widetilde{U}^2 \begin{vmatrix} \frac{1}{\widetilde{U}}\left\{\frac{\partial}{\partial\Psi}\left\{\widetilde{U}^2\left[\frac{\partial}{\partial\Phi}\left(\frac{v}{\widetilde{U}}\right) - \frac{\partial}{\partial\Psi}\left(\frac{u}{\widetilde{U}}\right)\right]\right\} - \frac{\partial}{\partial z}\left[\frac{\partial}{\partial z}\left(\frac{u}{\widetilde{U}}\right) - \frac{\partial w}{\partial\Phi}\right]\right\} \\ \\ \frac{1}{\widetilde{U}}\left\{\frac{\partial}{\partial z}\left[\frac{\partial w}{\partial\Psi} - \frac{\partial}{\partial z}\left(\frac{v}{\widetilde{U}}\right)\right] - \frac{\partial}{\partial\Phi}\left\{\widetilde{U}^2\left[\frac{\partial}{\partial\Phi}\left(\frac{v}{\widetilde{U}}\right) - \frac{\partial}{\partial\Psi}\left(\frac{u}{\widetilde{U}}\right)\right]\right\}\right\} \\ \\ \frac{\partial}{\partial\Phi}\left[\frac{\partial}{\partial z}\left(\frac{u}{\widetilde{U}}\right) - \frac{\partial w}{\partial\Phi}\right] - \frac{\partial}{\partial\Psi}\left[\frac{\partial w}{\partial\Psi} - \frac{\partial}{\partial z}\left(\frac{v}{\widetilde{U}}\right)\right] \end{vmatrix},$$

and thus equation (A.10) in scalar form is

$$
\begin{aligned}
&\Phi): \frac{\partial u}{\partial t} + \widetilde{U}\frac{\partial}{\partial \Phi}\left(\frac{u^2+v^2+w^2}{2}\right) - \\
&\widetilde{U}^2\left\{v\left[\frac{\partial}{\partial \Phi}\left(\frac{v}{\widetilde{U}}\right) - \frac{\partial}{\partial \Psi}\left(\frac{u}{\widetilde{U}}\right)\right] - \frac{w}{\widetilde{U}}\left[\frac{\partial}{\partial z}\left(\frac{u}{\widetilde{U}}\right) - \frac{\partial w}{\partial \Phi}\right]\right\} = \\
&-\widetilde{U}\frac{\partial p}{\partial \Phi} - \frac{\widetilde{U}}{R}\left\{\frac{\partial}{\partial \Psi}\left\{\widetilde{U}^2\left[\frac{\partial}{\partial \Phi}\left(\frac{v}{\widetilde{U}}\right) - \frac{\partial}{\partial \Psi}\left(\frac{u}{\widetilde{U}}\right)\right]\right\} - \frac{\partial}{\partial z}\left[\frac{\partial}{\partial z}\left(\frac{u}{\widetilde{U}}\right) - \frac{\partial w}{\partial \Phi}\right]\right\},
\end{aligned}
$$

$$
\begin{aligned}
&\Psi): \frac{\partial v}{\partial t} + \widetilde{U}\frac{\partial}{\partial \Psi}\left(\frac{u^2+v^2+w^2}{2}\right) - \\
&\widetilde{U}^2\left\{\frac{w}{\widetilde{U}}\left[\frac{\partial w}{\partial \Psi} - \frac{\partial}{\partial z}\left(\frac{v}{\widetilde{U}}\right)\right] - u\left[\frac{\partial}{\partial \Phi}\left(\frac{v}{\widetilde{U}}\right) - \frac{\partial}{\partial \Psi}\left(\frac{u}{\widetilde{U}}\right)\right]\right\} = \\
&-\widetilde{U}\frac{\partial p}{\partial \Psi} - \frac{\widetilde{U}}{R}\left\{\frac{\partial}{\partial z}\left[\frac{\partial w}{\partial \Psi} - \frac{\partial}{\partial z}\left(\frac{v}{\widetilde{U}}\right)\right] - \frac{\partial}{\partial \Phi}\left\{\widetilde{U}^2\left[\frac{\partial}{\partial \Phi}\left(\frac{v}{\widetilde{U}}\right) - \frac{\partial}{\partial \Psi}\left(\frac{u}{\widetilde{U}}\right)\right]\right\}\right\},
\end{aligned}
$$

$$
\begin{aligned}
&z): \frac{\partial w}{\partial t} + \frac{\partial}{\partial z}\left(\frac{u^2+v^2+w^2}{2}\right) - \\
&\widetilde{U}\left\{u\left[\frac{\partial}{\partial z}\left(\frac{u}{\widetilde{U}}\right) - \frac{\partial w}{\partial \Phi}\right] - v\left[\frac{\partial w}{\partial \Psi} - \frac{\partial}{\partial z}\left(\frac{v}{\widetilde{U}}\right)\right]\right\} = \\
&-\frac{\partial p}{\partial z} - \frac{\widetilde{U}^2}{R}\left\{\frac{\partial}{\partial \Phi}\left[\frac{\partial}{\partial z}\left(\frac{u}{\widetilde{U}}\right) - \frac{\partial w}{\partial \Phi}\right] - \frac{\partial}{\partial \Psi}\left[\frac{\partial w}{\partial \Psi} - \frac{\partial}{\partial z}\left(\frac{v}{\widetilde{U}}\right)\right]\right\},
\end{aligned}
$$

where u,v,w are the velocity components in the Φ,Ψ,z directions (not in x,y,z

directions). Rearranging and simplifying it is obtained

$$\Phi): \frac{1}{\widetilde{U}^2}\frac{\partial w_\Phi}{\partial t} + w_\Phi\frac{\partial w_\Phi}{\partial \Phi} + w_\Psi\frac{\partial w_\Phi}{\partial \Psi} + \frac{w_z}{\widetilde{U}}\frac{\partial w_\Phi}{\partial z} + (w_\Phi^2 + w_\Psi^2)\frac{\partial}{\partial \Phi}(\ln \widetilde{U}) = -\frac{1}{V_0^2}\frac{\partial p}{\partial \Phi} +$$

$$\frac{1}{R}\left[\frac{\partial^2 w_\Phi}{\partial \Phi^2} + \frac{\partial^2 w_\Phi}{\partial \Psi^2} + \frac{1}{V_0^2}\frac{\partial^2 w_\Phi}{\partial z^2} - 2\frac{\partial \ln \widetilde{U}}{\partial \Psi}\left(\frac{\partial w_\Psi}{\partial \Phi} - \frac{\partial w_\Phi}{\partial \Psi}\right) - \frac{2}{\widetilde{U}}\frac{\partial \ln \widetilde{U}}{\partial \Phi}\frac{\partial w_z}{\partial z}\right],$$

$$\Psi): \frac{1}{\widetilde{U}^2}\frac{\partial w_\Psi}{\partial t} + w_\Phi\frac{\partial w_\Psi}{\partial \Phi} + w_\Psi\frac{\partial w_\Psi}{\partial \Psi} + \frac{w_z}{\widetilde{U}}\frac{\partial w_\Psi}{\partial z} + (w_\Phi^2 + w_\Psi^2)\frac{\partial}{\partial \Psi}(\ln \widetilde{U}) = -\frac{1}{V_0^2}\frac{\partial p}{\partial \Psi} +$$

$$\frac{1}{R}\left[\frac{\partial^2 w_\Psi}{\partial \Phi^2} + \frac{\partial^2 w_\Psi}{\partial \Psi^2} + \frac{1}{V_0^2}\frac{\partial^2 w_\Psi}{\partial z^2} + 2\frac{\partial \ln \widetilde{U}}{\partial \Phi}\left(\frac{\partial w_\Psi}{\partial \Phi} - \frac{\partial w_\Phi}{\partial \Psi}\right) - \frac{2}{\widetilde{U}}\frac{\partial \ln \widetilde{U}}{\partial \Psi}\frac{\partial w_z}{\partial z}\right],$$

$$z): \frac{1}{\widetilde{U}^2}\frac{\partial w_z}{\partial t} + w_\Phi\frac{\partial w_z}{\partial \Phi} + w_\Psi\frac{\partial w_z}{\partial \Psi} + \frac{w_z}{\widetilde{U}}\frac{\partial w_z}{\partial z} + w_z\left(w_\Phi\frac{\partial \ln \widetilde{U}}{\partial \Phi} + w_\Psi\frac{\partial \ln \widetilde{U}}{\partial \Psi}\right) =$$

$$-\frac{1}{V_0^3}\frac{\partial p}{\partial z} +$$
$$\frac{1}{R}\left[\frac{\partial^2 w_z}{\partial \Phi^2} + \frac{\partial^2 w_z}{\partial \Psi^2} + \frac{1}{V_0^2}\frac{\partial^2 w_z}{\partial z^2} + \frac{w_z}{\widetilde{U}}\left(\frac{\partial^2 \widetilde{U}}{\partial \Phi^2} + \frac{\partial^2 \widetilde{U}}{\partial \Psi^2}\right) + 2\left(\frac{\partial w_z}{\partial \Phi}\frac{\partial \ln \widetilde{U}}{\partial \Phi} + \frac{\partial w_z}{\partial \Psi}\frac{\partial \ln \widetilde{U}}{\partial \Psi}\right)\right].$$

B. DERIVATION OF CONTINUITY AND NAVIER-STOKES EQUATIONS FOR THE INNER MEAN FLOW

The equations which govern the mean flow inside the boundary layer are derived. The mean flow velocity components and pressure are (U, V, P). During the derivation of the non-dimensional Navier-Stokes equations in optimal coordinates we scaled all the legths by the characteristic lenght of the body L^*. The key point in the boundary layer theory is the existence of two different length scales

- the characteristic length of the body L^*,
- the boundary layer thickness $\delta^* \ll L^*$.

We now take L^* as scale in the streamwise direction and δ^* as scale in the normal direction. The boundary layer thickness δ^* actually varies along the body, but we choose it to be the value at one fixed streamwise position so that it is constant. We also expect different scales for the velocity components (U, V). The aim is to have all the flow variables of order 1. From the continuity equation (2.5) it is clear that both the normal velocity component V and the normal coordinate Ψ_{L} are of order δ

$$\frac{\partial U}{\partial \Phi_{\mathrm{L}}} + \frac{\partial V_\delta}{\partial \Psi_{\mathrm{L}\delta}} \frac{\delta}{\delta} = 0,$$

with $V_\delta = V/\delta = \mathcal{O}(1)$, $\Psi_{\mathrm{L}\delta} = \Psi_{\mathrm{L}}/\delta = \mathcal{O}(1)$ and δ the non-dimensional boundary layer thickness. The Φ-momentum equation is obtained by expressing the equation in terms of these rescaled variables, so that some terms become small and they can be ignored. The boundary layer thickness is proportional to $R_{\mathrm{L}}^{-1/2}$

therefore some viscous terms cannot be neglected in the equations. The same line of reasoning is used for the Ψ-momentum equation and it is assumed that the outer mean velocity $\widetilde{U} = \widetilde{U}_b$ in the boundary layer. The momentum equations for the mean flow in the boundary layer are

$$U\frac{\partial U}{\partial \Phi_{\mathrm{L}}} + V_\delta \frac{\partial U}{\partial \Psi_{\mathrm{L}\delta}} + \frac{1}{\widetilde{U}_b}\frac{\partial \widetilde{U}_b}{\partial \Phi_{\mathrm{L}}}U^2 = -\frac{1}{\widetilde{U}_b^2}\frac{\partial P}{\partial \Phi_{\mathrm{L}}} + \frac{1}{R_{\mathrm{L}}}\frac{\partial^2 U}{\partial \Psi_{\mathrm{L}\delta}^2},$$

$$\frac{\partial P}{\partial \Psi_{\mathrm{L}\delta}} = 0.$$

For convenience the subscript δ in section 2.3.2 has been omitted. The stream-function and the inner variable are defined

$$\widetilde{\Psi} = F(\Phi_{\mathrm{L}}, \eta)\sqrt{\frac{2\Phi_{\mathrm{L}}}{R_{\mathrm{L}}}}, \qquad \eta = \Psi_{\mathrm{L}}\sqrt{\frac{R_{\mathrm{L}}}{2\Phi_{\mathrm{L}}}}.$$

The following relationships are valid:

$$\begin{aligned}
&U = F', \\
&V = -\left[\sqrt{\frac{2\Phi_{\mathrm{L}}}{R_{\mathrm{L}}}}\left(F_{\Phi_{\mathrm{L}}} - F'\frac{\eta}{2\Phi_{\mathrm{L}}}\right) + \frac{F}{2}\sqrt{\frac{2}{R_{\mathrm{L}}\Phi_{\mathrm{L}}}}\right], \\
&\frac{\partial U}{\partial \Phi_{\mathrm{L}}} = \frac{\partial F'}{\partial \Phi_{\mathrm{L}}} + \frac{\eta}{2\Phi_{\mathrm{L}}}F'', \\
&\frac{\partial U}{\partial \Psi_{\mathrm{L}}} = F''\sqrt{\frac{R_{\mathrm{L}}}{2\Phi_{\mathrm{L}}}}, \\
&\frac{\partial^2 U}{\partial \Psi_{\mathrm{L}}^2} = F'''\frac{R_{\mathrm{L}}}{2\Phi_{\mathrm{L}}}, \\
&\frac{\partial P}{\partial \Phi_{\mathrm{L}}} = -\widetilde{U}_b\frac{\partial \widetilde{U}_b}{\partial \Phi_{\mathrm{L}}} \Rightarrow -\frac{1}{\widetilde{U}_b}\frac{\partial P}{\partial \Phi_{\mathrm{L}}} = \frac{1}{\widetilde{U}}\frac{\partial \widetilde{U}_b}{\partial \Phi_{\mathrm{L}}}.
\end{aligned}$$

By substituting these relationships into equation (2.20), it is obtained

$$\begin{aligned}
&F'\left(\frac{\partial F'}{\partial \Phi_{\mathrm{L}}} + \frac{\eta}{2\Phi_{\mathrm{L}}}F''\right) - \\
&\left[\sqrt{\frac{2\Phi_{\mathrm{L}}}{R_{\mathrm{L}}}}\left(F_{\Phi_{\mathrm{L}}} - F'\frac{\eta}{2\Phi_{\mathrm{L}}}\right) + \frac{F}{2}\sqrt{\frac{2}{R_{\mathrm{L}}\Phi_{\mathrm{L}}}}\right]F''\sqrt{\frac{R_{\mathrm{L}}}{2\Phi_{\mathrm{L}}}} + \frac{1}{\widetilde{U}_b}\frac{\partial \widetilde{U}_b}{\partial \Phi_{\mathrm{L}}}F'^2 = \\
&\frac{1}{\widetilde{U}_b}\frac{\partial \widetilde{U}_b}{\partial \Phi_{\mathrm{L}}} + \frac{1}{R_{\mathrm{L}}}F'''\frac{R_{\mathrm{L}}}{2\Phi_{\mathrm{L}}},
\end{aligned}$$

that becomes

$$\frac{F'''}{2\Phi_{\mathrm{L}}}+\frac{FF''}{2\Phi_{\mathrm{L}}}+\frac{1}{\widetilde{U}_b}\frac{\partial\widetilde{U}_b}{\partial\Phi_{\mathrm{L}}}(1-F'^2)=F'\frac{\partial F'}{\partial\Phi_{\mathrm{L}}}-\frac{\partial F}{\partial\Phi_{\mathrm{L}}}F''+\cancel{F'F''\frac{\eta}{2\Phi_{\mathrm{L}}}}-\cancel{F'F''\frac{\eta}{2\Phi_{\mathrm{L}}}}.$$

Multiplying both sides by $2\Phi_{\mathrm{L}}$ we have

$$F'''+FF''+2m(\Phi_{\mathrm{L}})(1-F'^2)=2\Phi_{\mathrm{L}}(F'F'_{\Phi_{\mathrm{L}}}-F_{\Phi_{\mathrm{L}}}F''),$$

where

$$F'=\frac{\partial F}{\partial\eta},\qquad F_{\Phi_{\mathrm{L}}}=\frac{\partial F}{\partial\Phi_{\mathrm{L}}},\qquad m=\frac{\Phi_{\mathrm{L}}}{\widetilde{U}_b}\frac{\mathrm{d}\widetilde{U}_b}{\mathrm{d}\Phi_{\mathrm{L}}}.$$

C. DISPLACEMENT EFFECT

The Navier-Stokes equations have been derived in optimal coordinates without displacement Φ-Ψ and the inviscid mean flow without displacement has been found numerically as a function of Φ-Ψ. In the same fashion, the Navier-Stokes equations can be derived in displaced coordinates Φ_d-Ψ_d, where Φ_d-Ψ_d are the potential and streamfunction of the displaced mean flow. The first observation is that as the inviscid mean flow with no displacement has only the Φ-component in optimal coordinates without displacement, the displaced mean flow has only the Φ_d-component in displaced coordinates. However, the displaced mean flow has two components in the Φ-Ψ plane, as shown in figure C.1.

We need to find Φ_d, Ψ_d and the mean inviscid displaced mean flow as functions of the not-displaced coordinates Φ-Ψ. In order to do that, we need to solve the Laplace equation for the displaced streamfunction Ψ_d in (Φ, Ψ) optimal coordinates. Therefore, we need to define the streamfunction associated with the displaced mean flow

$$\widetilde{\mathbf{U}} = (\widetilde{U}_d, \widetilde{V}_d, 0) \qquad \widetilde{U}_d = \frac{\partial \Psi_d}{\partial \Psi} \qquad \widetilde{V}_d = -\frac{\partial \Psi_d}{\partial \Phi}, \tag{C.1}$$

where

- $\widetilde{U}_d = \widetilde{U}_d^* / \widetilde{U}^*$ is the mean velocity component along Φ,
- $\widetilde{V}_d = \widetilde{V}_d^* / \widetilde{U}^*$ is the mean velocity component along Ψ,
- $\widetilde{U}^*$ is the absolute value of the inviscid mean flow without displacement.

The velocity components (C.1) satisfy the continuity equations and Navier-Stokes equations in optimal displaced coordinates.

The vorticity of the inviscid displaced mean flow (C.1) must be zero, therefore

$$\nabla \times \widetilde{\mathbf{U}}_{\mathbf{d}} = \frac{\partial \widetilde{V}_d}{\partial \Phi} - \frac{\partial \widetilde{U}_d}{\partial \Psi} = 0, \tag{C.2}$$

the streamfunction can be written as

$$\Psi_d(\Phi, \Psi) = \Psi + R^{-1/2}\Psi_d(\Phi, \Psi).$$

It follows that the problem to be solved is

$$\nabla^2 \Psi_d = \frac{\partial^2 \Psi_d}{\partial \Phi^2} + \frac{\partial^2 \Psi_d}{\partial \Psi^2} = 0, \tag{C.3}$$

$$\Psi_d(\phi, 0) = -\beta(\Phi)\sqrt{\Phi}, \Phi > 0, \tag{C.4}$$

$$\Psi_d(\Phi, 0) = 0, \Phi < 0, \tag{C.5}$$

$$\Psi_d = 0 \quad \text{as} \quad \Psi \to \infty, \tag{C.6}$$

$$\Psi_d = 0 \quad \text{as} \quad \Psi \to -\infty. \tag{C.7}$$

If $\beta(\Phi)$ were a constant the problem could be easily solved by analytic continuation to the complex plane, (Van Dyke (1975) pages 134-135). But it is not constant, so it is solved numerically. The same line of reasoning is used for the potential $\Phi_d(\Phi, \Psi)$ so that we have numerically $\Phi_d(\Phi, \Psi)$, $\Psi_d(\Phi, \Psi)$ and $\widetilde{\mathbf{U}}(\Phi_d, \Psi_d)$. The analysis of the outer perturbation flow is performed by using these displaced coordinates.

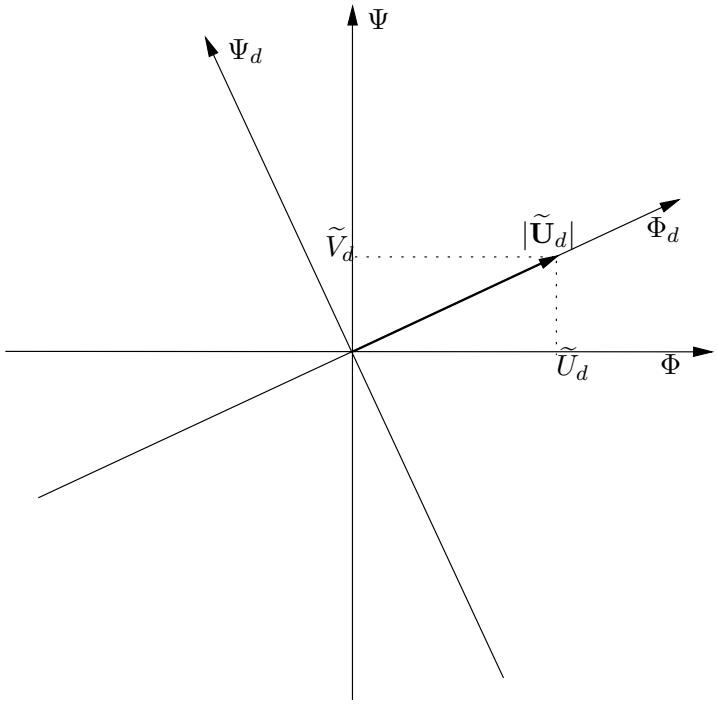

Fig. C.1: Outer potential displaced velocity in Φ-Ψ plane and Φ_d-Ψ_d plane.

D. NEWTON-RAPHSON ALGORITHM

```
void  get_x_y_r_theta(double PHI,double PSI,int opt){

//Stagnation point
if(PHI==0.0 && PSI==0.0){
x=-Lambda/(2.0*PI);
y=0.0;
R=fabs(x);
theta=PI;
r_start=R;
theta_start=theta;
}
r_guess=r_start;
theta_guess=theta_start;
//Newton-Raphson
while(1){
a=r_guess*cos(theta_guess)+Lambda/(2.0*PI)*log(r_guess)-
Lambda/(2.0*PI)*(log(Lambda/(2.0*PI))-1.0)-PHI;
b=r_guess*sin(theta_guess)+(Lambda*theta_guess)/(2.0*PI)-Lambda/2.0-PSI;
if(fabs(a)<=toll && fabs(b)<=toll){break;}
jac_1=cos(theta_guess)+Lambda/(2.0*PI*r_guess);
jac_2=-r_guess*sin(theta_guess);
jac_3=sin(theta_guess);
```

```
jac_4=r_guess*cos(theta_guess)+Lambda/(2.0*PI);

det_j=jac_1*jac_4-jac_2*jac_3;

h_r=(a*jac_4-b*jac_2)/det_j;

h_theta=(b*jac_1-a*jac_3)/det_j;

r_guess=fabs(r_guess-h_r);

theta_guess=fabs(theta_guess-h_theta);

}

R=r_guess;

theta=theta_guess;

x=R*cos(theta);

y=R*sin(theta);

r_start=r_guess;

theta_start=theta_guess;


}
```

E. EIKONAL EQUATION

In this appendix an alternative method employed by Goldstein (1984) to solve the outer perturbation flow is illustrated. The focus is on the Eikonal equation, a nonlinear partial differential equation obtained during the analysis. The main difference with our method is that upstream it is considered that $\lambda^* \ll L^*$, where λ^* represents the wavelengths in all the three directions. Equation (2.34) was obtained by using the outer scale L^* and $1/R_{\mathrm{L}}$ is a small parameter because R_{L} is large. It is solved by employing WKBJ theory, which is used to obtain the approximate solution of a linear differential equation whose highest derivative is multiplied by a small parameter (Bender & Orszag, 1999). In this case the small parameter used to obtain the solution is not in the equations, but the time scale of perturbation motion is much smaller than the characteristic time of mean flow. Moreover the spatial scale of the perturbation is much smaller than L^* which is used in analogy to the application of WKBJ theory to classical ordinary differential equations, where the equations are initially scaled by the larger scale. This case is very similar to that one of Holmes (2013) where there is not a small parameter in the equations, then it is not obvious how to use WKBJ theory. By using WKBJ theory the solution to (2.34) can be taken of the form

$$\tilde{\mathbf{u}}_{\mathrm{H}} = e^{iks}\left(\tilde{\mathbf{u}}_0 + \frac{1}{ik}\tilde{\mathbf{u}}_1 + ...\right)e^{ik(k_{3G}z_{\mathrm{L}} - t_{\mathrm{L}})}, \tag{E.1}$$

where $k = 2\pi L^*/\lambda^*_{\Phi} \gg 1$ and $k_{3G} = \lambda^*_{\Phi}/\lambda^*_z$. Thus to find $\tilde{\mathbf{u}}_{\mathrm{H}}$ it is necessary to find $s(x_{\mathrm{L}}, y_{\mathrm{L}})$ and $\tilde{\mathbf{u}}_0(x_{\mathrm{L}}, y_{\mathrm{L}})$. By substituting (E.1) in (2.34) and equating coefficients of inverse powers of k, the following are obtained

$$1 - \widetilde{\mathbf{U}} \cdot \nabla s = -\frac{i}{R_{\lambda_\Phi}}(\nabla s \cdot \nabla s + k_{3G}^2), \tag{E.2}$$

$$\widetilde{\mathbf{U}} \cdot \nabla \tilde{\mathbf{u}}_0 - \frac{2i}{R_{\lambda_\Phi}} \nabla s \cdot \nabla \tilde{\mathbf{u}}_0 - \frac{i}{R_{\lambda_\Phi}} \tilde{\mathbf{u}}_0 \nabla^2 s + \tilde{\mathbf{u}}_0 \cdot \nabla \widetilde{\mathbf{U}} = 0, \tag{E.3}$$

where $R_{\lambda_\Phi} = R_{\mathrm{L}}/k = \mathcal{O}(1)$.

It has to be remarked that in obtaining equation (E.2) the following assumptions have been made:

- $\lambda_\Phi^*, \lambda_\Psi^*, \lambda_z^* \ll L^*$ namely the wavelengths of the disturbance in the three spacial directions are all of the same order and they are all smaller than the characteristic length of the body L^*.

- R_{λ_Φ} is of order 1. This assumption permitted to use WKBJ theory to expand the solution for the velocity as in (E.1). This theory is used to obtain the approximated solution of partial differential equations whose highest derivative is multiplied by a small parameter. The equation for $\tilde{\mathbf{u}}_{\mathrm{H}}$ is (2.34) where $\tilde{\mathbf{u}}_{\mathrm{H}}$ is a function of $x_{\mathrm{L}} - y_{\mathrm{L}}$ only and t_{L} is the time scaled by the mean flow velocity and L^*. The small parameter in this equation is $1/R_{\mathrm{L}}$. In WKBJ theory the solution expands as in (E.1) where the phase is normally multiplied by a large parameter, which should be the inverse of the small parameter in the equation (in this case the Reynolds number R_{L}). We actually chose to multiply the phase by k, following Goldstein (1984) and we are allowed to do that because $R_{\mathrm{L}}/k = \mathcal{O}(1)$.

As explained, it is convenient to change the coordinates from Cartesian to optimal. Here, in the outer region, the potential and streamfunction used are Φ_{L} and Ψ_{L} associated with the outer mean flow $\widetilde{\mathbf{U}}$.

A new function is introduced

$$s_{0L} = \frac{2}{R_{\lambda_\Phi}} s + i(\Phi_{\mathrm{L}} - \Phi_{\mathrm{L}0}), \tag{E.4}$$

where $\Phi_{\mathrm{L}0}$ is an arbitrary constant and $s_{0L} = s_0^*/L^*$. Then (E.2) becomes

$$\left(\frac{\partial s_{0L}}{\partial \Phi_{\mathrm{L}}}\right)^2 + \left(\frac{\partial s_{0L}}{\partial \Psi_{\mathrm{L}}}\right)^2 = Q^2(\Phi_{\mathrm{L}}, \Psi_{\mathrm{L}}), \tag{E.5}$$

where

$$Q^2 = \frac{4i}{R_{\lambda_\Phi} |\widetilde{\mathbf{U}}|^2} \left(1 + \frac{i k_{3G}^2}{R_{\lambda_\Phi}}\right) - 1,$$

with $|\widetilde{\mathbf{U}}| = |\nabla \Phi_{\mathrm{L}}|$. Equation (E.5) is called Eikonal equation.

The boundary conditions on all the four boundaries are taken as equation (3.27) in Goldstein (1984) which is the solution for equation (E.2) for a constant mean flow, thus it can be used as the solution far from the body, where the mean flow is uniform. The solution written in the notation here used is

$$s = k_{2G} y_{\mathrm{L}} + \left[\sqrt{\frac{1}{4} R_{\lambda_\Phi}^2 Q^2 - k_{2G}^2} - \frac{1}{2} R_{\lambda_\Phi} i\right] (x_{\mathrm{L}} - x_{L0}), \tag{E.6}$$

where $k_{2G} = \lambda_\Phi^*/\lambda_\Psi^*$. By substituting Q^2 for $|\widetilde{\mathbf{U}}|$ in the above equation the following is obtained

$$s = k_{2G} y_{\mathrm{L}} + \left[\sqrt{i R_{\lambda_\Phi} - k_{3G}^2 - \frac{R_{\lambda_\Phi}^2}{4} - k_{2G}^2} - \frac{1}{2} R_{\lambda_\Phi} i\right] (x_{\mathrm{L}} - x_{L0}).$$

In the next sections it is demonstrated that the solution (E.6) satisfies equation (E.2) and there is also the proof that that solution in the inviscid limit coincides with Leib *et al.* (1999)'s region IV solution. Moreover, a few possible methods to solve the Eikonal equation everywhere in the domain are illustrated. There are two big issues in the case studied herein:

1. The right hand side of the Eikonal equation is complex.

2. The right hand side of the Eikonal equation is singular at the stagnation point.

E.1 Solution of the Eikonal equation for a constant mean flow

The following are the passages which demonstrate that the solution (E.6) satisfies equation (E.2). Remember that the outer mean flow far from the body is $\{1, 0\}$ and that the coordinates $x_{\mathrm{L}} - y_{\mathrm{L}}$ coincide with $\Phi_{\mathrm{L}} - \Psi_{\mathrm{L}}$,

$$1 - \frac{\partial s}{\partial x_{\mathrm{L}}} = -\frac{i}{R_{\lambda_\Phi}} \left[\left(\frac{\partial s}{\partial x_{\mathrm{L}}} \right)^2 + \left(\frac{\partial s}{\partial y_{\mathrm{L}}} \right)^2 + k_{3G}^2 \right],$$

$$1 - \left[\sqrt{\frac{1}{4} R_{\lambda_\Phi}^2 Q^2 - k_{2G}^2} - \frac{1}{2} R_{\lambda_\Phi} i \right] =$$
$$- \frac{i}{R_{\lambda_\Phi}} \left(\frac{1}{4} R_{\lambda_\Phi}^2 Q^2 - k_{2G}^2 - \frac{1}{4} R_{\lambda_\Phi}^2 - R_{\lambda_\Phi} i \sqrt{\frac{1}{4} R_{\lambda_\Phi}^2 Q^2 - k_{2G}^2} + k_{2G}^2 + k_{3G}^2 \right),$$

$$1 - \cancel{\sqrt{\frac{1}{4} R_{\lambda_\Phi}^2 Q^2 - k_{2G}^2}} + \frac{1}{2} R_{\lambda_\Phi} i =$$
$$- \frac{i}{4} R_{\lambda_\Phi} Q^2 + \cancel{k_{2G}^2 \frac{i}{R_{\lambda_\Phi}}} + \frac{i}{4} R_{\lambda_\Phi} - \cancel{\sqrt{\frac{1}{4} R_{\lambda_\Phi}^2 Q^2 - k_{2G}^2}} - \cancel{k_{2G}^2 \frac{i}{R_{\lambda_\Phi}}} - k_{3G}^2 \frac{i}{R_{\lambda_\Phi}},$$

$$1 + \frac{1}{2} R_{\lambda_\Phi} i = -\frac{i}{4} R_{\lambda_\Phi} \left(\frac{4i}{R_{\lambda_\Phi}} - \frac{4 k_{3G}^2}{R_{\lambda_\Phi}^2} - 1 \right) + \frac{i R_{\lambda_\Phi}}{4} - \frac{i k_{3G}^2}{R_{\lambda_\Phi}},$$

$$\cancel{1} + \cancel{\frac{1}{2} i R_{\lambda_\Phi}} = \cancel{1} + \cancel{\frac{i k_{3G}^2}{R_{\lambda_\Phi}}} + \cancel{\frac{i R_{\lambda_\Phi}}{4}} + \cancel{\frac{i R_{\lambda_\Phi}}{4}} - \cancel{\frac{i k_{3G}^2}{R_{\lambda_\Phi}}},$$

Thus the solution of Goldstein (1984) for a constant mean flow satisfies the equation (E.2).

E.2 Solution of Eikonal equation for a costant mean flow in the inviscid limit

It is important to notice that the initial gust used in Leib *et al.* (1999) has $x_{L0} = 0$.

Equation (5.11) of Leib *et al.* (1999) is the solution in the outer region, where the displacement effect is considered. The solution is here written again for convenience

$$\mathbf{u}^{(0)} = \hat{\mathbf{u}}^{\infty} e^{i(\bar{x}+k_2\Psi)-(\kappa^2+\kappa_2^2)(\bar{x}-\bar{x}_{\mathrm{L}})}, \tag{E.7}$$

where $\bar{x}$ is the streamwise coordinate scaled by λ_x (which is the equivalent of λ_Φ in the notation used here), Ψ is the streamfunction associated to the outer mean flow, which far away and not considering the displacement effect, coincided with the normal coordinate y. $k_2 = (2\pi\lambda_z)/\lambda_y$ and is the equivalent of kk_{2G} or k_Ψ, $\kappa = k_3/(k_1 R_\Lambda)^{1/2}$, $\kappa_2 = k_2/(k_1 R_\Lambda)^{1/2}$ and x_{L} is the position of the grid (not to be confused with x_{L} which here is x^*/L^*). The second part of the exponent in equation (E.7) represents the viscous decay. Is this solution of Leib *et al.* (1999) consistent with the solution of Goldstein (1984)? Yes it is, in the limit of y large (namely far from the body) and in the inviscid limit of R_{λ_Φ} large. The complete solution of Goldstein (1984) for a constant mean flow is here written again for convenience

$$s = k_{2G} y_{\mathrm{L}} + \left[\sqrt{iR_{\lambda_\Phi} - k_{3G}^2 - \frac{R_{\lambda_\Phi}^2}{4} - k_{2G}^2} - \frac{1}{2} R_{\lambda_\Phi} i \right] (x_{\mathrm{L}} - x_{L0}).$$

Considering the limit of R_{λ_Φ} large

$$s = k_{2G} y_{\mathrm{L}} + \left[\frac{iR_{\lambda_\Phi}}{2} \sqrt{1 - \frac{4i}{R_{\lambda_\Phi}} + \frac{4}{R_{\lambda_\Phi}} \left(\frac{k_{2G}^2 + k_{3G}^2}{R_{\lambda_\Phi}} \right)} - \frac{1}{2} R_{\lambda_\Phi} i \right] (x_{\mathrm{L}} - x_{L0}),$$

$$s = k_{2G} y_{\mathrm{L}} + \left[\frac{iR_{\lambda_\Phi}}{2} \left[1 - \frac{2i}{R_{\lambda_\Phi}} + \frac{2}{R_{\lambda_\Phi}} \left(\frac{k_{2G}^2 + k_{3G}^2}{R_{\lambda_\Phi}} \right) \right] - \frac{1}{2} R_{\lambda_\Phi} \right] (x_{\mathrm{L}} - x_{L0}),$$

where the Taylor expansion of $\sqrt{1+1/x}$ in the limit of $x \to \infty$ has been used. The above equation becomes

$$s = k_{2G} y_{\mathrm{L}} + \left[1 + i\left(\frac{k_{2G}^2 + k_{3G}^2}{R_{\lambda_\Phi}}\right)\right](x_{\mathrm{L}} - x_{L0}). \tag{E.8}$$

Now each term has to be written in Leib *et al.* (1999)'s notation in order to see that the two solutions are the same. This can easily be done by comparing quantities with dimensions. The results are

$$\begin{aligned}
k_{2G} y_{\mathrm{L}} &= \frac{\lambda_\Phi^* y^*}{\lambda_\Psi^* L^*} = \frac{k_\Psi y}{k}, \\
k_{2G} &= \frac{\lambda_\Phi^*}{\lambda_\Psi^*} = \frac{k_\Psi}{k_\Phi}, \\
k_{3G} &= \frac{\lambda_\Phi^*}{\lambda_z^*} = \frac{k_z}{k_\Phi}, \\
R_{\lambda_\Phi} &= \frac{U_\infty^* \lambda_\Phi}{2\pi\nu *} = \frac{R}{k_\Phi}, \\
x_{\mathrm{L}} &= \frac{x^*}{L^*} = \frac{\bar{x}}{k}.
\end{aligned}$$

Thus,

$$s = \frac{k_\Psi y}{k} + \left[1 + \frac{ik\cancel{k_\Phi}}{R}\left(\frac{k_\Psi^2 + k_z^2}{\cancel{k_\Phi^2}}\right)\right]\frac{(x_{\mathrm{L}} - x_{L0})}{k}.$$

The exponent of the solution in Goldstein (1984) is iks, $\kappa = k_3/(k_1 R_\Lambda)^{1/2}$, $\kappa_2 = k_2/(k_1 R_\Lambda)^{1/2}$ and rearranging it is obtained

$$iks = i(\bar{x} + k_\Psi y) - (\kappa + \kappa^2)(\bar{x} - \bar{x}_0) - i\bar{x}_0,$$

which is exactly Leib *et al.* (1999)'s solution (Leib *et al.* (1999)'s k_2 is here k_Ψ). It has been demonstrated that the solution (3.27) in Goldstein (1984) in the limit of large R_{λ_Φ} is identical to the solution (5.11) of Leib *et al.* (1999). The only difference is in the initial point, which is equal to zero in Leib *et al.* (1999).

E.3 Numerical methods for the Eikonal equation

The Eikonal equation (E.5) is a first order nonlinear partial differential equation, here written again for convenience

$$\left(\frac{\partial s_{0L}}{\partial \Phi_{dL}}\right)^2 + \left(\frac{\partial s_{0L}}{\partial \Psi_{dL}}\right)^2 = Q^2(\Phi_{dL}, \Psi_{dL}).$$

It can be numerically solved, but it is harder to find a solution if the right hand side is a complex function which also becomes singular in one point. This is exactly the case, since

$$Q^2 = \frac{4i}{R_{\lambda_\Phi}|\widetilde{\mathbf{U}}|^2}\left(1 + \frac{ik_{3G}^2}{R_{\lambda_\Phi}}\right) - 1,$$

where $|\widetilde{\mathbf{U}}|^2$ is the outer mean velocity which is zero at the stagnation point. During the analysis of the outer flow, several numerical methods have been tested to find a complete solution of the Eikonal equation (E.5). However, none of these methods led to the solution. In this appendix some of these methods will be briefly illustrated.

First of all the singularity has to be removed. In order to do that a smooth Gaussian function is added to $|\widetilde{\mathbf{U}}|^2$ at the denominator of the right hand side of (E.5) in a way to have $|\widetilde{\mathbf{U}}|^2$ not singular at the stagnation point but still 1 far from the body. This strategy has been adopted in each of the following methods.

Charpit's method

The Charpit's method is suitable for nonlinear partial differential equations of first order such as the Eikonal equation (E.5). The partial differential equation reduces to a system of ordinary differential equations, which should be easier to solve. A function G can be defined

$$G(b, q, s_{0L}, \Phi_{dL}, \Psi_{dL}) = b^2 + q^2 - Q^2 = 0,$$

where

$$b = \frac{\partial s_{0L}}{\partial \Phi_{dL}},$$

$$q = \frac{\partial s_{0L}}{\partial \Psi_{dL}},$$

$$\frac{\partial b}{\partial \Psi_{dL}} = \frac{\partial q}{\partial \Phi_{dL}}.$$

Characteristic rays $\Phi_{dL}(\tau)$,$\Psi_{dL}(\tau)$ are defined which should satisfy

$$\frac{d\Phi_{dL}}{\partial \tau} = \frac{\partial G}{\partial b}, \tag{E.9}$$

$$\frac{d\Psi_{dL}}{\partial \tau} = \frac{\partial G}{\partial q}. \tag{E.10}$$

The following are the Charpit's equations obtained from the Eikonal equation (E.5):

$$\frac{d\Phi_{dL}}{d\tau} = 2b, \tag{E.11a}$$

$$\frac{d\Psi_{dL}}{d\tau} = 2q, \tag{E.11b}$$

$$\frac{db}{d\tau} = \frac{\partial Q^2}{\partial \Phi_{dL}}, \tag{E.11c}$$

$$\frac{dq}{d\tau} = \frac{\partial Q^2}{\partial \Psi_{dL}}, \tag{E.11d}$$

$$\frac{ds_{0L}}{d\tau} = 2Q^2. \tag{E.11e}$$

In order to numerically solve equations (E.11) initial conditions for $\tau = 0$ must be specified along y_L. The following are the initial conditions in the limit of $R_{\lambda_\Phi} \to \infty$:

$$\Phi_{dL}(y_L, 0) = \Phi_{dL0},$$

$$\Psi_{dL}(y_L, 0) = \Psi_{dL0},$$

$$s_{0L}(y_L, 0) = 0,$$

$$b(y_L, 0) = i,$$

$$q(y_L, 0) = 0.$$

The Charpit's method seems to have problems with complex functions. In fact, equations (E.9) and (E.10) can not be satisfied because the potential and stream-function are real, the characteristic ray is real as well, but the function G is complex. Thus, to let the method work, the complex potential should be defined, but then the Charpit's method could not be used.

Vanishing viscosity method

The vanishing viscosity method consists in adding the second partial derivatives of the function to the left hand side of the equation, both multiplied by a small parameter ϵ. The ϵ dependent solution of the second order partial differential equation is found and then, in order to find the solution for the Eikonal equation, the limit of $\epsilon \to 0$ is taken. The vanishing viscosity method is really useful, for example, when Gauss-Seidel iterative method is adopted to solve a partial differential equation.

As it is an iterative method, after every iteration the residual is evaluated and compared with a small value, previously set. If the residual is smaller than that value the equation is satisfied and the method converges to the solution. Otherwise the solution is up to date and the calculations are repeated in the next iteration. Iterative methods can also diverge. The residual is evaluated on each point and at the end of each iteration the maximum value of the residual is

compared with the threshold. For this reason the maximum residual could also oscillate before decreasing or increasing.

By adding the second derivative, the problem of chosing between two roots in the discretized form of the equation is avoided. This concept is better understood by seeing how the Eikonal equation is discretized. Equation (E.5) can be discretized by Euler method and it becomes

$$\left(\frac{s_{i,j} - s_{i-1,j}}{dh}\right)^2 + \left(\frac{s_{i,j} - s_{i,j-1}}{dh}\right)^2 = Q^2(\Phi_i, \Psi_j), \tag{E.12}$$

where the subscripts 'L' and 'dL' have been omitted for simplicity. The step dh is distance between two consecutive points of the grid, both in the horizontal and in the vertical direction. In (E.12) it is seen that the value $s_{i,j}$ is squared, thus with this discretization there would be two roots for each grid point and it would be necessary to choose between one of these two. By vanishing viscosity method the Eikonal equation (E.5) becomes

$$\epsilon\left(\frac{\partial^2 s_{0L}}{\partial\Phi_{dL}^2} + \frac{\partial^2 s_{0L}}{\partial\Psi_{dL}^2}\right) + \left(\frac{\partial s_{0L}}{\partial\Phi_{dL}}\right)^2 + \left(\frac{\partial s_{0L}}{\partial\Psi_{dL}}\right)^2 = Q^2(\Phi_{dL}, \Psi_{dL}). \tag{E.13}$$

By using second order central difference (E.13) is discretized as follows

$$\begin{aligned}\epsilon\left(\frac{s_{i+1,j} - 2s_{i,j} + s_{i-1,j}}{dh^2} + \frac{s_{i,j+1} - 2s_{i,j} + s_{i,j-1}}{dh^2}\right) + \\ + \left(\frac{s_{i,j} - s_{i-1,j}}{dh}\right)^2 + \left(\frac{s_{i,j} - s_{i,j-1}}{dh}\right)^2 = Q^2(\Phi_i, \Psi_j).\end{aligned} \tag{E.14}$$

From equation (E.14) the value of the function at each grid point can be found and Gauss-Seidel iterative method can be employed to find the solution. This iterative method is improved by the relaxation parameter ω, which can accelerate the convergence of the method.

This method does not work for small ϵ. In fact the solution for $\epsilon = 10$ has been found, but when the parameter ϵ is slowly decreased the residual starts to

increase until it becomes very large and the method diverges.

Fast sweeping algorithm

During the last 10 years numerical algorithms have been designed to solve the nonlinear equations obtained by the discretization of the Eikonal equation. The problem is then treated as a stationary boundary value problem. Two of these methods are for example the fast marching method developed by Sethian (1999) and the fast sweeping algorithm developed by Zhao (2004). Much time has been spent in trying to extend the last algorithm to complex functions.

The fast sweeping algorithm uses upwind difference for the discretization of the Eikonal equation. In fact the first derivative which appears in the equation can be approximated by backward Euler or forward Euler method at each point. The upwind difference scheme is a way to choose at each point which of the two Euler methods is better to use. This choice is done by always choosing the largest finite difference (which approximate the first derivative) and then the value of the function is evaluated by a formula found by Zhao (2004). The fast sweeping algorithm uses Gause-Seidel iterations and at each iteration the value of the function is updated to the smaller value between the old one and the new one until convergence.

As stated in the paper, this method works if the right hand side of the Eikonal equation is positive, namely if the function to be found is real. The method has been tested for several real cases and it actually works. But this is not the case of equation (E.5) where the right hand side is complex.

We have tried an extension to the algorithm of Zhao (2004). Two equations for the real part and the imaginary part are obtained from the Eikonal equation. These two are obviously coupled since the equation is nonlinear. A first guess solution is used in order to start the method. The equation for the real part is

iteratively solved with the initial imaginary part, then the solution of the real part is substituted in the imaginary equation and a new imaginary part is found. This is substituted into the real equation and a new iteration starts. Unfortunately, what happens is that at some iterations, the right hand side of the real equation, which contains the imaginary part, becomes negative thus the code gives error.

BIBLIOGRAPHY

Anderson, J.D.Jr. 2007. *Fundamentals of aerodynamics*. 4 edn. McGraw Hill.

Andersson, P., Berggren, M., & Henningson, D.S. 1999. Optimal disturbances and bypass transition in boundary layers. *Phys. Fluids*, **11**(1), 134–150.

Bae, S., Lele, S.K., & Sung, H.J. 2003. Direct numerical simulation of stagnation region flow and heat transfer with free-stream turbulence. *Phys. Fluids*, **15**, 1462–1484.

Batchelor, G.K., & Proudman, I. 1954. The effect of rapid distortion of a fluid in turbulent motion. *Quart. J. Mech. Appl. Maths*, **7**(1), 83–103.

Bearman, P.W. 1972. Some measurements of the distortion of turbulence approaching a two-dimensional bluff body. *J. Fluid Mech.*, **53**(03), 451–467.

Bearman, P.W., & Morel, T. 1983. Effect of free stream turbulence on the flow around bluff bodies. *Prog. Aerospace Sci.*, **20**, 97–123.

Bender, M., & Orszag, S. A. 1999. *Advanced Mathematical Methods for Scientists and Engineers - Asymptotic methods and perturbation theory*. Springer.

Bertolotti, F.P. 1997. Response of the Blasius boundary layer to free-stream vorticity. *Phys. Fluids*, **9**(8), 2286–2299.

Brandt, L., & Henningson, D.S. 2002. Transition of streamwise streaks in zero-pressure-gradient boundary layers. *J. Fluid Mech.*, **472**, 229–261.

Brattkus, K., & Davis, S. H. 1991. The linear stability of plane stagnation-point flow against general disturbances. *Q. J. Mech. Appl. Math.*, **44**(1), 135–146.

Butler, K.M., & Farrell, B.F. 1992. Three-dimensional optimal perturbations in viscous shear flow. *Phys. Fluids*, **4**(8), 1637–1650.

Cebeci, T. 2002. *Convective Heat Transfer*. Springer-Verlag, Berlin Heidelberg.

Choudhari, M. 1996. Boundary layer receptivity to three-dimensional unsteady vortical disturbances in the free stream. *AIAA Paper 96-0181*.

Criminale, W.O., Jackson, T. L., & Lasseigne, D. G. 1994. Evolution of disturbances in stagnation-point flow. *J. Fluid Mech.*, **270**, 331–347.

Dong, M., & Wu, X. 2013. On continuous spectra of the Orr-Sommerfeld/Squire equations and entrainment of free-stream vortical disturbances. *J. Fluid Mech.*, **732**, 616–659.

Dryden, H.L. 1936. Air flow in the boundary layer near a plate. *NACA Rep.*, **562**.

Fransson, J.H.M., Matsubara, M., & Alfredsson, P.H. 2005. Transition induced by free-stream turbulence. *J. Fluid Mech.*, **527**, 1–25.

Goldstein, M.E. 1978. Unsteady vortical and entropic distortions of potential flows round arbitrary obstacles. *J. Fluid Mech.*, **89**, 433–468.

Goldstein, M.E. 1984. Small-amplitude viscous motion on arbitrary potential flows. *Quart. J. Mech. Appl. Math.*, **37**, 1–31.

Goldstein, M.E., & Atassi, H. 1976. A complete second-order theory for the unsteady flow about an airfoil due to a periodic gust. *J. Fluid Mech.*, **74**(04), 741–765.

Gorla, R.S.R. 1978. Transient response behavior of an axisymmetric stagnation flow on a circular cylinder due to time dependent free stream velocity. *Lett. Appl. Engng Sci.*, **16**, 493–502.

Guegan, A., Huerre, P., & Schmid, P. J. 2007. Optimal disturbances in swept Hiemenz flow. *J. Fluid Mech.*, **578**, 223–232.

Higuera, M., & Vega, J.M. 2009. Modal description of internal optimal streaks. *J. Fluid Mech.*, **626**, 21–31.

Holmes, M. H. 2013. *Introduction to Perturbation Methods*. Springer.

Huai, X., Joslin, R. D., & Piomelli, U. 1999. Large-eddy simulation of boundary-layer transition on a swept wedge. *J. Fluid Mech.*, **381**, 357–380.

Hunt, J.C.R. 1973. A theory of turbulent flow round two-dimensional bluff bodies. *J. Fluid Mech.*, **61**(04), 625–706.

Jacobs, R.G., & Durbin, P.A. 2001. Simulation of bypass transition. *J. Fluid Mech.*, **428**, 185–212.

Jacobs, Robert G, & Durbin, Paul A. 1998. Shear sheltering and the continuous spectrum of the Orr–Sommerfeld equation. *Phys. Fluids*, **10**, 2006.

John, M. O., Obrist, D., & Kleiser, L. 2014. Stabilization of subcritical bypass transition in the leading-edge boundary layer by suction. *J. Turbul.*, **15**(11), 795–805.

Johnson, M. W., & Ercan, A.H. 1999. A physical model for bypass transition. *Int. J. Heat Fluid Flow*, **20**, 95–104.

Kaplun, S. 1954. *The role of coordinate systems in boundary layer theory*. Ph.D. thesis, California Institute of Technology.

Kendall, J.M. 1990. Boundary layer receptivity to free stream turbulence. *AIAA Paper*, **90-1504**.

Kestin, J., & Wood, R.T. 1970. On the stability of two-dimensional stagnation flow. *J. Fluid Mech.*, **44**, 461–479.

Klebanoff, P.S. 1971. Effect of free-stream turbulence on a laminar boundary layer. *Bull. Am. Phys. Soc.*, **16**, 1323.

Kleiser, Leonhard, & Zang, Thomas A. 1991. Numerical simulation of transition in wall-bounded shear flows. *Ann. Rev. Fluid Mech.*, **23**(1), 495–537.

Ladyzhenskaya, O.A., & Silverman, R.A. 1969. *The mathematical theory of viscous incompressible flow.* Gordon and Breach.

Landahl, M.T. 1980. A note on an algebraic instability of inviscid parallel shear flows. *J. Fluid Mech.*, **98**, 243–251.

Leib, S.J., Wundrow, D.W., & Goldstein, M.E. 1999. Effect of free-stream turbulence and other vortical disturbances on a laminar boundary layer. *J. Fluid Mech.*, **380**, 169–203.

Libby, P.A., & Fox, H. 1964. Some perturbation solutions in laminar boundary-layer theory. *J. Fluid Mech.*, **17**, 433–449.

Liepmann, H. W., & Nosenchuck, D. M. 1982. Active control of laminar-turbulent transition. *J. Fluid Mech.*, **118**, 201–204.

Lorna, J. A., & Peake, N. 2016. Interaction of turbulence with the leading-edge stagnation point of a thin aerofoil. *J. Fluid Mech.*, **798**, 439–456.

Luchini, P. 1996. Reynolds-number-independent instability of the boundary layer over a flat surface. *J. Fluid Mech.*, **327**, 101–115.

Luchini, P. 2000. Reynolds-number-independent instability of the boundary layer over a flat surface: optimal perturbations. *J. Fluid Mech.*, **404**, 289–309.

Maciejewski, P.K., & Moffat, R.J. 1992. Heat Transfer With Very High Free-Stream Turbulence: Part I - Experimental Data. *J. Heat Transfer*, **114**, 827–833.

Mack, C. J., & Schmid, P. J. 2011. Global stability of swept flow around a parabolic body: features of the global spectrum. *J. Fluid Mech.*, **669**, 375–396.

Mack, C. J., Schmid, P. J., & Sesterhenn, J. L. 2008. Global stability of swept flow around a parabolic body: connecting attachment-line and crossflow modes. *J. Fluid Mech.*, **611**, 205–214.

Mans, J., Kadijk, E.C., de Lange, H.C., & van Steenhoven, A.A. 2005. Breakdown in a boundary layer exposed to free-stream turbulence. *Exp. Fluids*, **39**, 1071–1083.

Mans, J., de Lange, H.C., & van Steenhoven, A.A. 2007. Sinuous breakdown in a flat plate boundary layer exposed to free-stream turbulence. *Phys. Fluids*, **19**(088101).

Matsubara, M., & Alfredsson, P.H. 2001. Disturbance growth in boundary layers subjected to free-stream turbulence. *J. Fluid Mech.*, **430**, 149–168.

Obrist, D., & Schmid, P. J. 2010. Algebraically decaying modes and wave packet pseudo-modes in swept Hiemenz flow. *J. Fluid Mech.*, **643**, 309–332.

Obrist, D., & Schmid, P. J. 2011. Algebraically diverging modes upstream of a swept bluff body. *J. Fluid Mech.*, **683**, 346–356.

Obrist, D., Henniger, R., & Kleiser, L. 2012. Subcritical spatial transition of swept Hiemenz flow. *Int. J. Heat and Fluid Flow*, **35**, 61–67.

Ovchinnikov, V., Choudhari, M.M., & Piomelli, U. 2008. Numerical simulations of boundary-layer bypass transition due to high-amplitude free-stream turbulence. *J. Fluid Mech.*, **613**, 135–169.

Panton, R. 1995. *Incompressible Flow.* Wiley-Interscience – Second Edition.

Pérez, J. M., Rodríguez, D., & Theofilis, V. 2012. Linear global instability of non-orthogonal incompressible swept attachment-line boundary-layer flow. *J. Fluid Mech.*, **710**, 131–153.

Polyanin, A.D. 2001. *Handbook of linear partial differential equations for engineers and scientists.* CRC press.

Ricco, P., Luo, J., & Wu, X. 2011. Evolution and instability of unsteady nonlinear streaks generated by free-stream vortical disturbances. *J. Fluid Mech.*, **677**, 1–38.

Rist, U., & Fasel, H. 1995. Direct numerical simulation of controlled transition in a flat-plate boundary layer. *J. Fluid Mech.*, **298**(9), 211–248.

Sadeh, W.Z., Sutera, S.P., & Maeder, P.F. 1970. Analysis of vorticity amplification in the flow approaching a two-dimensional stagnation point. *J. Appl. Math. Phys.*, **21**, 699–716.

Schlichting, H. 1979. *Boundary-layer theory.* McGraw Hill.Inc.

Sethian, J.A. 1999. Fast Marching Methods. *SIAM Review*, **41**(2), 199–235.

Sutera, S.P., Maeder, P.F., & Kestin, J. 1963. On the sensitivity of heat transfer in the stagnation point boundary layer to free-stream velocity. *J. Fluid Mech.*, **16**, 497–520.

Taylor, G.I. 1935. Statistical theory of turbulence. *Proc. R. Soc. London*, **151**(873), 421–444.

Taylor, G.I. 1939. Some recent developments in the study of turbulence. *Fifth Intl. Congr. for Appl. Mech.*, 294–310.

Tempelmann, D., Hanifi, A., & Henningson, D.S. 2012. Swept-wing boundary-layer receptivity. *J. Fluid Mech.*, **700**, 490–501.

Theofilis, V. 1993. Numerical experiments on the stability of leading edge boundary layer flow: a two-dimensional linear study. *Int. J. Numer. Meth. Fluids*, **16**, 153–170.

Theofilis, V. 1994. The discrete temporal eigenvalue spectrum of the generalised Hiemenz flow as solution of the Orr-Sommerfeld equation. *J. Eng. Math.*, **28**, 241–259.

Thomas, C., Hall, P., & Davies, C. 2015. Nonlinear effects on the receptivity of cross-flow in the swept Hiemenz flow. *J. Fluid Mech.*, **763**, 433–459.

Turner, M. R. 2005. Numerical and asympotic approaches to boundary-layer receptivity and transition. *PhD Thesis, University of East Anglia.*

Ueda, T., Imaizumi, H., Mizomoto, M., & Shepherd, I. G. 1997. Velocity statistics along the stagnation line of an axi-symmetric stagnation turbulent flow. *Experiments in Fluids*, 473–481.

van Driest, E.R., & Blumer, C. B. 1963. Boundary layer transition: freestream turbulence and pressure gradient effects. *AIAA J.*, **1**(6), 1303–1306.

Van Dyke, M. 1975. *Perturbation Methods in Fluid Mechanics.* The Parabolic Press - Stanford, California.

Venema, L., von Terzi, D., Bauer, H., & W., Rodim. 2014. Direct Numerical Simulation of Stagnation Point Heat Transfer Affected by Varying Wake-Induced Turbulence. *J. Turbom.*, **136**, 021008–1–7.

Walsh, E.J., Davies, M.R.D., & McEligot, D.M. 2004. On the use of entropy to predict boundary layer stability. *Entropy*, **6**(4), 375–387.

Wundrow, D.W., & Goldstein, M.E. 2001. Effect on a laminar boundary layer of small-amplitude streamwise vorticity in the upstream flow. *J. Fluid Mech.*, **426**, 229–262.

Xiong, Z., & Lele, S.K. 2001. Numerical study of leading-edge heat transfer under free-stream turbulence. *AIAA Paper 2001-1016*.

Xiong, Z., & Lele, S.K. 2004. Distortion of upstream disturbances in a Hiemenz boundary layer. *J. Fluid Mech.*, **519**, 201–232.

Zaki, T., & Durbin, P.A. 2005. Mode interaction and the bypass route to transition. *J. Fluid Mech.*, **531**, 85–111.

Zaki, T., & Durbin, P.A. 2006. Continuous mode transition and the effects of pressure gradient. *J. Fluid Mech.*, **563**, 357–388.

Zhao, H. 2004. A fast sweeping method for Eikonal equations. *Mathematics of Computation*, **74**(250), 603–627.